Ultrafast momentum microscopy of dark exciton dynamics in real- and reciprocal-space

Dissertation

zur Erlangung des mathematisch-naturwissenschaftlichen Doktorgrades

"Doctor rerum naturalium"

der Georg-August-Universität Göttingen

im Promotionsstudiengang Physik

der Georg-August-University School of Science (GAUSS)

Vorgelegt von

David Schmitt

aus Lich

Göttingen, 2023

Thesis Committee

Prof. Dr. Stefan Mathias
I. Physikalisches Institut, Georg-August-Universität Göttingen

Prof. Dr. Martin Wenderoth
IV. Physikalisches Institut, Georg-August-Universität Göttingen

Prof. Dr. Stefan Kehrein
Institut für Theoretische Physik, Georg-August-Universität Göttingen

Members of the Examination Board

Reviewer:
Prof. Dr. Stefan Mathias
I. Physikalisches Institut, Georg-August-Universität Göttingen

Second Reviewer:
Prof. Dr. Thomas Weitz
I. Physikalisches Institut, Georg-August-Universität Göttingen

Further members of the Examination Board

Prof. Dr. Martin Wenderoth
IV. Physikalisches Institut, Georg-August-Universität Göttingen

Prof. Dr. Claus Ropers
Max-Planck-Institut für Multidisziplinäre Naturwissenschaften, Göttingen

Prof. Dr. Fabian Heidrich-Meisner
Institut für Theoretische Physik, Georg-August-Universität Göttingen

Prof. Dr. Salvatore Manmana
Institut für Theoretische Physik, Georg-August-Universität Göttingen

Date of the oral examination: 17.08.2023

Contents

CHAPTER 1

Introduction

Atomically thin transition metal dichalcogenides (TMDs) provide a new, versatile platform to study and control correlated quantum material properties [1, 2]. Monolayer semiconducting TMDs such as MoS_2, $MoSe_2$, WS_2 and WSe_2 have attracted considerable attention [3]. The weak dielectric screening from the environment gives rise to strongly enhanced Coulomb interactions and, thus, the optical response is dominated by the formation, thermalization and recombination of tightly-bound electron-hole pairs, i.e. excitons, with extremely large binding energies of up to 500 meV [3]. In consequence, the optical response of these materials is no longer defined by the single-particle electronic band structure, but by the exciton landscape, which includes optically bright excitons, where direct optical excitation and recombination is possible, and optically dark excitons, e.g. momentum-indirect excitons, where the different momenta of electron and hole forbid direct excitation/recombination with light.

While monolayer TMDs already exhibit intriguing properties, the properties can be further controlled by combining different TMD monolayers to form stacked TMD heterostructures [4]. Depending on the band alignment of the respective layers, the overall conduction band minimum and valence band maximum can be located in different layers. In such type-II aligned heterostructures a charge transfer of electrons or holes between adjacent layers can be energetically favorable [5]. As a result, so-called interlayer excitons can be formed, where the electron and the hole are located in two different layers. Furthermore, the hybridization of the two layers allows the formation of so-called hybrid excitons, where the electron and/or hole can be delocalized between the neighboring layers [6, 7]. The exciton landscape can be even further manipulated by introducing a rotational misalignment between the layers. The rotation not only affects the hybridization and corresponding exciton dynamics [6, 8], but also gives rise to a so-called moiré potential capable of confining excitons in its potential landscape [9]. The on-demand control of excitons by twisting has opened up the new research field of 'twistronics' that investigates new possibilities to build, e.g., programmable quantum emitters [10] and exciton crystals [11]. Because of the plethora of fascinating properties of TMD heterostructures, especially with regard to the excitonic properties, it is of fundamental interest to have experimental access to the exciton landscape of TMDs and to understand the optical response of such systems. A part of the exciton landscape can be accessed by all-optical experiments, such as photoluminescence and absorption spectroscopy. Seminal experimental works using these techniques were indeed able to provide spectrally resolved signatures of interlayer and intralayer excitons [12, 3, 13], exciton confinement effects within moiré potentials [14], timescales of interlayer charge transfer [15, 16] and lifetimes of inter-

layer excitons [17]. However, all of these experimental techniques are not directly sensitive to the momentum distribution of excitons and therefore are fairly limited to access the whole energy landscape of excitons, which determines the respective exciton formation, thermalization and recombination dynamics. In addition to the spectroscopic information, there is also huge research interest in the exciton landscape and dynamics on a nanometer spatial scale [18, 19]. Exfoliated TMD structures are typically exposed to different kinds of disorder on the nanometer-to-micrometer spatial scale [20]. Understanding the influence of such disorder on the exciton landscape plays a crucial role for the application of these materials in opto-electronic devices. However, the simultaneous access to the following key-aspects in this research field have so far remained experimentally challenging:

1. Access to the dark exciton energy landscape.
2. Access to the ultrafast exciton formation, thermalization and recombination processes within the dark exciton landscape.
3. Access to the nanoscale variation of the dark exciton landscape and dynamics.

To shed light on these questions, new experimental strategies have to be established [18, 21, 22, 23, 19]. Here, the seminal experiments of Madéo *et al.* [24] and Wallauer *et al.* [25] showed that time-resolved and angle-resolved-photoemission spectroscopy (trARPES) is able to detect the photoemission yield of bright and dark momentum-indirect excitons with the concomitant temporal evolution of the photoemission yield of the respective excitons. Furthermore, trARPES experiments have shown that other key quantities, such as the Bohr radius of the exciton, can be directly determined [26, 27]. The mentioned experiments are using a new experimental approach to trARPES, i.e. time-resolved momentum microscopy (trMM). This new detection scheme allows the simultaneous acquisition of the kinetic energy (E_{kin}) and the two in-plane momenta (k_x, k_y) of the photoelectrons across the whole Brillouin zone within µm-sized regions-of-interest. In this way, trMM provides a new tool for studying the momentum-resolved exciton landscape and dynamics throughout the entire Brillouin zone. (c.f. Fig. 1.0.1).

In the first article [28] of this cumulative Ph.D. thesis, the trMM experiment [29] is used to investigate the momentum-resolved exciton dynamics of a 9.8° twisted WSe_2/MoS_2 heterostructure (c.f. Fig. 1.0.1). This new approach is used to:

1. Identify the distinct photoemission momentum distribution of the interlayer exciton.
2. Provide a precise experimental identification of the interlayer exciton formation mechanism.
3. Reconstruct the electron contribution to the interlayer exciton wave function.

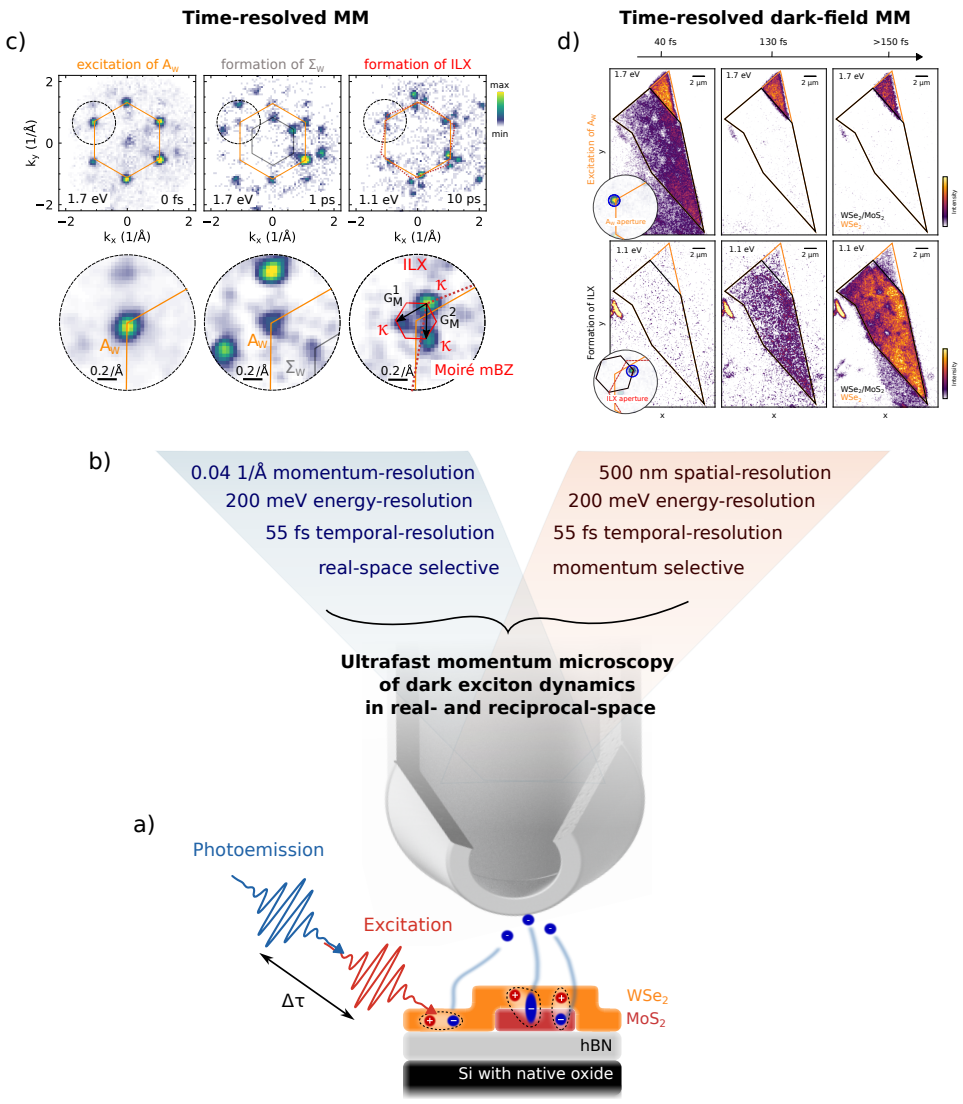

Fig. 1.0.1.: Accessing the exciton landscape and dynamics in real-space and in reciprocal space of a twisted WSe_2/MoS_2 heterostructure. a) Illustration of the photoemission process from excitons. The pump pulse (red) creates bright intralayer excitons in WSe_2, which can thermalize to interlayer and hybrid excitons. The time-delayed EUV pulse (blue) breaks up the electron-hole pair and causes the photoemission of the exciton's electron. b) The photoemitted electrons are measured with a time-of-flight momentum microscope, which can be operated in momentum- and in real-space. c) In the first publication the momentum-space mode is used to resolve the distinct time-resolved momentum distribution of the photoemission signature of excitons [28]. d) The second publication shows that dark-field momentum microscopy is able to follow ultrafast exciton dynamics with nanometer spatial resolution [30].

The investigation of the nanoscale spatial variation of the dark exciton landscape and dynamics is experimentally much more challenging. The ideal experiment has to provide femtosecond-to-picosecond temporal and nanometer-to-micrometer spatial resolution, and preferably spectroscopic information. The momentum-resolved trMM experiment described before does not yet justify these requirements, because the experiment usually averages over areas with about 10 µm diameters [28, 25, 24] and is therefore not sensitive to inhomogeneities on the nanometer scale. This Ph.D. thesis presents a new approach that is able to provide direct access to the desired quantities: Time-resolved dark-field momentum microscopy. Here, the real-space capabilities of the trMM setup are used to follow the temporal evolution of the photoemission yield of a selected momentum region-of-interest, e.g. the dark interlayer exciton, with 55 femtosecond time-, 200 meV spectral- and 500 nm spatial resolution (c.f. Fig. 1.0.1). In the second article of this cumulative Ph.D. thesis, time-resolved dark-field momentum microscopy is used to investigate:

1. Sub-µm spatial variation of the intralayer and dark interlayer exciton landscape.
2. Sub-µm spatial variation of the formation of dark interlayer excitons.
3. Correlations between the spatio-temporal and spatio-spectral information.

Combining both worlds of momentum and real-space trMM measurements provides a new way to probe the entire exciton landscape and dynamics with momentum-, spatial-, spectral- and temporal-resolution and paves the way for new types of experiments with spatio-spectral and spatio-temporal capabilities.

Outline of the PhD-thesis:

This PhD-thesis is structured as follows.

Chapter 2:
Section 2.1 starts with a short summary of the fundamental quantities measured in typical ARPES experiments. The extension to time-resolved ARPES (trARPES) is introduced as the main experimental tool used in this PhD-thesis. The following section 2.3 will introduce the material class of TMDs as the main sample system investigated in this PhD-thesis. The section will first provide information about the lattice and electronic structure, before introducing the research field of excitons. Section 2.4.4 introduces the energy landscape of monolayer and heterostructure TMDs, including the description of inter/intralayer, hybrid and moiré excitons and their role for the respective exciton dynamics. After that, the influence of disorder to the exciton landscape is discussed and the experimental techniques to access excitons are introduced. The next section 2.5 describes the photoemission signatures of excitons.

Section 2.6.1 starts with a specification of the requirements that the experiment must fulfill in order to measure the exciton landscape and dynamics. After that, the time-resolved momentum microscopy setup is briefly introduced.

Chapter 3:
In the first publication [28], time-resolved momentum microscopy measurements are performed on a 9.8° twisted WSe_2/MoS_2 heterostructure. The emphasis lies here on the distinct momentum fingerprint of interlayer excitons, the exact formation dynamics of interlayer excitons and the reconstruction of the electronic real-space wavefunction of the interlayer exciton.

Chapter 4:
In the second publication [30], femtosecond dark-field momentum microscopy is used as a new technique to obtain unprecedented spatio-temporal and spatio-spectral information of the exciton landscape and dynamics of a 28.8° twisted WSe_2/MoS_2 heterostructure.

Chapter 5:
The final chapter of this thesis begins with a discussion of further observation and analysis of the data sets beyond the evaluation presented in the two articles, and ends with possible future improvements to the existing setup.

Appendix A and B
Appendix A provides additional information to the time-resolved momentum microscopy setup, including a description of the different imaging modes and alignment procedures. Finally, the limitations of the current setup are discussed. Appendix B provides additional information on data-handling of the second manuscript, "Ultrafast nano-imaging of dark excitons".

CHAPTER 2

Background

2.1. Angle-Resolved Photoemission Spectroscopy

Angle-resolved photoemission spectroscopy (ARPES) is the main experimental technique used in this thesis. In this chapter, a brief introduction is given in order to describe the fundamental quantities observed in the experiment. A more detailed description, covering both theory and the experimental details of ARPES experiments, can be found in the standard literature of Hüfner [31] and several review articles [32, 33, 34].

Angle-resolved photoemission experiments provide the most direct way to access the electronic band structure of a material by measuring the angle and kinetic energy of the photoemitted electrons. The kinetic energy of the photoelectron is given by [31]

$$E_{\mathrm{kin}} = h\nu - E_{\mathrm{B}} - \phi. \tag{2.1}$$

Since the constant work function ϕ is dependent on the material and the photon energy $h\nu$ is given by the light source, the measured kinetic energy is directly proportional to the binding energy E_{B} of the initial electron before photoemission (c.f. Fig. 2.1.1 a)). The emission angle α and the kinetic energy of the photoelectron give access to the in-plane momenta of the photoelectron [31]

$$|k_{||}^{f}| = \sqrt{k_x^{f2} + k_y^{f2}} = \sqrt{\frac{2m_e E_{\mathrm{kin}}}{\hbar^2}}\sin(\alpha). \tag{2.2}$$

Because of the in-plane translational symmetry of the solid, the in-plane momentum is conserved during the photoemission process. Therefore, the emission angle provides direct access to the crystal momentum of the initial state electron (c.f. Fig. 2.1.1 b)). On the other hand, the out-of-plane component is not conserved during the photoemission process and in general very difficult to access in experiment [35]. From equation (2.2) it is evident that the kinetic energy and specifically the photon energy determines the accessible momentum range. The maximal accessible momentum as a function of E_{kin} can be calculated by setting $\alpha = 90°$, which results for the given experimental conditions ($h\nu = 26.6$ eV, ϕ_{WSe_2}=4.35 eV [36], $E_B \approx 0$) in a maximal momentum of $k_{||,\mathrm{max}}$=2.42 1/Å for the photoemission experiment. In commonly used ARPES experiments (hemispherical analyzers) the emission angle has to be elaborately converted into the momentum coordinates, whereas in the photoemission scheme used in this work (trMM), a direct imaging of the momentum is intrinsically performed. In this way, the experiment provides the kinetic energies and the in-plane mo-

mentum of each emitted photoelectron within the photoemission horizon (c.f. Fig. 2.1.1 c) and 2.1.3), defined as

$$E_{\text{kin}} = \frac{\hbar^2(k_x^2 + k_y^2)}{2m_e}. \tag{2.3}$$

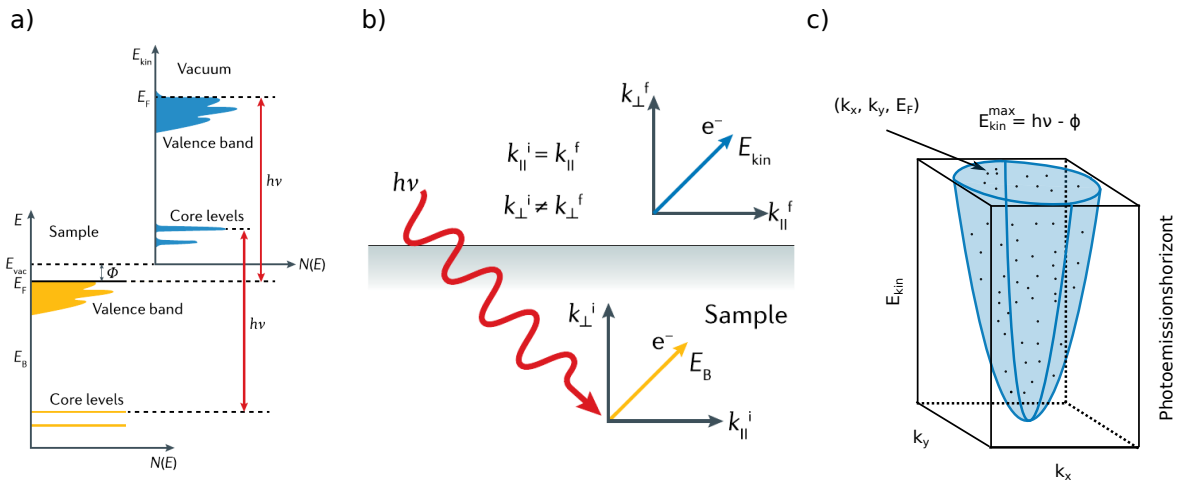

Fig. 2.1.1.: a) Illustration of energy conservation during the photoemission process. Bands with a certain initial binding energy are projected via equation 2.1 to kinetic energies. b) Illustration of the momentum conservation during the photoemission process. While the in-plane momentum is conserved $k_{||}^i = k_{||}^f$, because of the translation symmetry of the lattice, the out-of plane component is influenced by the inner potential $k_\perp^i \neq k_\perp^f$. c) The available energy-momentum-space (blueish-area) of the photoelectrons is given by the photoemission horizon (eq. 2.3). For static photoemission spectroscopy, the maximal accessible energy is determined by $E_{\text{kin}}^{\text{max}} = h\nu - \phi$. Panel a) and b) are taken from [33].

The measured photoemission intensity can be written as [33]

$$I(\mathbf{k}, E) = I_0(\mathbf{k}, \nu, \mathbf{A}) A(\mathbf{k}, E) f(E, t). \tag{2.4}$$

where $I_0(\mathbf{k}, \nu, \mathbf{A}) \propto \sum_{f,i} |M_{f,i}^k|^2$ is expressed by the photoemission matrix element $M_{f,i}^k = \phi_f^k |\mathbf{A} \cdot \mathbf{P}| \phi_i^k$, describing the transition from the electron ϕ_i^k in the initial state to the final state ϕ_f^k including the vector potential $\mathbf{A}$ and the electronic momentum operator $\mathbf{P}$. This photoemission matrix element directly depends on the orbital geometry and the wavefunctions and can lead, e.g., to a suppression of the photoemission intensity for specific orbital geometries with respect to the incidence plane [37, 38]. A(**k**, E) describes the one-particle spectral function, containing information about the quasiparticle self-energy, which defines many-body interaction effects and partly the bandwidth of the electronic bands [34]. The last term $f(E,t) = \frac{1}{1+\exp((E-E_F)/k_B T)}$ describes the Fermi-Dirac distribution at a certain temperature T. Thus, the measured photoemission intensity $I(\mathbf{k}, E)$ provides access to the described quantities.

One additional property of the ARPES experiment is the extremely high surface sensitivity. During their propagation to the surface, the excited electrons experience inelastic scattering events, whereby the kinetic energy of the electrons decreases. The mean-free path of the electrons as a function of the kinetic energy is largely independent of the material and can be described by the universal-curve of the inelastic mean free path, shown in Fig. 2.1.2 [31]. The mean free path is the reason for the strong surface-sensitivity of the photoemission experiment. As a consequence, ARPES experiments require very clean surfaces and therefore excellent vacuum conditions in the range of 10^{-10} mBar and additional sample preparation such as annealing or sputtering of the sample are necessary.

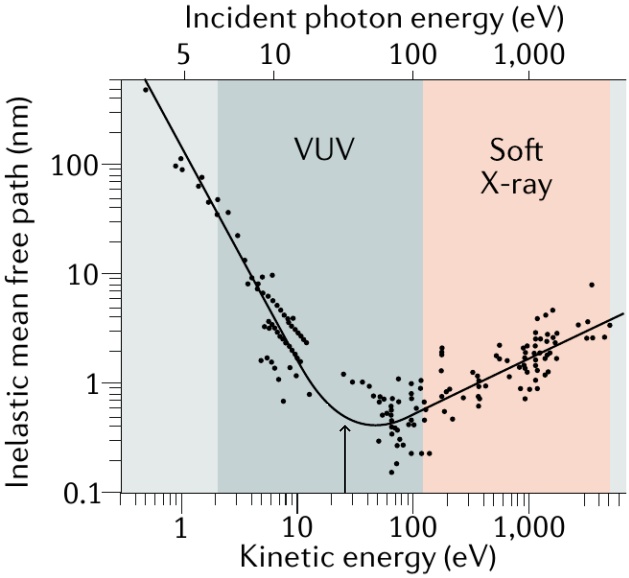

Fig. 2.1.2.: Universal-curve of the inelastic mean free path. The mean free path corresponding to the given probe photon energy of the experiment (=26.6 eV) is around 0.5 nm (indicated by an arrow). Image adapted from [34].

In summary, the ARPES experiment is able to measure the photoemission intensity $I(\mathbf{k},E)$ as a function of the in-plane momentum $k_{||}$ and energy E of the photoemitted electrons. These quantities can be measured by different kinds of experimental realizations involving, e.g., commonly used 1D/2D hemispherical analyzers, where the sample or detector has to be rotated to map certain directions in momentum-space. The measurements in this work are performed with a time-of-flight momentum microscope, a very recent development that is able to measure the two in-plane momentum coordinates (k_x, k_x) and the kinetic energy simultaneously [35]. In that way, this approach gives direct access to the 3D band structure of the sample, as demonstrated for a static photoemission spectrum of n-doped graphene in Fig. 2.1.3. The experimental schematics of this approach is detailed in the appendix A.

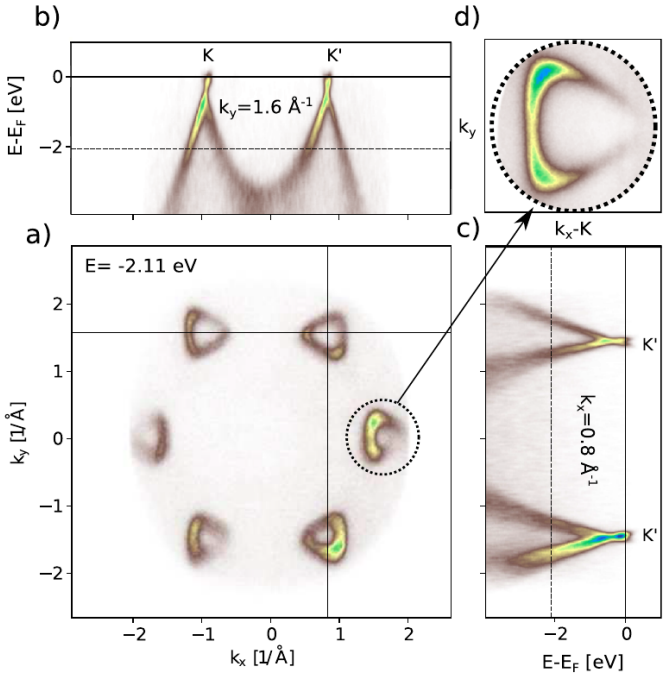

Fig. 2.1.3.: Static momentum microscopy of graphene. The multidimensional detection scheme allows the extraction of isoenergetic momentum-momentum planes a), energy-momentum cuts b), c) and also larger magnification of selected regions in momentum-space d) within the photoemission horizon. Image obtained from [29].

2.2. Time-resolved ARPES

So far, static ARPES has been discussed as an elegant way to directly map the occupied band structure and the equilibrium spectral function [32]. The extension to time-resolved ARPES (trARPES) allows the measurement of the temporal evolution of the non-equilibrium material properties with energy and momentum resolution. It can be realized by adding a pump-probe scheme to the ARPES experiment. The pump beam, with photon energies usually below the work function of the material, creates a non-equilibrium distribution of excited electrons (c.f. Fig. 2.2.1 a)), where the electrons are excited in the unoccupied regions of the band structure. In order to restore its equilibrium state, the electron system experiences energy dissipation processes by interacting with other electrons, the spin system or the lattice (phonons). All these interactions can be attributed to certain timescales (c.f. Fig. 2.2.1 b)). E.g., the timescale for electron-electron interaction is typically in the order of femtoseconds, whereas the electron-phonon timescale is usually in the order of femto- to picoseconds [39]. The large photon energy probe beam now photoemits the non-equilibrium charge carrier distribution. By varying the pump-probe-delay, a movie of the electron dynamics can be generated and, thus, the timescales and coupling strength of the interactions can be examined.

In this way, trARPES provides access not only to the unoccupied band structure [40, 41] but also to the strength and type of energy dissipation channels [42, 43] that are usually difficult to determine in the equilibrium case. Beside the investigation of electron dynamics, the trARPES experiment can among others be used to investigate ultrafast phase transitions [44, 45], charge transfer processes [46, 28], phonon oscillations [47], renormalization effects [48, 49], many-body particle interactions [50] and coherent electron-light coupling [51, 52, 53, 54].

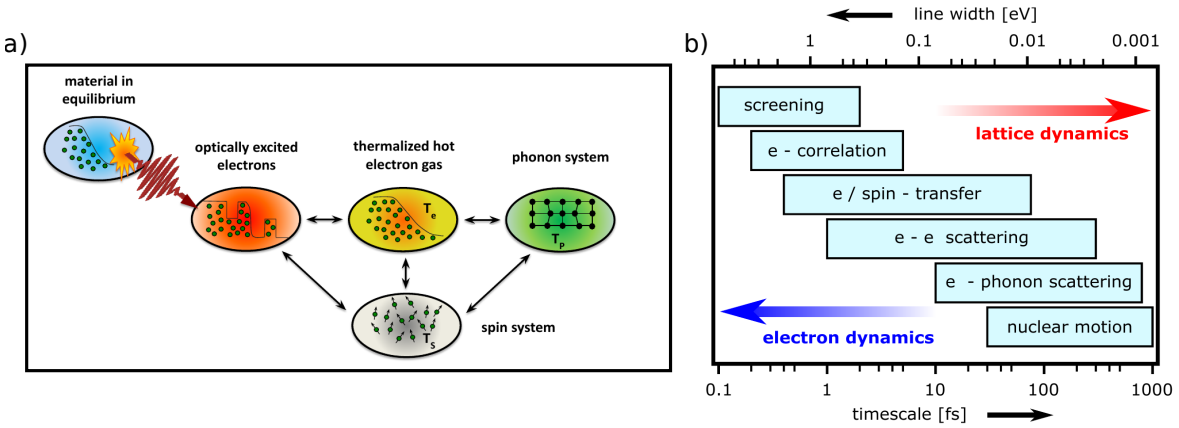

Fig. 2.2.1.: a) Schematic overview of different interactions during and after optical excitation of the material. b) Corresponding timescales and line widths of different interaction types. Image b) adapted from [39] and [55].

The direct access of trARPES to the transient band structure dynamics is exemplified in Fig. 2.2.2 for n-doped graphene [29, 56]. In typical trARPES experiments, the non-equilibrium situation is created by exciting electrons into the unoccupied band structure with a pump pulse (red arrow) and the electronic structure and occupation is then probed by the probe pulse (blue arrow). In the trARPES experiment, the excited electrons can be directly tracked as a function of the pump-probe delay, which allows to create a movie of the electron dynamics with momentum and energy resolution. Applying the pump-probe scheme to the time-of-flight momentum-microscope allows tracking of the 3D band structure dynamics as a function of pump-probe delay (c.f. Fig. 2.2.2 b)).

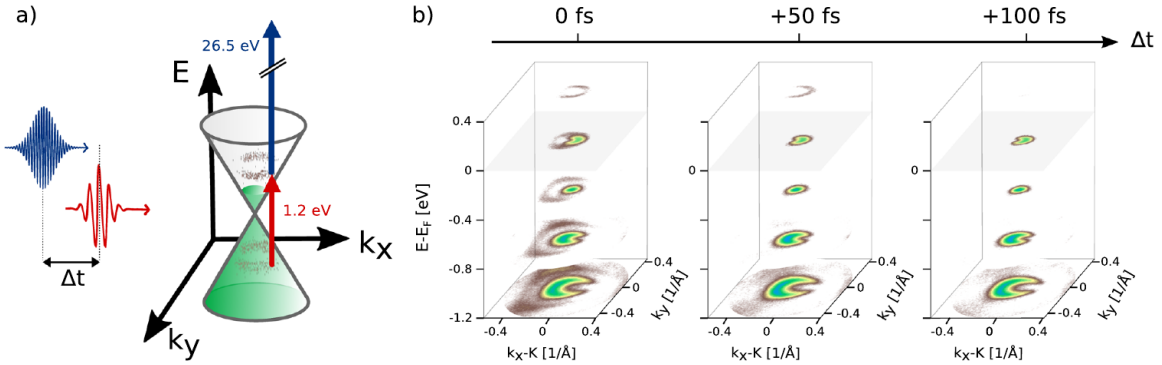

Fig. 2.2.2.: Time-resolved momentum microscopy of graphene. a) The pump pulse (red arrow) creates a non-equilibrium distribution by exciting electrons into the unoccupied band structure, which is then probed by the EUV pulse (blue arrow). By varying the pump-probe delay Δt, the dynamics after excitation can be tracked. b) Time-resolved momentum microscopy allows tracking of the 3D band structure dynamics as a function of pump-probe delay. Image obtained from [29].

2.3. Introduction to TMDs

The material class of TMDs is the main sample system investigated in this PhD-thesis. It offers a wide range of scientifically interesting physical properties, such as strong spin-orbit coupling [57], exotic phases ranging from CDW- [44, 47], Mott [58], superconducting-, correlated, and topological-phases [59, 60, 61]. In the 2D limit, the class of TMDs exhibits new physical properties different from their 3D bulk structures [62]. It was shown that MoS_2 and WSe_2 monolayers host excitons with large binding energies of up to 500 meV [3]. Because of that, the optical properties and dynamical response of WSe_2, WS_2, $MoSe_2$ and MoS_2 monolayer TMDs are dominated by exciton dynamics. The examination of the exciton energy landscape and exciton dynamics of TMDs is the key aspect of this PhD-thesis. Therefore, the following sections will provide an introduction to the material class of TMDs, with an emphasis on the excitonic properties. Further information on TMDs and their potential application can be found in recent review articles [59, 63, 64, 65].

2.3.1. TMD lattice structure

The TMD atomic structure consists of transition-metal (e.g., M = Mo, W) and chalcogen (e.g., X = S, Se) atoms in the chemical form of MX_2. There are two typical polytypes of monolayer TMDs, the trigonal prismatic (2H) and the octahedral (1T) coordination [59]. In this work, only the trigonal prismatic (2H) coordination is used, which corresponds to an ABA stacking of the chalcogen and the transition metal layer (cf. Fig. 2.3.1 a)). In bulk TMDs, weak van-der-Waals interactions define the bonding of different MX_2 layers (cf. Fig. 2.3.1 b)).

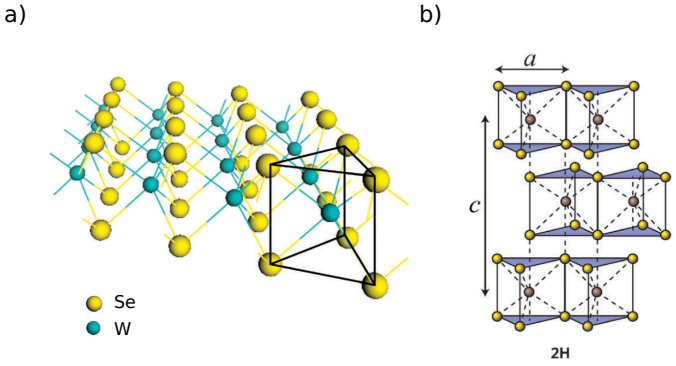

Fig. 2.3.1.: a) Lattice structure of 2H-WSe_2, where the yellow and green points indicate the selenium and tungsten atoms, respectively. b) Structure of bulk WSe_2 in a 2H-configuration, where the layers are coupled by weak van-der-Waals forces. Both images obtained from [66].

2.3.2. TMD electronic structure

The semiconducting TMDs WSe_2, WS_2, $MoSe_2$ and MoS_2 exhibit a very similar single-particle band structure. As an example, the (2H)-bulk a) and monolayer b) WSe_2 band structures are shown in Fig. 2.3.2 [67]. For both cases, two valence bands at the K-valleys can be found, which are energetically separated by Δ_{VB}. Theoretical and experimental studies have shown that these separated valence bands have opposite spin-polarization [68], which is a result of the strong spin-orbit interaction. Due to time-reversal symmetry, the spin-directions of the upper and lower valence band are reversed at the K'-valleys (not shown here), which gives rise to the spin-valley polarization and distinct transition rules observed in these materials [68, 69]. While the valence bands are significantly separated of about 500 meV [28, 70, 25], the conduction bands at the K-valley show a smaller energy separation (Δ_{CB}). Due to hybridization, the valence bands at the Γ-point and the conduction band at the Σ-point are drastically different between bulk and monolayer WSe_2. At the Γ-valley, a series of hybridized valence bands are observed for the bulk case, which are forming the overall valence band maximum. In the monolayer case, only a single band is observed at lower energies and the valence band maximum is located at the K-valley. For the conduction band at the Σ-valley, the hybridization in the bulk leads to an energetic down shift of the conduction band in comparison to the monolayer case. The apparent differences in the electronic band structure between bulk and monolayer TMDs strongly influence the optical properties of these materials. In particular, the single-particle band gap changes from indirect (bulk) to direct (monolayer).

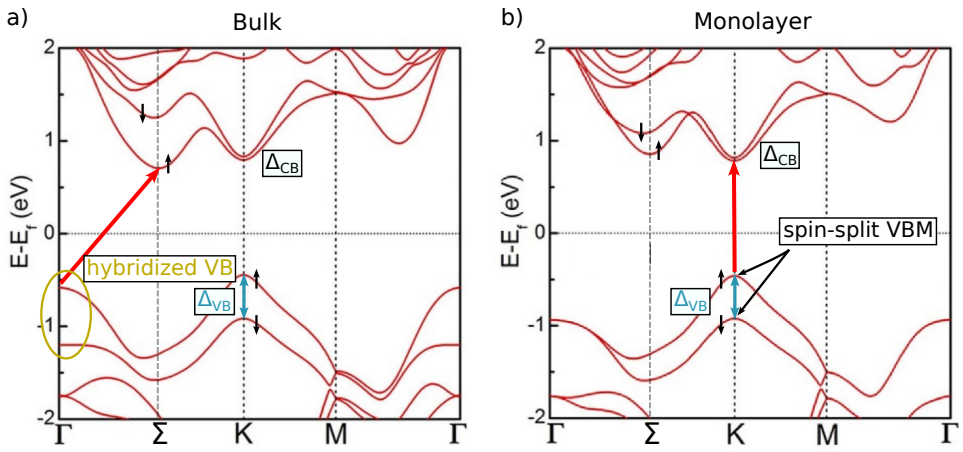

Fig. 2.3.2.: Electronic band structure of a) bulk and b) monolayer WSe_2. The spin-split valence band maximum (VBM) at the K-point (blue arrow), the bulk hybridized valence bands at the Γ-valley (yellow circle) and the indirect/direct band gaps (red arrow) are indicated. Both images adapted from [67].

2.3.3. TMDs in the monolayer limit

Scaling the thickness from bulk TMD to monolayer TMD dramatically changes the single-particle band structure, as shown in the last section. An additional consequence of the monolayer limit is the strongly reduced dielectric screening of the environment (cf. Fig. 2.3.3 a)), which gives rise to enhanced Coulomb interaction, providing the existence of tightly-bound electron-hole pairs, so-called excitons, after optical excitation with large binding energies up to $\approx$ 500 meV [3] (cf. Fig. 2.3.3 b)). Beside the large binding energies for these excitons, also a series of further exciton states were observed in monolayer TMDs [12], reflecting the excitonic Rydberg series in analogy to the hydrogen model (c.f. Fig. 2.3.3 c)). These large binding energies facilitate the access to exciton signatures by many experimental means, but in particular for time-resolved ARPES experiments, where the energy resolution is typically on the order of a few hundred meV [29].

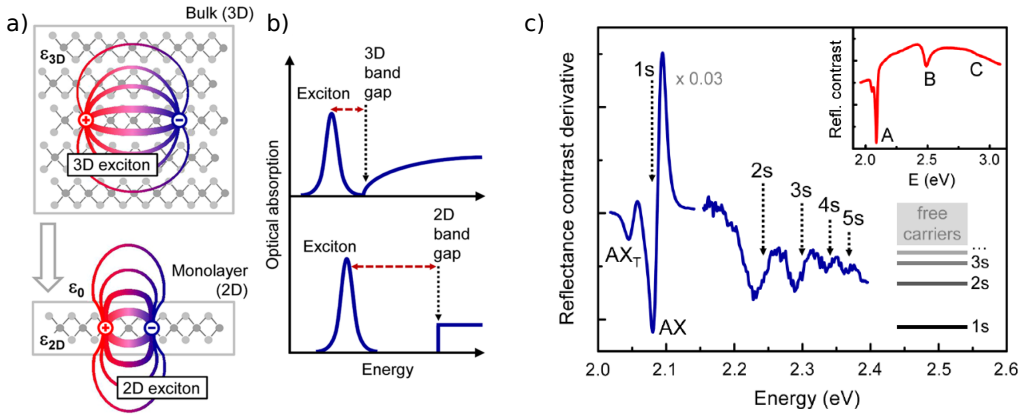

Fig. 2.3.3.: a) Electron-hole interaction in bulk and monolayer TMDs. In the latter case, the electric field passes the vacuum permittivity ε_0 and is therefore much less affected by screening, whereas in the bulk case these field lines are screened by the much higher permittivity of ε_{3D}. b) Schematic optical absorption profiles from the respective materials. In both profiles, exciton signatures can be identified, but in the monolayer limit the respective binding energy (red dashed line) is much larger than in the bulk case. c) Exciton Rydberg series of WS_2. Images obtained from [12].

2.4. Energy landscape and dynamics of excitons in TMDs

Due to the large binding energies of excitons, the optical response of TMDs is strongly determined by the formation, thermalization and recombination of excitons. The processes are defined within the exciton landscape, which is the exciton equivalent of the electronic band structure. Such exciton landscapes typically exhibit multiple exciton states and can be very complex, especially in the case of TMD heterobilayers. Therefore, this section provides an overview of the exciton landscapes and exciton dynamics found in monolayer and heterobilayer TMDs. After that, the possible influences of disorder on the exciton landscape are presented. Finally, experimental techniques providing access to exciton states are briefly reviewed.

2.4.1. Exciton dispersion relation

Due to the Coulomb interaction of the electron-hole pair, the energy of the exciton is reduced in comparison to the single-particle band gap. The energy dispersion of the exciton is given by [71]

$$E_{\mathrm{exc}}(\mathbf{Q}) = E_g - E_B + \frac{\mathbf{Q}^2}{2M}, \tag{2.5}$$

where E_g corresponds to the single-particle band gap and E_B is the exciton binding energy. The last term describes the kinetic energy of the exciton which is parametrized by the kinematic center-of-mass momentum $\mathbf{Q}=\mathbf{k}_\mathrm{e}+\mathbf{k}_\mathrm{h}$, defined by the momentum positions of the electron $\mathbf{k}_\mathrm{e}$ and hole $\mathbf{k}_\mathrm{h}$ with respect to their corresponding valley in the Brillouin zone [72, 73]. The exciton mass M is given by the sum of the respective effective masses of the electron in the conduction band $\mathrm{m_e}$ and the hole in the valence band $\mathrm{m_h}$. Experimental studies of TMDs indicate a long-range coupling of the electron-hole pair, such that the excitons can be described as Wannier-Mott-excitons. In that case, the exciton can be described in analogy to the hydrogen-atom and the binding energy can be expressed as a Rydberg-series of exciton states [12]. Similarly, the size of the exciton is described by the Bohr-radius. As the exciton energy is given as a function of the kinematic center-of-mass momentum, it is useful to characterize the exciton landscape by this coordinate.

2.4.2. Bright and dark excitons

Fig. 2.4.1 shows how the electron-hole single-particle band structure picture can be translated into the exciton energy landscape as a function of the center-of-mass momentum. For K-K-excitons, the electron in the conduction band and the hole in the valence band are located at the same K-valley in momentum space (Fig. 2.4.1 a)) (Hence the name K-K-excitons, where the first letter describes the momentum position of the hole and the second letter the position of the electron). The respective exciton parabola (eq. 2.5) is located at zero center of mass-momentum. A direct resonant optical excitation and recombination of excitons is only

possible for small center-of-mass momenta $Q \leq q_{photon} \approx 0$ within the light cone (yellow cone in 2.5 b)). Excitons, where such a direct optical excitation is possible, are also called bright excitons. Beside the bright excitons, there are also dark excitons, e.g., momentum-indirect excitons where the electron and the hole contributions are situated at two different positions in momentum space, as shown in Fig. 2.4.1 a) for a K-Σ-exciton. According to equation 2.5 the center-of-mass momentum **Q** describes the relative momentum of the electron and hole with respect to their valley, i.e. for **Q**=0, the K-Σ exciton is at the energetically lowest point of the exciton parabola, while the electron and hole are located in different valleys. For momentum-indirect excitons, another terminology of the center-of-mass-momentum is often used, where the valley momenta of the electron and hole are taken into account. In this notation, Q=0 is defined by the position of the light cone and the momentum-indirect excitons are shifted by the difference of the respective valley momenta of the electron and hole (c.f. Fig. 2.4.1 b)). Because of the momentum-indirect nature of the K-Σ-exciton, direct optical excitation and the radiative recombination are not possible for the K-Σ-exciton (c.f Fig. 2.4.1 b)). As a consequence, the radiative recombination is suppressed, leading to long-lived dark excitons and further, a population of dark excitons is only possible by scattering processes from bright to dark excitons [24].

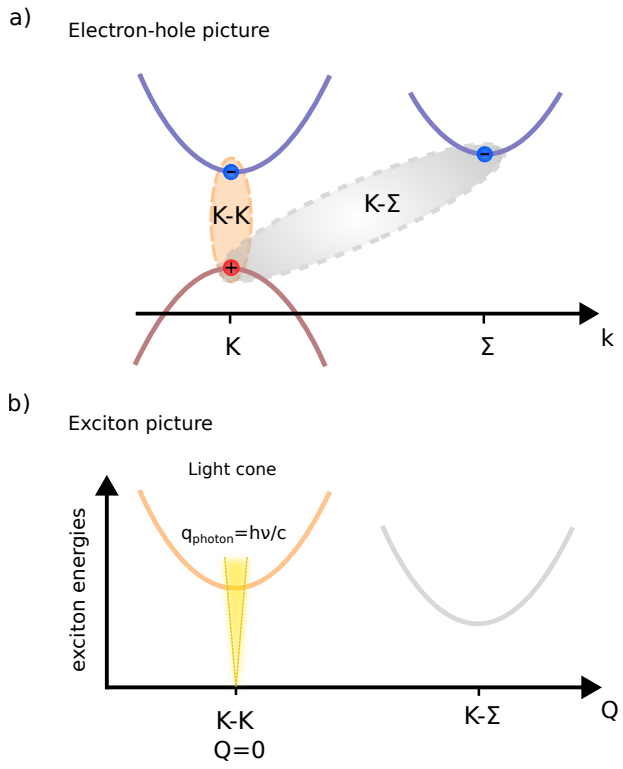

Fig. 2.4.1.: a) Exemplary bright K-K exciton and a dark K-Σ excitons visualized in the electron-hole picture. b) Respective exciton landscape as a function of the center-of-mass momentum Q. The light cone is indicated by a yellow cone at Q=0. Image inspired by [74].

2.4.3. Exciton landscape of monolayer TMDs

TMD monolayers feature a rich exciton landscape, including different kinds of bright and dark intralayer excitons. In WSe_2-monolayer, beside the bright K-K-excitons (c.f Fig. 2.4.2 a) orange shading) situated at the K-valley, also the momentum-dark K-Σ-exciton and K-K'-excitons can be observed, where the electron of the exciton is located at the Σ-valley and in the K'-valley conduction band, respectively, and the hole remains at the K-valley valence band (c.f Fig. 2.4.2 a) gray-shading: K-Σ, orange light shading: K-K'-excitons).

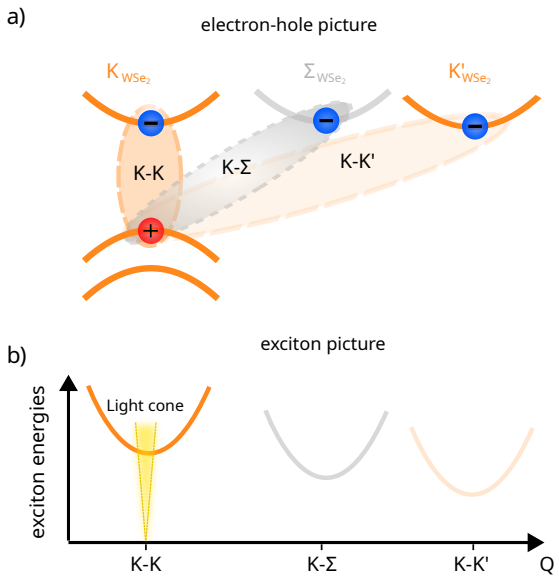

Fig. 2.4.2.: b) Schematics of the typical single-particle energy landscape of the valence and conduction bands of a WSe_2 monolayer. Beside bright intralayer excitons (Coulomb interaction pictured as orange shading), there are other types of intralayer excitons such as the momentum-indirect dark exciton (gray shading: KΣ-exciton, light-orange shading: KK'-excitons), defining the overall exciton landscape. c) Respective exciton landscape. The light cone (yellow) is located in the bright K-K-exciton.

Because of the energetically lower K-Σ-exciton and K-K'-exciton, the optically bright K-K exciton can decay into the respective excitons [8, 24, 25]. Interestingly, due to the higher energy position of the conduction band at the Σ-valley compared to the K-valley, the scattering process in the electron-hole band structure would involve an uphill process but because of the larger binding energy of the K-Σ exciton the scattering process is energetically favorable in the exciton landscape. However, the exact energy alignment of the single-particle band structure and the exciton landscape depends strongly on the considered sample system. In monolayer MoS_2 for example, the K-Σ excitons are energetically above the K-K excitons, whereby the K-Σ excitons cannot be populated [28, 75] (c.f. chapter 3, Fig. 3.0.9).

2.4.4. Exciton landscape of TMD heterostructures

The vertical stacking of two similar (homobilayer) or different (heterobilayer) monolayer TMDs gives rise to new physical properties extending the properties of the respective monolayers [62]. Because of the exciting opportunities to tailor TMD heterostructures with desired functionalities on demand, these structures came into the focus of current research [4]. Also in these heterostructures, the optical response is governed by excitons. The presence of a second layer introduces new exciton states, leading to a more complex exciton landscape. This section focuses on the exciton landscape of a type-II aligned WSe_2/MoS_2 heterostructure (see Fig. 2.4.3), the main sample system studied in this thesis.

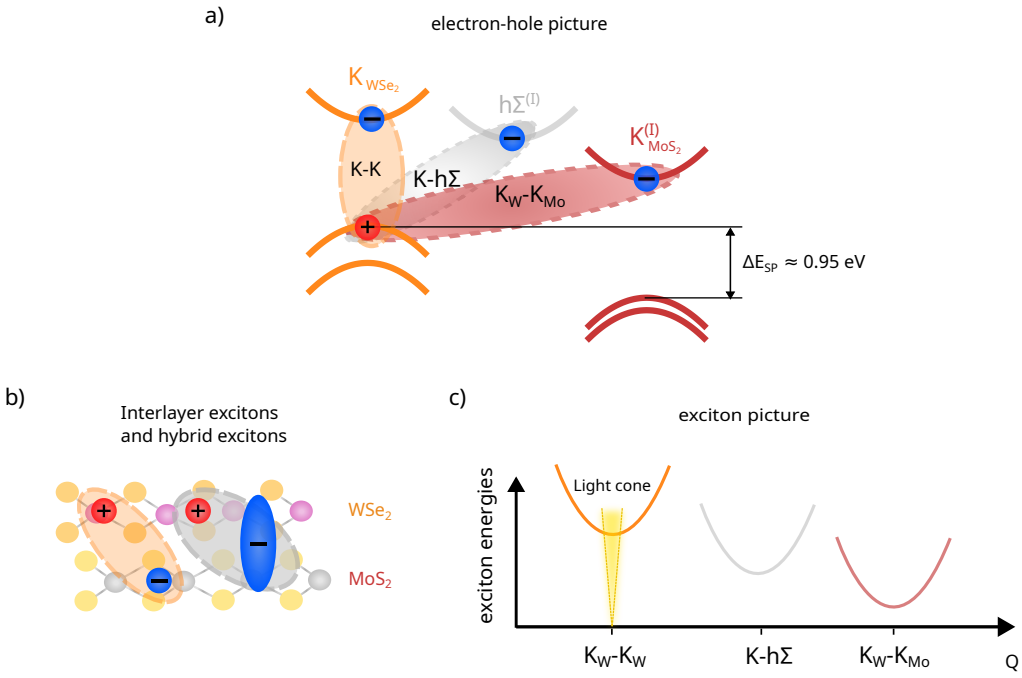

Fig. 2.4.3.: a) Single-particle energy landscape of the valence and conduction bands of a WSe_2/MoS_2 heterostructure in a type-II (Δ $E_{SP} = 0.95$ eV) configuration. Beside the intralayer exciton states shown in Fig. 2.4.2 and additional intralayer exciton states of MoS_2 (not shown here), the heterostructure exhibits pure interlayer excitons (red-shading), where the hole is located in the WSe_2-layer and the electron in the MoS_2-layer. Also, hybrid exciton states with a mixture of intra- and interlayer excitons can be formed (gray-shading: K_W-Σ-exciton). b) Schematic illustration of interlayer and hybrid excitons in the WSe_2/MoS_2 heterostructure. c) Respective exciton landscape. The light cone (yellow) is located in the bright K_W-K_W-exciton. Note that the landscape of the heterostructure also involves further intralayer exciton states, which are not shown here.

The exciton landscape of a type-II aligned TMD heterostructure includes different kinds of intralayer- (1), interlayer- (2) and hybridized (3) excitons, which are discussed in the following.

(1) Intralayer excitons:
In the case of the WSe_2/MoS_2 heterostructure, the valence and conduction bands at the K-valleys are mostly not affected by the stacking of the monolayers (see point 3). As a consequence, the intralayer bright K_W-K_W, K_{Mo}-K_{Mo}-excitons and the dark K_W-K'_W, K_{Mo}-K'_{Mo}-excitons are still present in the heterostructure (c.f. Fig. 2.4.4 b)). Because of the different exciton energies of the bright excitons of 1.7 eV for WSe_2 and 1.9 eV for MoS_2 [28, 76, 8], the resonant excitation of the bright WSe_2 exciton cannot generate a population of the bright MoS_2 exciton.

(2) Interlayer excitons:
The energy alignment of the WSe_2 and MoS_2 monolayer in a type-II configuration, as shown in Fig. 2.4.3, allows the charge transfer of electrons or holes from one layer to another layer. The charge transfer allows the formation of so-called interlayer excitons, where the electron is located in the MoS_2 layer and the hole remains in the WSe_2 layer (Fig. 2.4.3 a), b)). Because of the large energy offset of the type-II band alignment, the interlayer exciton energy is much smaller compared to other exciton energies in the system. As a consequence, the interlayer exciton presents the energetically lowest state in the exciton landscape and, thus, contributes significantly to the exciton dynamics. Due to the spatial separation between the electron and hole, the Bohr radius of the interlayer exciton is larger and the binding energy is smaller compared to the energy of the intralayer exciton (130 meV for a WS_2/WSe_2 heterostructure [77]). The spatial separation of the electron and hole and the large center-of-mass momentum (due to the lattice mismatch and/or rotation of the layers) of the interlayer excitons increases the lifetime of interlayer excitons significantly [78]. Beside the K_{Mo}-K_W interlayer excitons shown in Fig. 2.4.3 the material also features Γ-K_{Mo} interlayer excitons [79]. Interlayer excitons can be generated by first exciting the bright WSe_2 or MoS_2 excitons and, dependent on the respective excitations, either electrons or holes perform the charge transfer to the other layer. The exact charge-transfer mechanism for the formation of interlayer excitons is still under debate, and experimental identification is barely available [77, 28, 16, 76] (see section 2.4.6).

(3) Hybridized excitons:
The introduction of a second layer creates hybridization effects. The hybridization is determined by the wavefunction overlap between the two layers, which defines the interlayer interaction and tunneling strength [80]. The electronic wavefunction of the K-valley valence and conduction bands of TMDs have mostly an in-plane orbital character (d-orbitals) located between the two selenium atoms (c.f. Fig. 2.4.4 b)). The respective interlayer tunneling strength is on the order of a few meV [7] and thus the bands are not affected by the presence of the added layer (2.4.4 a) left panel). On the other hand, the Σ- and Γ-valley valence and conduction bands are defined by orbitals with out-of-plane components, where significant orbital overlap is expected between the two layers, resulting in a much larger tunneling strength

of about 170 meV [7]. The hybridization of these orbitals causes energy shifts of the bands at the respective valleys and allows the creation of hybrid exciton states [6], where the wave function of the exciton is a mixture of intra- and interlayer contributions and the respective hole and electron wavefunctions are distributed over both layers (c.f. Fig. 2.4.3). The degree of the hybridization of an exciton state is defined by the ratio of the intralayer contribution and the interlayer contribution to the wavefunction. The degree of the hybridization is maximal (=1) if there is a 50%-50% mixture of intralayer and interlayer exciton contributions, and minimal (=0) for purely intralayer or interlayer exciton states. Beside the direct influence on the exciton landscape, the degree of the hybridization determines scattering processes and especially the efficiency of charge transfer between the layers [6, 28, 8, 30]. The degree of the hybridization depends on multiple points: the material composition, the considered orbitals [7], the relative energy and momentum alignment [6] and the quality of the sample [30].

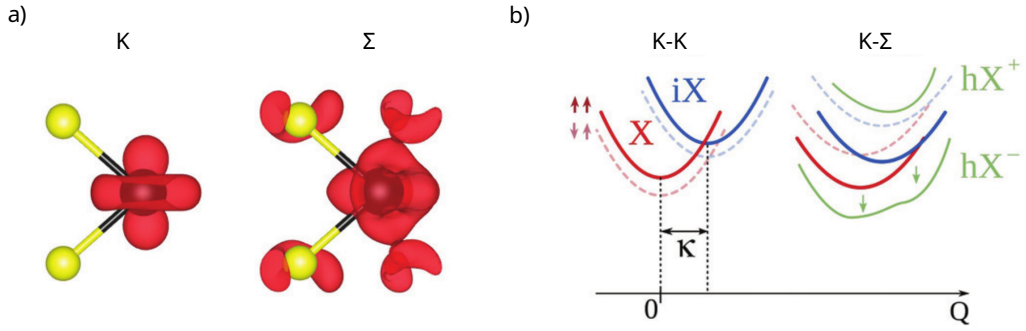

Fig. 2.4.4.: a) Orbital character of the conduction bands of the K-valley (left) and Σ-valley (right). The charge density for the K-valleys is located between the selenium atoms (yellow points), whereas the Σ-valley charge density is also found at the selenium atoms, which leads to an enhanced orbital overlap between the two layers. b) Because of the low interlayer tunneling strength at the K-valleys, the pure interlayer (iX) and intralayer (X) excitons show negligible hybridization, whereas the K-Σ (hX^+ and hX^-, green) excitons are strongly affected by hybridization. As a reference, the K-Σ exciton dispersion without hybridization are shown in red and blue curves. Images a) and b) are taken from [7].

2.4.5. Moiré excitons

Another great oppurtunity of TMD heterostructure comes by the possibility to introduce a twist angle between the respective layers, which has opened the research field called 'twistronics' [81, 17, 5]. The relative twist of the layers and also the different lattice constants of the two layers leads to a long-range periodic super structure, the so-called moiré structure. Inside the moiré structure, different atomic registrations can be found, which lead to an effective variation of the potential landscape in real-space [10] (c.f. Fig. 2.4.5 b), c)). Dependent on the size and depth of the moiré potential, excitons can be manipulated or even confined within the moiré potential. The confinement of excitons holds great promise to built up, e.g., programmable quantum emitters [82] and exciton crystals [11]. The moiré structure has huge impact on the exciton landscape of intra-, inter- and hybrid-excitons, which will be the subject of this section.

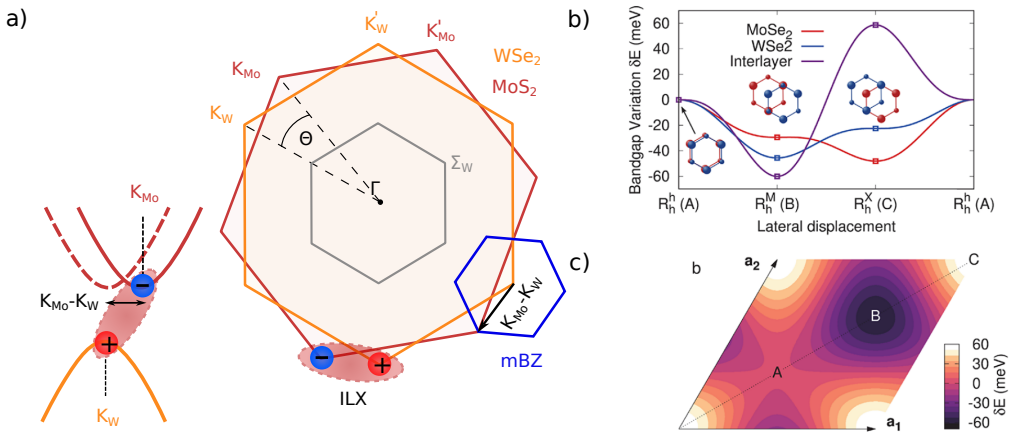

Fig. 2.4.5.: a) The relative twist θ of the Brillouin zones in momentum-space creates mini Brillouin zones (blue hexagon). The momentum offset gives rise to momentum-indirect interlayer excitons (ILX). b) The relative twist in the real-space leads to different atomic registrations and hence to a varying potential landscape, directly affecting the intra/interlayer band gap across the moiré unit cell, shown in c). Image a) is adapted from [83], b) and c) are obtained from Brem *et al.* [10].

Size of the moiré unit cell:
In the case of the heterobilayer, the rotation (or lattice mismatch) of the hexagonal unit cells of the two layers leads to a new hexagonal moiré structure with a larger moiré unit cell. With smaller relative twist angles, the periodicity of the moiré structure increases. The size of the moiré unit cell can be approximated by [80]

$$L_{\text{moire}} = \frac{a_0}{\sqrt{\theta^2 + \varepsilon^2}}, \tag{2.6}$$

where a_0 is the monolayer lattice constant, θ describes the relative twist and ε the relative lattice mismatch $|a_0 - a_0'|/a_0$ of the respective layers. Consequently, the size strongly depends on the twist angle and the heterostructure composition. For similar lattice constants of the two constituents and small twist angles, the size of the moiré unit cell can be in the range of 100 nm, whereas for larger lattice mismatches, such as WSe_2/MoS_2 investigated in this work, the largest moiré unit cell is in the range of about 8 nm [83].

Moiré excitons and exciton confinement
The different atomic registries inside the moiré cell lead to a variation of the potential landscape in real-space. The varying potential directly affects the intra-/interlayer single-particle band gaps (cf. Fig. 2.4.5 b), c)) and the respective exciton energies [10]. The dispersion of intra- and interlayer excitons in reciprocal space is described within the so-called moiré mini Brillouin zone (mBZ), which can be constructed by the respective reciprocal lattice vectors of the two layers (cf. Fig. 2.4.5 a) blue hexagon). Because of the periodicity of the moiré potential, all intra- and interlayer exciton bands can be back-folded into the first mBZ, resulting in a series of moiré minibands. The presence of a deep interlayer moiré potential leads to the formation of flat minibands, caused by interlayer exciton confinement within the moiré potential. It also has been shown that intralayer excitons are strongly affected by the moiré potential [10]. For increasing twist angles, the periodicity of the moiré unit cell decreases (c.f. eq. 2.6). The short-range periodicity facilitates the hopping of excitons between the moiré unit cells and leads to a more parobola-like dispersion of the exciton states (free particle like), where confinement effects of the moiré potential can be neglected. Experimentally, the presence of moiré minibands were confirmed, and it was shown that the mixing of inter and intralayer exciton within the mBZ creates hybridized exciton states [14].

Moiré excitons for larger twist angles
Due to the confinement of excitons and their manipulation within the moiré potential, most experimental studies have focused on TMD structures with small twist angles and deep moiré potentials. For larger twist angles, such confinement effects are negligible. However, the twist of the respective layer causes a twist of the respective Brillouin zones, as shown in Fig. 2.4.5 a), leading to an increased momentum displacement of the respective K-valleys. As a consequence, the interlayer exciton becomes more momentum indirect and because of that, the lifetime of the interlayer exciton is strongly enhanced with increasing twist angle [17]. The momentum-displacement also affects the degree of hybridization at the Σ-valley, which can have direct consequences on the formation process of interlayer excitons [6] (see next section). Further impact of larger twist angles on inter- and intralayer excitons remained so far elusive, because most experimental techniques are fairly limited to small twist angles (small momentum offsets). The first article of this thesis shows how the presence of (large) moiré mini Brillouin zone leads to distinct fingerprints in the momentum distribution of the interlayer exciton.

2.4.6. Dynamics of excitons

So far, the exciton landscapes of monolayer and (twisted) heterobilayer TMD structures were described, including bright and dark intralayer, interlayer and hybrid exciton contributions. For the potential application of TMDs as optical devices, it is important to examine the dynamical response of excitons including the formation, thermalization and the recombination processes of excitons after optical excitation, which is directly determined by the specific exciton landscape. Because the exciton dynamics involve the formation of dark exciton states, the experimental identification of the scattering and formation processes is challenging. As a consequence, there are major open questions from theoretical and experimental side. One of these questions concerns the exact mechanism responsible for the formation of interlayer excitons in TMD heterostructures, which is one of the central points investigated in this thesis [28]. This section provides an overview of the exciton dynamics of monolayer WSe_2 and the WSe_2/MoS_2 heterostructure. Further information on exciton dynamics can be found in ref. [84, 5, 85].

Exciton dynamics of monolayer WSe_2:
The exciton dynamics of monolayer WSe_2 has been investigated by trARPES experiments [24, 8], which allow to track the energy and momentum distribution of the exciton population with femtosecond temporal resolution. In those experiments, the pump pulse is tuned to the optical band gap of the bright K-K-excitons. When optically excited, the K-K exciton population starts to build up rapidly (c.f. Fig. 2.4.6 b)), which includes a coherent exciton polarization and the dephasing to incoherent excitons [86, 25, 85]. By increasing the pump-probe delay the K-K exciton population decreases and, concomitant, photoemission yield at the Σ-points starts to build up, indicating the build-up of a population of the energetically lower K-Σ-excitons (c.f. Fig. 2.4.6 a)) in the first 100 fs [8]. By comparing the experimental data with theoretical calculations, it was shown that exciton-phonon scattering is responsible for the formation of K-Σ-excitons [25, 27, 85, 28, 8]. Because of the large center-of-mass momentum, the radiative recombination of K-Σ-excitons is strongly suppressed. However, in a recent publication [8] it was shown that, because of the small energy difference between K-K'-excitons and K-Σ-excitons of around 70 meV, an efficient backscattering from KΣ-excitons to bright excitons is possible, resulting in a steady-state $K \leftrightarrow \Sigma$ between both exciton populations. The backscattering of K-Σ to K-$K^{(I)}$-excitons leads to a refilling of the K-$K^{(I)}$-exciton and enables the decay of K-Σ-excitons [8].

Exciton dynamics of TMD heterostructures:
Due to the presence of hybrid and interlayer excitons, the formation, thermalization and recombination of the incoherent exciton occupation is much more complex and challenging to access experimentally. The formation of interlayer excitons draws interest to the first pump-probe experiments and theoretical studies [87]. All-optical experiments were able to measure the timescale of the formation process of the interlayer excitons. For the WSe_2/MoS_2 heterostructure, Zhu *et al.* found a charge-transfer time of the K_W-K_{Mo} interlayer exciton of around 40 fs [88], consistent with later experiments on the same sample system [89, 30]. In order to describe the ultrafast interlayer exciton formation, theoretical studies suggest two

possible charge transfer mechanisms: Direct interlayer tunneling (1) and interlayer charge transfer through hybrid exciton states (2). In the first case, the electrons (or holes) of the intralayer excitons directly tunnel from the respective bands at the K_W (K_{Mo})-valleys to the K_{Mo} (K_W)-valleys. Due to the localized orbitals at the K-valleys, the interlayer coupling strength is relatively weak (see section 2.4.4), which could slow down the formation process and could cause a strong twist-angle dependence. This model could successfully describe the ILX formation in a WSe_2/WS_2 heterostructure measured by mid-infrared spectroscopy [77]. The second process takes the strong hybridization effects at the Σ- and Γ-valleys into account. Because of the hybridization at these points in the Brillouin zone, the interlayer coupling strength is much larger than in the K-valleys (see section 2.4.4), which facilitates a fast charge transfer. Following this model for the WSe_2/MoS_2 heterostructure, the electron contribution of the bright exciton at the K_W-valley is first scattered to the hybrid hΣ excitons by exciton-phonon scattering, where an efficient charge transfer takes place and after that a second phonon translates the electron to the K_{Mo}-valley to form the K_W-K_{Mo} interlayer exciton. Until now, this model was applied to explain some of the experimental observations [88, 16, 90], but so far the direct experimental identification of this charge process remained elusive. The present work provides first trARPES data, that is able to directly follow the interlayer exciton formation process by monitoring the temporal evolution of the electronic contribution of intralayer, hybrid hΣ and the interlayer excitons with femtosecond temporal resolution. The charge transfer is corroborated with a full microscopic model, which is in excellent qualitative agreement with the experimental data [28].

Fig. 2.4.6 b) (lower panel) shows the temporal evolution of the electronic parts of the bright WSe2 K_W-K_W exciton, the dark hΣ exciton and the ILX, as measured with the trARPES experiment. Similar to the monolayer WSe_2, the bright K_W-K_W exciton signal increases almost immediately during pump-probe overlap. However, in contrast to the monolayer WSe_2 dynamics, the spectral yield of the K_W-K_W-exciton decreases rapidly. The population of the hΣ-exciton starts to build up on similar time-scales compared to the monolayer, reflecting a similar exciton-phonon scattering mechanism of the hΣ-exciton formation [8]. After having reached its maximum yield, the spectral yield for the hΣ-exciton population starts to decrease and the interlayer exciton's spectral yield increases simultaneously, which strongly hints to a second scattering channel from the hΣ-valley to the K_{Mo}-valley and hence to a sequential ILX formation process in the form of $A_W \rightarrow h\Sigma \rightarrow ILX$. A detailed description and microscopic modelling will be presented in chapter 3.

The microscopic model to describe the ILX formation, shows that, due to the hybridization, the hΣ-excitons should have lower exciton energies than the intralayer Σ-excitons in the monolayer (c.f. Fig. 2.4.6 a) and c)). In a follow-up publication to ref. [28] on the same data set by Bange *et al.* [8], the presence of the energetically lower hΣ-exciton could be directly identified and the influence of the hΣ-exciton on the exciton dynamics were elaborated [8]. The energetically lower hΣ-excitons (c.f. Fig. 2.4.3) make the scattering of the initially excited bright K_W-K_W-exciton to hΣ via exciton-phonon-scattering energetically favorable. The larger energy difference between the bright exciton and the hybrid hΣ-exciton compared to the intralayer Σ-excitons in the monolayer WSe_2 strongly suppresses the backscattering of

hΣ-exciton, which leads to a rapid depletion of the intralayer K_W-K_W-exciton occupation.

Very recently, it has been shown by Bange *et al.* that also the hole charge transfer can be tracked by the trARPES experiment [76] by first exciting the bright MoS_2 K_{Mo}-K_{Mo}-exciton. The experiment reveals an unexpected energetic upshift of the spectral yield of the exciton photoemission signal found at the K_{Mo}-valley, which is a direct consequence of the formation of the interlayer exciton by a hole transfer process. Photoluminescence measurements have shown that the WSe_2/MoS_2 structure also exhibits Γ-K_{Mo} excitons, which could not yet be identified in the trARPES experiment.

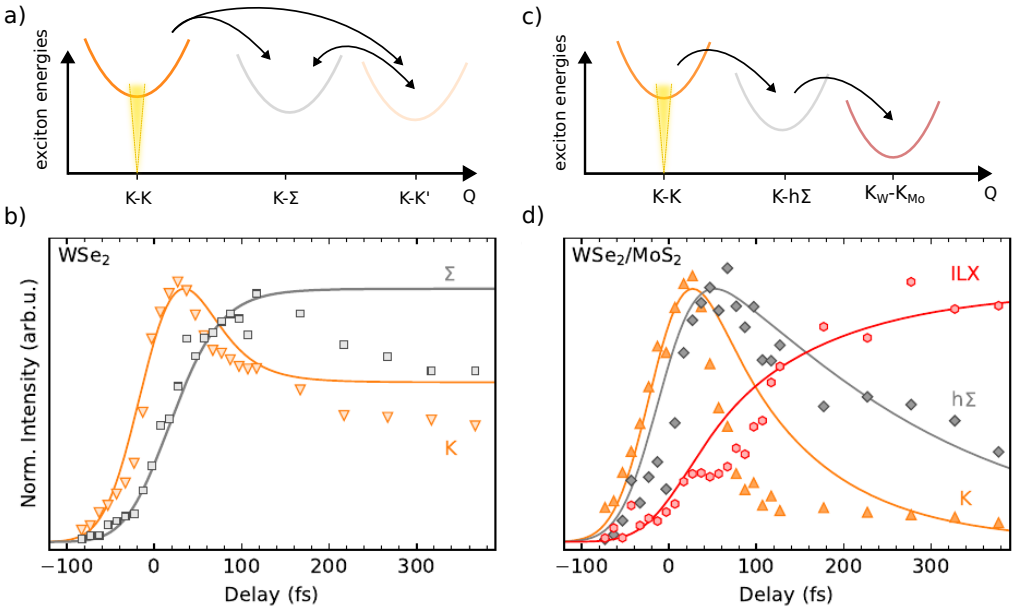

Fig. 2.4.6.: a) Schematic exciton landscape and scattering channels of monolayer WSe_2 b) Temporal evolution of the spectral yield of the electron contribution of the K-K exciton (orange triangles) and the K-Σ-exciton (gray squares) measured by the trARPES experiment. c) Schematic exciton landscape and scattering channels of a WSe_2/MoS_2 heterostructure. d) Temporal evolution of the spectral yield of the electron contribution of the K-K exciton (orange triangles), the K_W-hΣ-exciton (gray squares) and the K_W-K_{Mo} interlayer excitons (red circles). The solid lines in b) and d) are extracted from a microscopic model. Image b) and d) taken from Bange *et al.* [8]

The trARPES experiments and the microscopic model suggest that the formation of the interlayer excitons in a WSe_2/MoS_2 heterostructure is mediated by the hybridized hΣ-excitons. Consequently, the degree of hybridization of the hΣ-excitons should directly affect the charge transfer. The influence of the hybridization on the exciton lifetimes has been experimentally verified in a WSe_2 homobilayer by MIR spectroscopy [6]. In this work, the degree of hybridization was changed by increasing the twist angle of the homobilayer, and they were able to resolve systematic changes of the binding energies and lifetimes of the hΣ-excitons.

However, a hybridization dependent ILX formation remained so far elusive. In the second publication of this manuscript-based thesis [30], a spatially varying interlayer exciton formation time is observed, which could be tracked down to a spatially changing hybridization of the hΣ-excitons. A detailed description and microscopic modelling will be presented in chapter 4.

Note that the described exciton landscape of the WSe_2 monolayer and the WSe_2/MoS_2 heterostructure also includes K-K', K-Σ', K-hΣ' and K_W-K'_{Mo} excitons, which are important for the described dynamics. However, because the photoemission signal of these excitons appear at the same position in momentum-space as the K-K, K-Σ, K-hΣ and K_W-K_{Mo} excitons and have comparable exciton energies, the ARPES experiments cannot distinguish them. Consequently, the temporal evolution of the incoherent exciton populations shown in Fig. 2.4.6 b), c) and throughout this work include contributions from all these different excitons.

2.4.7. Inhomogeneities

Because of the fabrication process of TMD structures, including the growth, mechanical exfoliation/stacking and additional sample treatment prior to the experiment [91], the resulting TMD structures are exposed to different kinds of disorder [20]. The presence of disorder can result in local strain regions [92], local changes of the twist angle [93], dielectric disorder [94], charging effects [20] and many more. All of these disorder effects can affect the exciton landscape and the respective exciton dynamics of the TMD structures. The following discussion will elaborate the influence of the dielectric environment, strain and substrate effects.

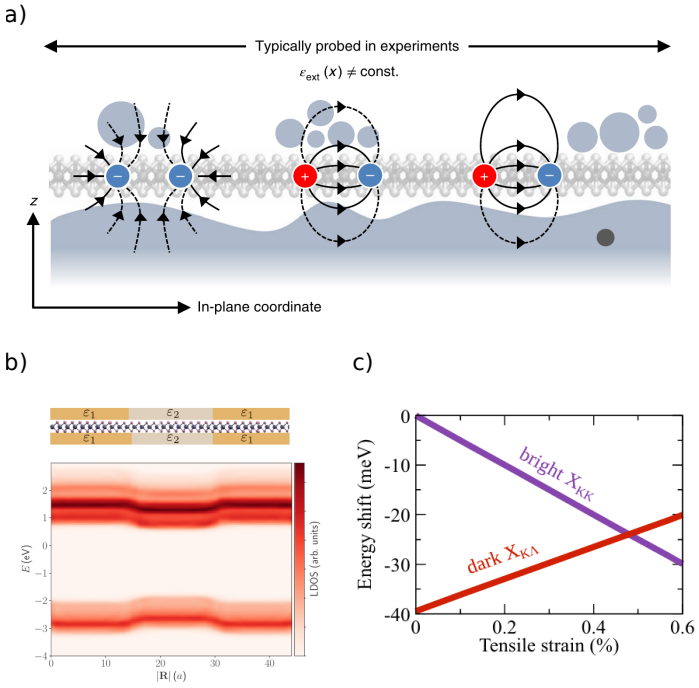

Fig. 2.4.7.: a) Adsorbates, imperfections and the surface potential directly shape the effective dielectric environment and thus the interaction strength of electron-hole pairs, b) Change of the single-particle band structure for different dielectric environments. c) Strain directly affects the energetics of bright and dark excitons and can also lead to a diffusion towards strain or away from strain regions, respectively. Image a) taken from [94], b) from [95] and c) from [75].

Influence of the dielectric environment:
The dielectric environment of 2D TMDs determines the presence of excitons with large binding energies. Consequently, the exciton landscape is strongly affected by variations of the dielectric environment. Fig. 2.4.7 a) illustrates that the dielectric environment and thus the interaction of charged particles can be affected by adsorbates and the surface potential [94].

The changed dielectric environment leads to a renormalization of the single-particle electronic band structure [95, 96] (c.f. Fig. 2.4.7 b)) and to a change in the exciton landscape, as shown by Raja *et al.* [94]

Influence of strain:
The presence of blisters (gas bubbles) between and under the layers can cause strain in the vicinity of those. The strain can strongly modify the electronic structure [97], e.g. leading to a band gap transition from direct to indirect [98], and also directly impacts the exciton landscape [97]. As shown by Rosati *et al.* [75], the bright and dark excitons of WS_2 experience opposite energetic shifts as a function of strain (c.f. Fig. 2.4.7 c)).

Influence of the substrate:
The quality of the surface strongly determines the surface potential of TMD flakes. First experiments were investigating TMD samples on top of SiO_2-substrates [79, 25, 20, 13]. The SiO_2-substrates are known to exhibit strong local potential variation, charge impurities and roughness, which can cause a variation of the local exciton energies [20]. In order to minimize such substrate effects, present experiments use hexagonal Boron Nitride (hBN) either as encapsulation of the whole flake or only as a substrate. The insulating hBN provides here a high-quality substrate with a bandgap of 6 eV and low surface roughness [20]. The strong impact of the substrate on the quality of the sample is demonstrated and discussed in Fig. A.9.2 and also in reference [99], showcasing the importance of a high-quality substrate.

2.4.8. Experimental access to excitons

Because of the multitude of exciton properties of TMD structures and the potential use for optoelectric devices, there are a strong experimental research efforts to explore the exciton landscape and the respective exciton dynamics. This section gives a brief overview of commonly used techniques for exciton-related studies.

All-optical experiments:
Intuitively, the most direct way to study the optical response of the exciton landscape is provided by all-optical experiments, such as photoluminescence- or absorbtion spectroscopy, which are able to spectrally resolve the excitations and recombinations energies of excitons [12, 64]. The seminal photoluminescence works were able to identify intra/interlayer excitons in TMD monolayer and heterostructure and identified signatures of confinement and hybridization effects inside moiré structures [14]. Time-resolved photoluminescence could verify the enhanced lifetime of interlayer excitons in twisted heterostructures [17]. The sensitivity of photoluminescence techniques, however, are mainly limited to direct transitions inside the light cone, which mostly hinders the observation of dark (e.g. momentum-indirect) excitons. However, recently it was shown that also dark excitons can decay under emission of phonons to virtual states inside the light cone, leading to distinct spectral features in the PL spectra (phonon sidebands) [22].

Time-resolved reflectivity, transient absorption and second-harmonic generation experiments are able to get access to the electron's and the hole's ultrafast charge transfer, which is measured by exciting the intralayer excitons of one layer and probing of the other layer [16, 89, 15, 88, 86]. Because of the layer sensitivity, the interlayer exciton formation can be studied even for larger twist angles [89], but they can not discriminate between different exciton species inside the layer.
Other techniques such as four-wave mixing (FWM) can be used to track coherent processes of monolayer [19] and heterostructures [100], giving access to, e.g., the dephasing times of the coherent exciton population.

Near-infrared pump–MIR probe spectroscopy:
While all of the above techniques used pump and probe pulses in the range of visible to near-infrared photon energies, the near-infrared pump–MIR probe spectroscopy monitors the temporal change of the electric field of mid-infrared pulses, by tuning the MIR wavelength to the excitonic 1s-2p transition. This technique is able to provide the optical conductivity and the dielectric function as function of pump-probe delay [77, 6]. Since the energy for the 1s-2p transition is different for different exciton states, this method is also able to track the temporal evolution of the occupation of momentum-indirect excitons. By applying the detection scheme to a heterostructure, this technique has been used successfully to investigate the formation of interlayer excitons in a WS_2/WSe_2 heterostructure and the exciton dynamics of WSe_2 homobilayers with varying twist-angles [77, 6].

Nanoscopy:
Due to the influence of disorder on the exciton landscape, spatially resolved techniques with sub-µm resolution are required to distinguish the influence of disorder from the unperturbed exciton landscape. Most optical techniques provide spot diameters in the range of a few micrometers, and thus usually integrate over many inhomogeneities. Using tip-enhanced optical spectroscopy [19, 18], the optical response can be probed with a spatial resolution of about 50 nm. A recent study has shown that even in relatively 'flat' regions, the recombination of interlayer excitons can be drastically different [18].

trARPES:
All the above-mentioned techniques provide unique spectral, spatial and temporal access to the exciton landscape. However, the exciton landscape is defined by the position and distribution of excitons in momentum space, where the mentioned experiments provide only limited access. In section 2.1 trARPES was introduced as a technique that provides energy, in-plane momentum and temporal resolution of excited carriers. Seminal trARPES measurements of excitons in TMDs have shown the unprecedented access to momentum-indirect exciton signatures in monolayer TMDs and their temporal evolution [24, 26, 25]. The access to the momentum-distribution of bright and dark excitons allows the measurement of the dispersion of the exciton photoemission signature and the extraction of the Bohr radius [27, 26, 28]. However, by now there are only a few studies applying trARPES to twisted TMD heterostructures [101, 28, 30, 76, 8]. The first publication of this cumulative thesis (3) investigates the exciton landscape and dynamical response of a 9.8° twisted WSe_2/MoS_2

heterostructure using time-resolved momentum microscopy (trMM). The trMM experiment provides here a distinct momentum fingerprint of the interlayer exciton, is able to uncover the dynamics of the interlayer exciton formation and, allows the reconstruction of the wavefunction distribution of the electronic part of the exciton [28].

Concerning the spatial resolution, the trMM experiment averages over probing areas of about $> 100\ \mu m^2$ [28, 25, 24] and thus integrate over multiple inhomogeneities. In order to resolve the influence of disorder to momentum-indirect excitons, the second article of this manuscript based thesis makes use of the dark-field real-space imaging capabilities of the trMM setup, which allows the projection of selected momentum regions-of-interest to real-space coordinates. In this way, the formation of dark momentum-indirect interlayer excitons can be tracked on the nanometer-to-micrometer spatial scale.

2.5. Photoemission signatures of excitons

In this work, the method of choice is time-resolved photoemission spectroscopy because of its ability to map the energy and momentum distribution of the out-of-equilibrium band structure. As described in the previous section, trARPES experiments are able to provide unique access to exciton landscape and dynamics in TMD structures. To extract such information from the trARPES data, the photoemission signature of the excitons has to be examined. Therefore, this section provides information about the energetic positions, dispersion and photoemission intensity of the exciton photoemission signal.

2.5.1. Exciton energies in ARPES

In the seminal ARPES experiments on excitons [24, 26, 25, 27], it has been shown that ARPES experiments are able to provide direct access to the exciton energy E_{exc} (c.f. equation 2.5). The mentioned ARPES articles assume here a near zero kinematic center-of-mass momentum and the lowest exciton energies. During the photoemission process, the exciton is ionized, resulting in the breakdown of the correlated electron-hole pair. In order to detect the electron of the ionized exciton, it has to overcome the work function of the material, while the hole is left behind in the valence band. Following the approach by Weinelt *et al.* [102, 76, 26], the total energy before photoemission is given by $E_{\text{init}} = E_0 + E_{\text{exc}} + h\nu$, where E_0 is the ground state energy and $h\nu$ the probe photon energy. After the break-up of the exciton and subsequent photoemission of the electron, the total energy is $E_{\text{after}} = E_0 - E_{\text{hole}} + E_{\text{kin}} + \phi$, where E_{hole} is the remaining hole energy in the valence band $E_{\text{hole}} = -E_{\text{VBM}}$ and E_{kin} the kinetic energy of the photoemitted electron that has to overcome the work function ϕ. Considering energy conservation yields

$$E_{\text{kin}} = E_{\text{hole}} + E_{\text{exc}} + h\nu - \phi = -\frac{\hbar^2 k^2}{2m_h} + E_{\text{exc}} + h\nu - \phi. \tag{2.7}$$

From the equation, it is evident that the electronic contribution of the exciton is observed one exciton energy above the energetic position of the respective hole, e.g., the valence band energy E_{VBM}. In other words, the hole sets the reference energy for the exciton signature observed in ARPES experiments (c.f. Fig. 2.5.1). With that, ARPES is able to directly measure (1) exciton energies E_{exc} as the difference between the photoemitted electron and the photoemission energy of the remaining hole and (2) the absolute energies of both constituents. As a consequence, in contrast to photoluminescence experiments, ARPES is capable to distinguish between excitons with the same exciton energy where the hole is located at different energies. Two very recent experiments, performed with the present experiment setup [103, 76], make direct use of that property.

2.5.2. Dispersion of exciton states in ARPES

From equation 2.5 follows that the exciton exhibits a positive dispersion as function of the kinematic center-of-mass momentum. However, from equation 2.7 it follows that during the break-up of the exciton, the energy of the hole must be included, which mirrors the dispersion of the valence band energy. Assuming zero center of mass momentum (Q=0), for every k-point around the negatively curved valence band the exciton energy has to be added, which ends up in a negative dispersion of the photoemitted exciton electron signal (cf. fig. 2.5.1 a)). For a broader distribution of the center-of-mass momentum (cf. Fig. 2.5.1 b) inset), the VB-like dispersion has to be added for every center-of-mass momentum, which ends up in a more CB-like dispersion of the exciton photoemission signature. Recently, the VB-like dispersion (Q=0) of the exciton photoemission signal could be verified [26]. In the data measured in this PhD thesis (see chapter 2.7), such a dispersion was not observed, which could be attributed to the energy-resolution, room-temperature conditions and spectrally broad pump excitation of the experiment, leading to broader center-of-mass momentum distributions.

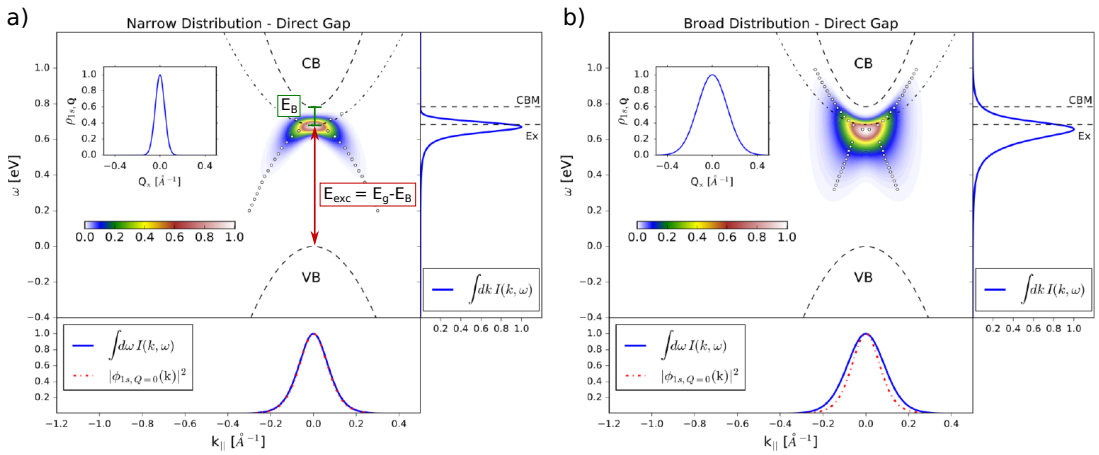

Fig. 2.5.1.: a) Theoretical calculations of ARPES spectra showing a dispersive exciton features as a signal below the conduction band and one exciton energy above the hole position in the valence band (VB and CB are indicated by dashed lines). In a) the center of mass-momentum-distribution is very narrow (inset), leading to a VB-like dispersion of the exciton signature. Additionally, the energy-integrated intensity profile (lower panel blue line) is identical to the modulus squared of the exciton wave function (lower panel red dashed line). c) In the case of a broader center-of-mass momentum distribution (inset), the dispersion of the exciton photoemission signal becomes a mixture of VB-like and CB-like dispersion and the energy-integrated intensity profile (lower panel blue line) is slightly larger than the modulus squared of the exciton wave function (lower panel red dashed line). Image obtained from [71].

2.5.3. Hole contribution to the exciton ARPES signature

So far, the electronic contribution to the excitons was discussed as the main experimental observable in the ARPES experiment. Recently, it was shown that also photoemission signatures of the hole can be observed as a reduced photoemission yield at the valence band maximum [101]. From this observation, the momentum distribution of the electron and the hole can be extracted individually, giving access to the center-of-mass momentum and to the exact reference energy of the hole. Besides that and the observation of the VB-like dispersion of the exciton signature (Fig. 2.5.1 a)), there can also be a more indirect influence of the hole, affecting the exciton photoemission signal. The first publication of this thesis in chapter 3 will show that also the lattice periodicity of the respective electron and hole has to be taken into account, leading to distinct fingerprints of exciton signatures. Moreover, two very recent articles, measured with the given experiment, were able to show that a coherent sum of electron-hole contributions has to be considered [103] and that the scattering of holes directly influences the exciton state and also the energetic position of excitons in the photoemission experiment (c.f. equation 2.5) [76].

2.5.4. Exciton wave function in real- and momentum-space

As shown in section 2.1, the ARPES experiment measures the photoemission intensities I(**k**, E) as a function of energy and momentum coordinates. In photoemission orbital tomography (POT) [104] it was demonstrated that the real-space wave function can be reconstructed through a Fourier transform of the photoemission intensities I(**k**, E) by assuming a plane wave for the final state [104]. This raises the question if, on the basis of POT, also the electronic contribution to the exciton wave function can be reconstructed from I(**k**, E). The starting point for the calculation of the photoemission intensity is given by the exciton wavefunction for zero center-of-mass momentum [71, 26, 105]

$$|\psi\rangle = \sum_{vc\mathbf{k}} A^{\dagger}_{vc\mathbf{k}} c^{\dagger}_{c\mathbf{k}} c_{v\mathbf{k}} |0\rangle\,, \tag{2.8}$$

where $A^{\dagger}_{vc\mathbf{k}}$ describes the envelope wavefunction of the exciton in reciprocal space and $c_{i\mathbf{k}}$ are the annihilation and creation operators acting on the ground state $|0\rangle$, creating the exciton. In the Wannier limit, the exciton wave function is mostly governed by the envelope function $A^{\dagger}_{vc\mathbf{k}}$. Now, the exciton photoemission intensity can be calculated by evaluating eq. (2.4). Assuming a plane wave approximation for the final state [27] yields the photoemission intensity as

$$I(\mathbf{k}) = |\mathbf{A}\cdot\mathbf{k}|^2 |\psi(\mathbf{k})|^2 \delta(E_B + E_{\mathrm{kin}} + \phi - \hbar\omega), \tag{2.9}$$

where $|\mathbf{A}\cdot\mathbf{k}|^2$ describes the polarization factor and the δ-term ensures the conservation of energy. Since the exciton wave function is governed by the envelope function, the photoemission intensity is proportional to $\mathrm{I}(\mathbf{k}) \propto |A^{\dagger}_{vc\mathbf{k}}|^2$. Consequently, the momentum-resolved photoemission intensity distribution of the exciton signature in ARPES experiment provides directly access to the modulus squared of the exciton envelope wave function. By assuming a constant phase, the real-space electronic contribution of the exciton wave function modu-

lus squared can be directly calculated by performing a Fourier transform of $I(\mathbf{k})$ and from that, quantities such as the Bohr-radius can be directly accessed. This relation is only exact if the center-of-mass momentum is near zero (c.f. Fig: 2.5.1) and if the assumed phase for the exciton wavefunction is a sufficient assumption. For finite center-of-mass momenta, the extension of the wavefunction in momentum-space can be slightly larger (cf. Fig. 2.5.1 b) lower panel). The assumption of the constant phase for the exciton wavefunction could lead to deviations and provides also only a lower limit for the Bohr radius [27].

2.6. Experimental setup

The starting point of this thesis was the implementation of the time-resolved momentum microscopy (trMM) setup that combines a table-top high-repetition-rate high harmonic generation beam line with a state-of-the-art time-of-flight momentum microscope [35]. The whole setup was benchmarked in the publication [29] and in the PhD-thesis of Marius Keunecke [55]. As stated in [55], Marius Keunecke had significant contributions to the build-up of the trMM setup. The HHG beam line was first planned, build-up and characterized by Christina Möller [29], Marie Gutberlet [106] and Amelie Schulte [107]. Significant modifications of the setup compared to [29] and [55] involves the installation of a new 300 W AFS fiber-based laser system, the implementation of an optical parametric amplifier (OPA), improvements of the HHG beam diameter for momentum microscopy of µm-sized samples and dark-field experiments, and the implementation of a spin-crystal for spin-resolved measurements. These modifications were implemented in collaboration with Wiebke Bennecke [108], Jan Philipp Bange and Marco Merboldt. Further help concerning the setup and implementation of analysis software were provided by bachelor and master students Hendrik Nolte [109], Paul Werner [70] and Michael Stellbrink [110].

This section starts with an introduction to the specific requirements that the experiment has to fulfil in order to measure the exciton landscape and dynamics, followed by a brief description of the setup. A detailed description of technical details and the alignment procedures of the µARPES and dark-field momentum microscopy experiments are provided in the Appendix A.

2.6.1. Experimental requirements

In order to measure the energy landscape and dynamics of excitons in a photoemission experiment with momentum, energy, temporal, and spatial resolution, the experiment has to fulfil certain key requirements:

1. **Requirements to the optical setup**
    a) Femtosecond EUV probe beam line (> 11 eV) to access the whole Brillouin zone of the TMDs (> 1.25 1/Å)
    b) Spectrally tunable femtosecond pump beam line for selective optical excitation
2. **Requirements to the experimental probe**
    a) Energy and in-plane momentum resolution
    b) Sensitivity for few µm-sized samples
    c) Nanometer spatial resolution

2.6.2. The trMM setup

The experimental setup that has these key-requirements is shown in Fig. 2.6.1. It includes a high-harmonic generation source and a monochromatization scheme, the variable OPA pump beam line and the momentum microscope. The setup is benchmarked and detailed in ref. [29] and [55]. A very brief description of the different components and how the setup can be used to gain access to photoemission signatures of excitons with momentum, energy, temporal, and spatial resolution is provided in the following. A more detailed description of the experimental setup and additional information on alignment procedures can be found in the Appendix A.

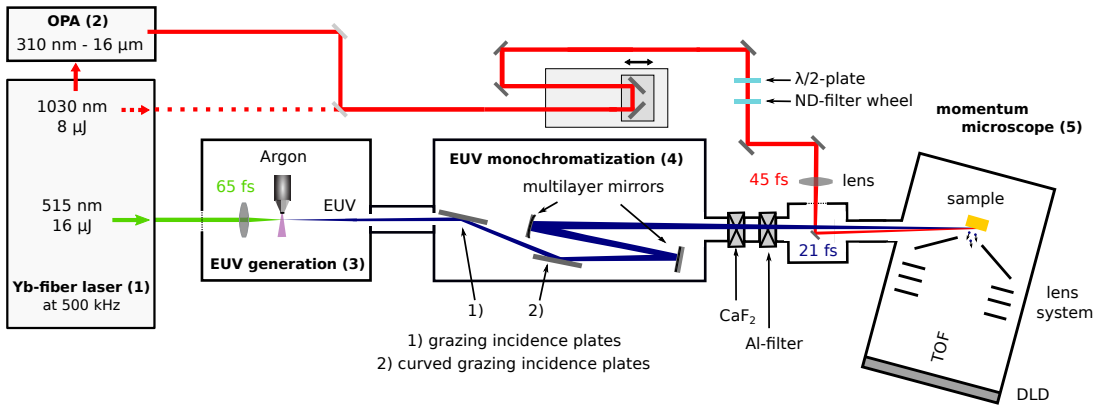

Fig. 2.6.1.: Scheme of the experimental setup. The 500 kHz 300 W Yb-fiber laser system (1) provides the laser power for the tunable OPA beam line (2) and the high harmonic generation (3). Before entering the momentum microscope (5), the HHG light is monochromatized (4). Picture obtained from [29] with slight adaption to the current setup.

The 300-W Yb fiber-based laser system:
The optical setup is based on a 300-W Yb-based fiber laser system from Active Fiber System (AFS) that operates at a repetition rate of 500 kHz with a pulse lengths 250 fs and a central wavelength of 1030 nm. An additional nonlinear compression provides pulse length of 30-40 fs. The laser system is used to drive the high harmonic generation and optical parametric amplifier. More details can be found in A.1.

EUV probe beam line
The light source has to provide sufficiently high photon energies to get access to the distinct photoemission signatures of exciton states that appear at large in-plane momenta, e.g., at the K/K'-valleys of the TMD Brillouin zone. In the case of WSe_2, the K-valleys are at 1.25 1/Å which requires a minimal photon energy of 11 eV (see section 2.1.1, ϕ_{WSe_2} =4.35 eV [36]). Such large photon energies can be generated either by large facility FEL beam lines or by table-top high harmonic generation (HHG) light sources. The latter has the advantage of availability (table-top experiment) and tunability of the repetition-rate, while providing also excellent temporal resolution [111]. In this work, the high harmonics are generated by

focussing the second-harmonic of the laser output into an Argon gas jet. The monochromatization is performed by using multilayer mirrors. With that, the HHG beam line provides 26.5 eV (p-polarized) photon energies with a pulse length of 21 $\pm$ 5 fs. Further details can be found in A.2, A.8 and [29, 55].

Spectrally tunable pump beam line
In order to resonantly excite the exciton signatures of the specific sample, the pump beamline has to provide spectrally tunable pump photon energies. For that, a part of the laser light is used to drive a commercially available high-power optical parametric amplifier (OPA, Orpheus-F/HP from Light Conversion, wavelength-range 310 nm to 16 µm). In most experiments, performed in this PhD-thesis, the OPA photon energy was tuned to 1.7 eV in order to resonantly excite the bright $K_W - K_W$ of WSe_2. A prism-based compression of the output beam provides a pulse length of about 50 $\pm$ 5 fs. Further information is provided in A.1 and A.8.

Time-resolved Momentum Microscopy:
As described in section 2.5, the trARPES experiment provides an excellent approach to explore exciton signatures with energy and momentum resolution. However, as it will be demonstrated in both publications of this thesis (Ch. 6), the photoemission yield of excitons can be distributed over the whole Brillouin zone. Conventional trARPES experiments (using hemispherical analyzers) are able to measure certain directions in momentum-space, and in order to map the whole Brillouin zone, the sample has to be rotated systematically. In this work, photoemission data is acquired by a time-of-flight momentum microscope [35] (ToF Momentum Microscope, Surface Concept), which allows a simultaneous acquisition of the two in-plane momenta (k_x, k_y) and the kinetic energy E_{kin} of photoelectrons within the full photoemission horizon. The combination with an EUV beam line and the spectrally tunable OPA pump beam line gives access to the femtosecond photoemission signal across the whole Brillouin zone, which enables the detection of all contributing exciton signatures. Further information regarding the working principle of the time-resolved momentum microscope can be found in section A.3 and A.7.

Sensitivity for few µm-sized exfoliated TMD flakes:
The fabrication of TMD flakes by exfoliation usually provides monolayer/heterobilayer TMD flakes on the order of a few micrometers. Therefore, the experimental probe must be sensitive to µm-sized regions-of-interest. Here, the momentum microscope provides another great key-advantage. The microscope electrostatic lens system allows the placement of apertures into the image-plane and the back-focal plane. Since the image-plane corresponds to the real-space distribution of photoelectrons, the aperture can be used to map the in-plane momentum and energy-resolved photoelectrons for specific regions of the sample. This real-space selective access to the momentum- and energy-resolved photoemission yield of the exciton landscape and exciton dynamics of µm-sized TMD flakes provides the key-requirement for the results of the first publication of this manuscript-based thesis (see chapter 3). Additional information on the alignment procedure for momentum microscopy of µm-sized samples can be found in section A.4.

Nanometer to micrometer real-space resolution:
As described in section 2.3, the presence of disorder can directly affect the exciton landscape. Therefore, it is advantageous to have an experimental probe which is sensitive to the exciton landscape and dynamics on the nanometer scale. Similar to the selected region in the image-plane, the microscope also allows to map the real-space and energy distribution of the photoemission yield for a specific momentum region-of-interest. This detection scheme enables a new experimental technique of dark-field momentum microscopy [112]. This new experimental approach allows to measure the spatio-temporal evolution of bright and dark exciton photoemission signatures on the femtosecond timescale and on the nanometer-to-micrometer spatial scale. The spatio-temporal access to the exciton landscape is demonstrated in the second publication of this manuscript-based thesis (see chapter 4). Additional information on the working principle, alignment of the lens system and data handling can be found in section A.5 and appendix B.

2.7. Original manuscripts

The next two chapters include two original manuscripts, which form the core of this manuscript-based thesis.

The first article "Formation of interlayer excitons in space and time" explores the distinct momentum fingerprint, the ultrafast formation dynamics and the reconstruction of the electronic contribution of the real-space wave function of the interlayer exciton in a twisted 9.8 $\pm$ 0.8 ° WSe_2/MoS_2 heterostructure. The measurements presented in this article make use of the momentum-resolved mode of the momentum-microscope A.4, providing direct access to the time-resolved exciton photoemission signal of µm-sized TMD flakes.

The second article describes a new approach to explore the nanoscale variation of the exciton landscape and the respective exciton dynamics on the 500 nm scale. The presented study, "Ultrafast nano-imaging of dark excitons", makes use of the dark-field real-space imaging capabilities of the momentum microscope, where a selection of a certain region-of-interest in momentum space allows the projection of the selected momentum range to real-space coordinates. In that way, the experiment is able to investigate the sub-µm spatio-spectral and spatio-temporal variation of the energy and formation of dark interlayer excitons.

At the beginning of each article, additional information about the author contributions and the submission state will be provided.

CHAPTER 3

Formation of moiré interlayer excitons in space and time

The following article "Formation of moiré interlayer excitons in space and time" is published in Nature[28]. The article version presented in this work is the accepted and peer-reviewed manuscript and differs only by editorial changes from the online available published version (DOI: 10.1038/s41586-022-04977-7.).

Formation of moiré interlayer excitons in space and time

David Schmitt[1], Jan Philipp Bange[1], Wiebke Bennecke[1], AbdulAziz AlMutairi[2], Giuseppe Meneghini[3], Kenji Watanabe[4], Takashi Taniguchi[4], Daniel Steil[1], D. Russell Luke[5], R. Thomas Weitz[1,7], Sabine Steil[1], G. S. Matthijs Jansen[1], Samuel Brem[3], Ermin Malic[3,6], Stephan Hofmann[2], Marcel Reutzel[1] and Stefan Mathias[1,7]

Author contributions

D.St., R.T.W., S.S., G.S.M.J., S.H., M.R. and S.M. conceived the research. D.Sch., J.P.B. and W.B. carried out the time-resolved momentum microscopy experiments and analyzed the data. W.B., D.R.L., and G.S.M.J. carried out the real-space reconstruction of the momentum fingerprints. A.A. fabricated the samples. G.M., S.B., and E.M. developed the microscopic model and analyzed the results. All authors discussed the results. M.R. and S.M. were responsible for the overall project direction and wrote the manuscript with contributions from all co-authors. K.W. and T.T. synthesized the hBN crystals.

[1] I. Physikalisches Institut, Georg-August-Universität Göttingen, Friedrich-Hund-Platz 1, 37077 Göttingen, Germany
[2] Department of Engineering, University of Cambridge, Cambridge CB3 0FA, U.K.
[3] Fachbereich Physik, Philipps-Universität, 35032 Marburg, Germany
[4] International Center for Materials Nanoarchitectonics, National Institute for Materials Science, 1-1 Namiki, Tsukuba 305-0044, Japan
[5] Institute for Numerical and Applied Mathematics, Georg-August-Universität Göttingen, Lotzestrasse 16-18, 37083 Göttingen, Germany
[6] Department of Physics, Chalmers University of Technology, Gothenburg, Sweden
[7] International Center for Advanced Studies of Energy Conversion (ICASEC), University of Göttingen, Göttingen, Germany

Abstract

Moiré superlattices in atomically thin van-der-Waals heterostructures hold great promise for an extended control of electronic and valleytronic lifetimes [15, 13, 113, 114, 77, 115, 116], the confinement of excitons in artificial moiré lattices [117, 118, 9, 14, 119, 101], and the formation of novel exotic quantum phases [120, 121, 122, 123, 124]. Such moiré-induced emergent phenomena are particularly strong for interlayer excitons, where the hole and the electron are localized in different layers of the heterostructure [125, 87]. In order to exploit the full potential of correlated moiré and exciton physics, a thorough understanding of the ultrafast interlayer exciton formation process and the real-space wavefunction confinement is indispensable. Here we show that femtosecond photoemission momentum microscopy provides quantitative access to these key properties of the moiré interlayer excitons: First, we elucidate that interlayer excitons are dominantly formed via femtosecond exciton-phonon scattering and subsequent interlayer tunneling at the interlayer-hybridized Σ valleys. Second, we show that interlayer excitons exhibit a momentum fingerprint that is a direct hallmark of the superlattice moiré modification. Third, we reconstruct the wavefunction distribution of the electronic part of the exciton and compare the size with the real-space moiré superlattice. Our work provides the first direct access to interlayer exciton formation dynamics in space and time and reveals new opportunities to study correlated moiré and exciton physics for the future realization of exotic quantum phases of matter.

The advent of two-dimensional van-der-Waals materials [126] has led to remarkable new strategies to manipulate correlated material properties. In transition metal dichalcogenides (TMDs), exceptional light-matter coupling and weak Coulomb screening of photoexcited electron-hole pairs allow to realize novel spin, valley, and excitonic properties of matter [3, 65]. Even more intriguing material properties can be accomplished in TMDs by stacking several monolayers into heterostructures [4, 125, 87]: In type II band-aligned stacks, novel excitonic states can be created, where the electron and the hole contribution to the exciton are separated between the van-der-Waals-coupled TMDs [101] (Fig. 3.0.1e). A key question that to date remains unanswered is how these interlayer excitons (ILX) are formed. Furthermore, the lattice mismatch and the twist angle between the TMDs induce a moiré superlattice, which makes it necessary to understand how precisely the interaction of the exciton and the moiré potential determines the material properties (Fig. 3.0.1d). Most intriguingly, it has been shown by optical [9, 14, 119] and momentum microscopy [101] experiments that ILXs can be confined within the moiré potential minima. However, a significant open challenge is the experimental identification of universal hallmarks that indicate signatures of the moiré superlattice imprinted onto the ILX.

Experimental quantitative insight into the ILX formation process and the influence of moiré modulation onto the ILX is so far strongly limited. All-optical spectroscopy techniques are only sensitive to transitions within the light cone [72] and thus lack the momentum information that is necessary to gain access to the time-dependent energy-momentum-fingerprints of the probed quasiparticles [24, 25, 27]. Using multidimensional time- and angle-resolved photoelectron spectroscopy (trARPES) on a tungsten diselenide / molybdenum disulfide (WSe_2/MoS_2) heterostructure, we find, for the first time in experiment, that ILX are dominantly formed

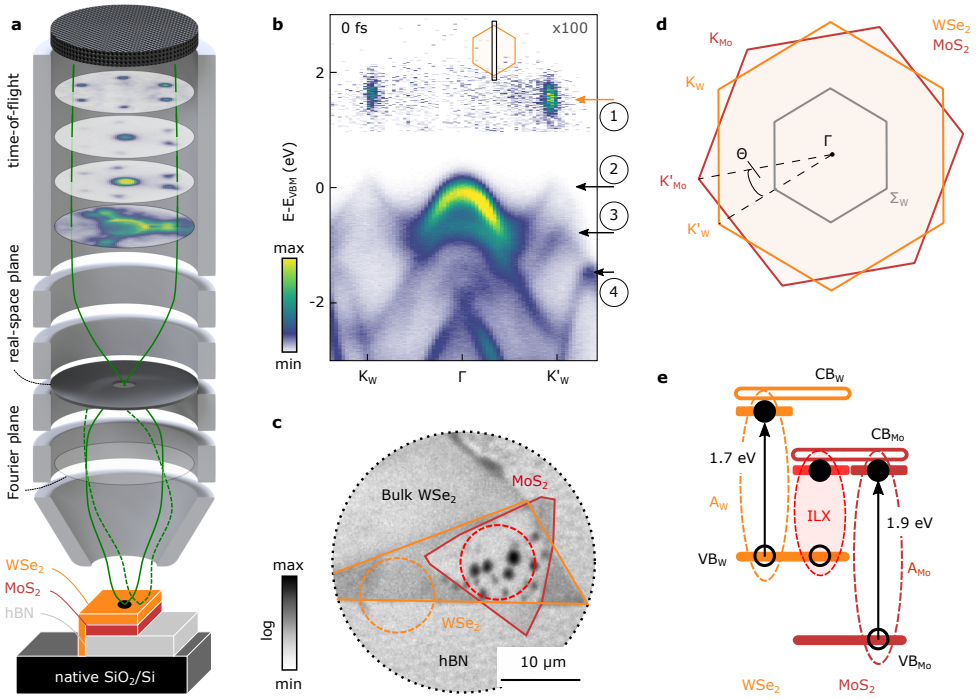

Fig. 3.0.1.: **Inter- and intralayer excitons in WSe_2/MoS_2 probed by femtosecond momentum microscopy. a** Illustration of the experimental setup and the WSe_2/MoS_2/hBN sample. **b** The valence bands of WSe_2 (2), MoS_2 (3), and hBN (4) are labelled in the energy-momentum cut. At 0 fs, bright A_W-excitons (1) are detected at the K_W and K'$_W$ valleys of WSe_2. **c** The heterostructure can be identified in the real-space mode of the microscope. The WSe_2/MoS_2 and WSe_2 regions-of-interest are indicated by red and orange circles, respectively (10μm diameter, see Methods). **d** The hexagonal Brillouin zones of WSe_2 (orange) and MoS_2 (brown) are misaligned by a twist angle Θ. **e** Bright A_W- and A_{Mo}-excitons of WSe_2 (orange) and MoS_2 (brown) can be resonantly excited with 1.7 eV and 1.9 eV pump photons, respectively (VB_W, VB_{Mo}: valence band maxima; CB_W, CB_{Mo}: conduction band minima). The hole and the electron contribution of the ILX reside in the WSe_2 and MoS_2 layer, respectively.

through exciton-phonon scattering via intermediate dark excitonic states at the Σ valleys of the hexagonal Brillouin zones. These results are fully supported by a microscopic model including exciton-light and exciton-phonon interaction on microscopic footing. Even more, we discover a complex momentum fingerprint of the ILX, and we show that this fingerprint is a direct hallmark signature of the moiré superlattice modification. From this data, we then reconstruct the real space wavefunction probability density of the electronic part of the exciton's wavefunction that we compare to the moiré superlattice size.

The electronic band structure of WSe_2/MoS_2

We focus our study on the model system WSe_2/MoS_2 with a twist angle of $9.8\pm0.8^\circ$ (Extended Figs. 3.0.5, 3.0.8) [127] and use our customized trARPES system that combines a

momentum microscope [35] with a high-repetition-rate high-harmonic generation beamline (Fig. 3.0.1a and Methods) [29, 128]. The 100 μm^2 heterobilayer region can be identified in the real-space distribution of the measured photoelectron yield (Fig. 3.0.1c and Extended Fig. 3.0.5e,f). By placing an aperture into the real-space image plane of the microscope (red circle in Fig. 3.0.1c), we can selectively probe the occupied band structure of WSe_2/MoS_2. The sample quality is evidenced by the sharp spectral features of the occupied electronic structure and the signature of interlayer hybridization of the valence bands of WSe_2 and MoS_2 at the Γ valley [129] (Fig. 3.0.1b, energy resolution $\approx$200 meV, see Extended Figs. 3.0.6 and 3.0.7).

Femtosecond ILX formation dynamics

We follow the build-up process of the ILX by resonantly exciting the optically bright A_W-exciton of WSe_2 with 1.7 eV, 50$\pm$5 fs pulses and study the subsequent ILX formation via photoemission with 26.5 eV, 21$\pm$5 fs extreme ultraviolet probe (XUV) pulses (see Extended Fig. 3.0.9 for spectral assignment of the valence/conduction bands and the WSe_2 and MoS_2 A-excitons). Figure 3.0.2a shows highest spectral weight for the electronic part of the bright A_W-exciton around 0 fs delay and 1.7 eV above the valence band maximum (orange dashed line; exciton density: $(5.4 \pm 1.0) \times 10^{12}$ cm^{-2}, cf. Extended Fig. 3.0.12b) [24, 26, 27, 25]. On the few hundred femtosecond timescale, we observe the formation of a second peak at lower photoemission energy (red dashed line). We identify this peak as the photoemitted electronic contribution of the ILX: The long-lived photoemission signature is detected below the A_W-exciton resonance at about 1.1 eV above the valence band maximum of WSe_2, in agreement with static photoluminescence experiments on a WSe_2/MoS_2 heterobilayer [130]. For the unambiguous attribution of the photoemission yield to an interlayer effect, we repeated the same analysis with data obtained from monolayer WSe_2 (Fig. 3.0.2b, dashed orange circle in Fig. 3.0.1c). Here, no spectral weight is observed in the ILX's energetic region, which clearly shows that the spectral weight in the heterobilayer measurement results from the charge transfer of the electron contribution of the exciton into the MoS_2 layer. We note that the identification of the ILX is in agreement with a recent trARPES study on 2° twisted WSe_2/MoS_2 [101]. Interestingly, in addition to the electron contribution to the ILX, Ref. [101] also identified the hole contribution to the ILX in energy-momentum resolved spectra. Such a signature is not found in our analysis (Fig. 3.0.1b), which is most likely related to the different twist angles and related exciton confinement effects.

The exact mechanism of the ILX formation and the according ultrafast charge separation is still a major open question [87]. It has been proposed that the ILX can be formed via interlayer tunneling of its electron contribution at the K valleys [115, 77], or, alternatively, via the intermediate formation of dark intralayer excitons, where the electron contribution is first scattered to the Σ valley and, subsequently, transferred to the neighbouring layer [114, 79, 131]. In this context, the strength of the trARPES experiment is that the femtosecond evolution of optically dark Σ_W-excitons can be explicitly monitored [25, 27, 24]. In Fig. 3.0.2c, we therefore investigate the delay-dependent transfer of spectral weight between the electronic parts of the bright WSe_2 A_W-exciton, the dark WSe_2 Σ_W-exciton, and the ILX (data

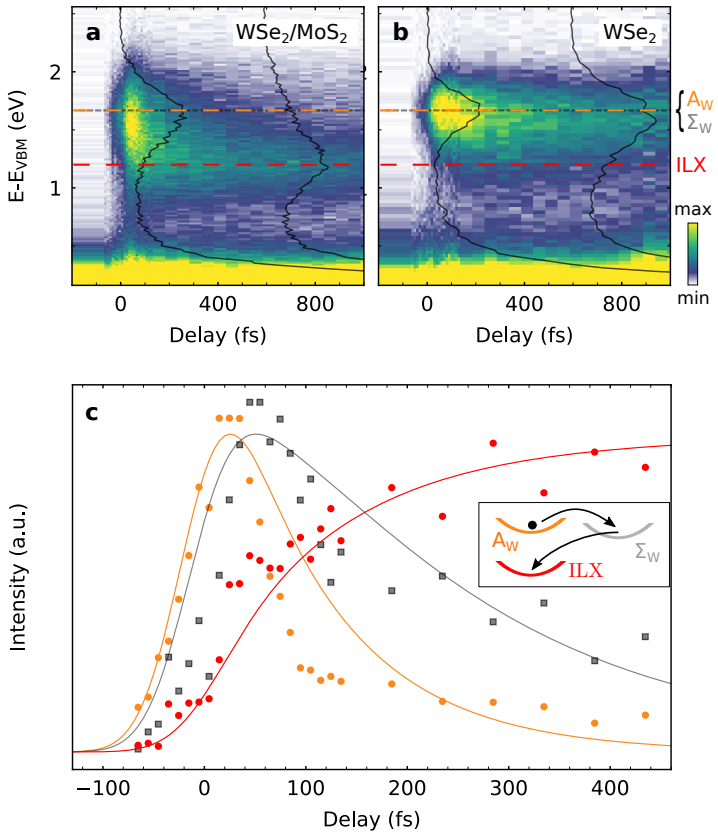

Fig. 3.0.2.: **Ultrafast formation dynamics of ILXs. a, b** Delay-dependent evolution of the momentum-integrated energy distribution curves (EDCs) for **a** WSe_2/MoS_2 and **b** WSe_2. In the monolayer, the signal decays on the picosecond timescale without a significant change in binding energy (dashed orange and grey lines). In the heterobilayer, the ILX formation is evident by the shift of spectral weight to smaller binding energies on the sub-100-fs timescale (dashed red line). The black line profiles are exemplary EDCs taken at -5 fs and 585 fs. **c** The ILX formation is extracted via the delay-dependent photoemission yield of the ILX (red), the bright A_W- (orange), and the dark Σ_W-excitons (grey, details on data analysis in Extended Figs. 3.0.11 and 3.0.12). Data points are experimental data and solid lines are calculated within a fully microscopic model. The inset shows the dominant charge-transfer channel. The EDCs in **a, b** are corrected for space-charge/photovoltage-induced rigid band shifts of maximally 70 meV (Extended Fig.3.0.12a).

handling in Extended Figs. 3.0.11 and 3.0.12; long-term picosecond dynamics in Extended Fig. 3.0.13). Initially, during the duration of the pump pulse, we find that bright WSe_2 A_W-excitons are efficiently excited (orange data points). Subsequently, the weight of their photoemission signature decreases in intensity, whereas, concomitant, spectral yield is detected for the WSe_2 Σ_W-exciton (grey) and the ILX (red). We particularly find that for the time evolution after the optical excitation and the initial build-up, the decrease of spectral weight of the electronic contribution of the Σ_W-exciton is synchronous to the increase of spectral

weight of the ILX, strongly hinting to an ILX formation process via intermediate scattering through the Σ_W valley. Here, a quantitative analysis yields delayed onsets with respect to the A_W-exciton signal of 33±6 fs for the Σ_W-exciton formation and 54±7 fs for the ILX (see Extended Fig. 3.0.13a). In order to corroborate the proposition of interlayer charge transfer through the Σ_W valley, we compare the trARPES data with predictions stemming from a fully microscopic model. We combine the density matrix formalism [132, 115] with material-specific parameters from first principle calculations in order to simulate the formation dynamics of interlayer excitons after the optical excitation of intralayer excitons. In the model, we include the full exciton landscape of bright and dark intralayer, interlayer, and hybrid excitons and all phonon-assisted transition channels between these states. We find that the most efficient exciton relaxation pathway is given by the cascade of optically-excited exciton states $A_W \rightarrow \Sigma_W \rightarrow$ ILX (inset in Fig. 3.0.2c, cf. supplemental information). The direct comparison of experiment (symbols) and theory (lines) in Fig. 3.0.2c confirms an excellent agreement. This shows, both from an experimental as well as a theoretical point of view, that phonon-assisted scattering via dark layer-mixed states is indeed the dominant pathway for the formation of ILX in the 9.8±0.8° twisted WSe_2/MoS_2 heterostructure.

The ILX moiré superlattice hallmark

While trARPES with XUV pulses is an ideal approach to study the ILX formation process, the combination with multidimensional momentum microscopy allows the identification of momentum-space signatures that are caused by the real-space moiré superlattice. In this manner, Fig. 3.0.3a, b, and c show the momentum structure of the A_W-exciton, the Σ_W-exciton, and the ILX, respectively (additional data in Extended Fig.3.0.10). While the momentum fingerprints of the A_W-exciton and the Σ_W-exciton appear as expected [24, 25], the ILX momentum structure is clearly more complex. Without consideration of the moiré superlattice, for the ILX, one would expect to detect photoemission yield at the in-plane momentum of the electron contribution to the quasiparticle, i.e., at the K_{Mo} (K'_{Mo}) valleys of MoS_2 (corners of the dotted brown hexagon in Fig. 3.0.3c). However, the measured momentum fingerprint shows a strikingly richer structure: We observe a complex momentum structure that is dominated by three peaks that are centered around the K_W (K'_W) valleys (orange hexagon in Fig. 3.0.3c). Apparently, the ILX momentum fingerprint exhibits additional features that are not observed for any other spectral feature in our data: so far, all other occupied bands and excitonic states were unambiguously assignable to the periodicity of either the WSe_2 top or the MoS_2 bottom layer.

The most interesting question now is, if the observed ILX momentum structure may be identified as a hallmark of the moiré superlattice that is created by the 9.8±0.8° twisted Brillouin zones of WSe_2 and MoS_2. To answer this question, we construct the momentum-space equivalent of the real-space moiré periodicity, which is the mini Brillouin zone (mBZ) that is shown ontop of the momentum-resolved photoemission data of the ILX in Fig. 3.0.3c (red hexagon). Within the mBZ, we can now unambiguously identify that the three-peak structure is indeed a fingerprint of the moiré superlattice, as the spectral features clearly coincide with the high symmetry κ-valleys of the mBZ.

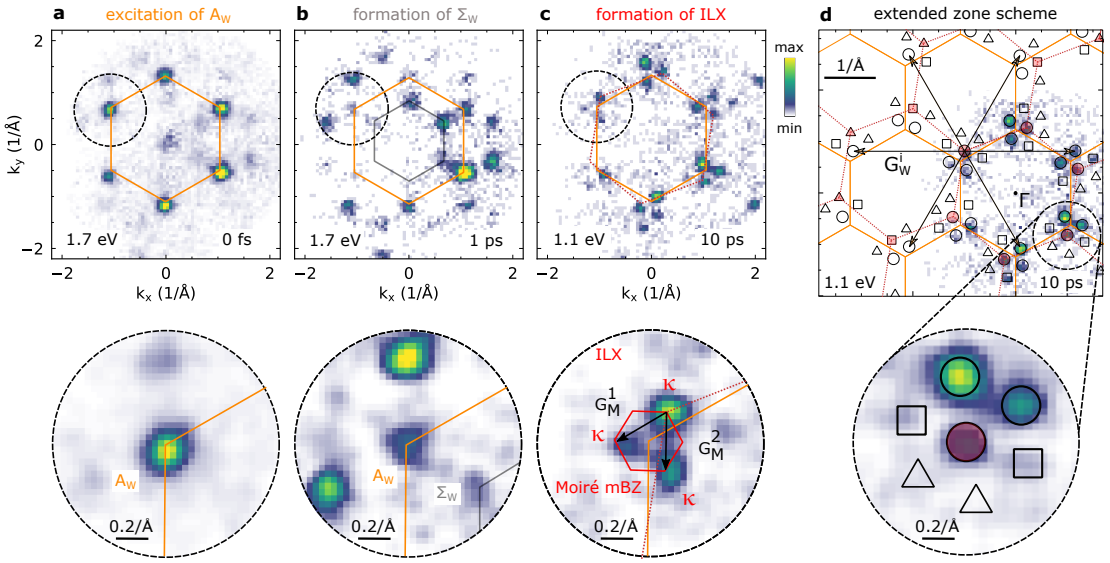

Fig. 3.0.3.: **Momentum-fingerprints of the moiré interlayer excitons.** Momentum fingerprints of **a** the bright A_W-exciton, **b** the dark Σ_W-exciton, and **c** the ILX. Photoemission yield is detected at the respective high-symmetry points of the Brillouin zones of WSe_2, MoS_2, and at the κ valleys of the moiré mini Brillouin zone. The bottom row shows zoom-ins from the circled areas in the top row. **d** The intensity distribution of the momentum-fingerprint of the ILX can be constructed using a generalized umklapp process [133]. Red filled symbols label K_{Mo} valleys of the first (circle) and higher orders (square, triangle) Brillouin zones. Open circles, squares, and triangles represent a hierarchy of expected spectral weight from high to low, resulting from generalized umklapp processes with WSe_2 lattice vectors G^i_W (black arrows).

Having identified the correlation between the ILX momentum fingerprint and the moiré superlattice, we aim to model the distinct photoemission intensity distribution of the ILX. For this purpose, we make use of previous works on interlayer interaction in incommensurate atomic layers [133]. In particular, we follow the notation by Koshino [133], where the interlayer coupling in reciprocal space is expressed in terms of a generalized umklapp process (Fig. 3.0.3d, details in Methods). A straightforward geometrical construction following this work yields the intensity distribution shown in Fig. 3.0.3: highest photoemission yield is expected for momenta marked by circles, which correspond to the κ-points of the mBZ. Weaker photoemission yield is expected in areas marked by squares, which indeed are partially and faintly visible in the data. Finally, negligible signal is expected in momentum areas marked by triangles, consistent with our experimental data.

However, despite the very good agreement of the data with this generalized umklapp process, the interpretation of the momentum structure being a result of interlayer interaction is not obvious, because interlayer coupling at the K valleys was mostly regarded negligibly small due to the in-plane orbital character in this valley [79, 114]. A regular final state scattering can be excluded, since only the ILX signal is exhibiting these replicas. The threefold

signal should also not be a result of an exciton wave function that is confined in a single moiré potential well, since a modification of the relative or center-of-mass motion of the electron-hole pair only becomes significant for large moiré wavelengths, i.e., for twist angles < 2° [9, 14, 119], in agreement with a recent momentum microscopy experiment [101] (see Extended Fig. 3.0.14). Instead, since the photoemitted electron of the ILX has been bound to a hole that remains in the heterostructure, we find here that the umklapp process is transferred via the Coulomb interaction. Thus, in order to imprint the moiré superlattice onto the excitonic photoemission signal, it is necessary that the electron and the hole components are found in the neighbouring TMD layers such that the quasiparticle experiences the lattice periodicities of both. In consequence, for intralayer A_W- and Σ_W-excitons, where electron and hole reside in WSe_2, we do not expect and do also not observe the moiré superlattice hallmark in the momentum-resolved photoemission intensity (Fig. 3.0.3a and b, extended Fig. 3.0.8). In order to unambiguously assign the microscopic origin of the moiré hallmark in the excitonic momentum fingerprint, however, further theory on photoemission from excitonic quasiparticles is necessary. Nevertheless, our analysis shows that the complex momentum structure of the ILX is a hallmark fingerprint of moiré superlattice modification that has not been observed so far and is clearly unique for the ILX in a twisted heterostructure.

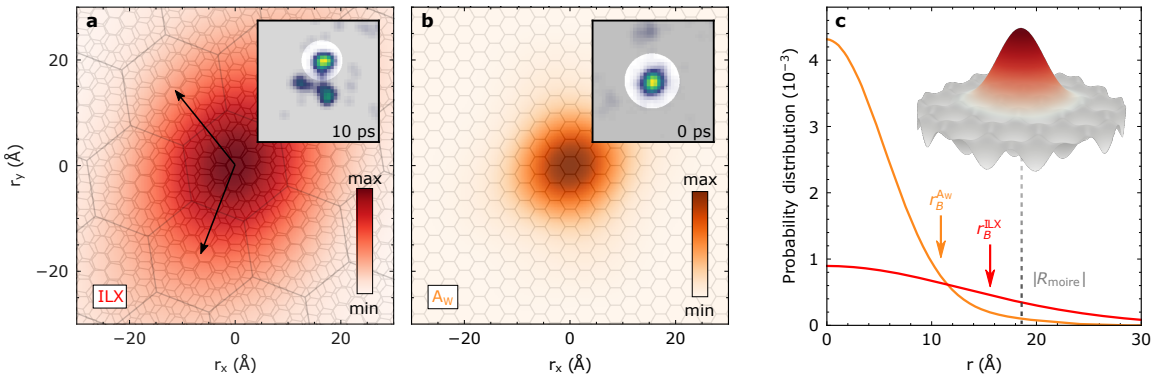

Fig. 3.0.4.: **Real-space exciton wavefunction reconstruction and spatial relation to the moiré superlattice.** Real-space reconstructions of the wavefunction of the electron contribution to the **a** ILX and the **b** WSe_2 A_W-exciton. **a** The overlay with small (atomic lattices of the twisted WSe_2 and MoS_2 layers) and large (moiré lattice) hexagons illustrates the extension of the electron contribution to the ILX wavefunction over multiple moiré unit cells (black arrows: moiré lattice vectors). In **b**, only the lattice periodicity of WSe_2 is overlayed onto the data. The insets show masks used to select a single valley for the reconstruction. **c** Line profiles through the probability density. The inset schematically shows how the electronic contribution to the ILX wavefunction (red) is spread over multiple moiré cells (grey).

ILX real-space wavefunction analysis

Finally, we determine the electron contribution to the real-space wavefunction of intra- and interlayer excitons. We follow the framework of photoemission orbital tomography [104] and

recent developments that have been carried out for TMD excitons [27, 26, 101]. We employ the relation $I(k_x,k_y) \propto \left|FT\{\Psi(r_x,r_y)\}\right|^2$ that connects the real-space wavefunction $\Psi(r_x,r_y)$ with the momentum-resolved photoemission intensity $I(k_x,k_y)$ within the plane wave approximation [104, 27]. The multidimensional data collection scheme now facilitates the direct comparison of the real-space extension $r_{x,y}$ of the electronic wavefunction contribution of the excitons with the spatial extension of the moiré unit cell (Fig. 3.0.4). We extract the respective Bohr radii to r_B^{ILX} =1.6±0.2 nm and r_B^{Aw} =1.1±0.1 nm (root-mean-square), which is in agreement with a recent analysis [101] (see methods). We can draw two conclusions: The extension of the electronic contribution to the ILX wavefunction is larger than the moiré period of the 9.8±0.8° twisted heterostructure ($|R_{\mathrm{moire}}| = 1.84 \pm 0.15$ nm), i.e., the ILX can propagate laterally through the heterostructure and is not confined to a single moiré potential well. Second, the analysis shows that the ILX extension is significantly broader than that of the WSe_2 A_W-exciton. The charge separation across the two TMD layers leads to a weaker attractive interaction between the electron- and the hole-contribution to the exciton and the wavefunction exhibits larger spread in real-space.

METHODS

Heterostructure fabrication.

The WSe_2/MoS_2/hBN heterostructures were assembled using mechanical exfoliation and dry transfer, as summarized in Extended Fig. 3.0.5a-d. First, a p^+-Si substrate (1-10 Ωcm) with polished native oxide was plasma cleaned with O_2 gas (100 W, 10 sccm, 10 mins). hBN was immediately mechanically exfoliated on the Si substrate using standard office tape. Using optical contrast, a hBN flake with thickness between 20-30 nm was identified. In parallel, MoS_2 and WSe_2 (HQ graphene) were mechanically exfoliated using blue tape (Ultron Systems, Inc. 1008R-6.0) on a Polydimethylsiloxane (PDMS) sheet (Gel-Pak PF-20/17-X4). Similar to hBN exfoliation, optical contrast was used to identify monolayer MoS_2 and WSe_2. Unlike the standard dry transfer assembly, the assembly of the heterostructure was started by assembling the WSe_2/MoS_2 heterostructure on PDMS first. The two flakes were aligned visually and the MoS_2 flake was dry transferred on top of the WSe_2 flake on PDMS. Then the WSe_2/MoS_2 heterostructure was dry transferred on top of the hBN. During the last transfer, the multilayer part of the WSe_2 flake was intentionally placed in direct contact with the Si substrate to reduce sample charging (cf. Extended Fig. 3.0.5e,f). It is worth noting that while the exfoliation part was done in ambient condition, the heterostructure assembly was done in a controlled Ar environment in a glovebox with O_2 and H_2O <0.1 ppm. An optical microscope image of the van-der-Waals stack is shown in Extended Fig. 3.0.5e.

Sample preparation for photoemission spectroscopy.

The silicon wafer with the heterostructure is clamped onto a sample holder under ambient conditions and transferred into ultrahigh vacuum (UHV). In an UHV preparation chamber (background pressure $< 5\times10^{-9}$ mbar), the sample is annealed for 2 hours at a temperature of approximately 670 K; such sample treatment has shown successful ARPES results on similar sample systems, e.g., Ref. [134]. Subsequently, the sample is transferred into the momentum microscope. All experiments have been performed at room temperature at a background pressure of approximately 1×10^{-10} mbar.

Femtosecond momentum microscopy.

The experimental setup is detailed and benchmarked in Ref. [29]. It consists of two major parts, namely, (i) a time-of-flight momentum microscope [35] (METIS, Surface Concepts), shown schematically in Fig. 3.0.1a of the main text, and (ii) a high-power femtosecond laser system (Active Fiber Systems). In the following, we will briefly describe the experimental setup.

(i) The strength of the time-of-flight momentum microscope is the simultaneous measurement of the 2D in-plane momenta and the kinetic energy of the photoelectrons within the full photoemission horizon [35]. In order to study high-quality TMD heterostructures with a diameter of approximately 10 μm, however, the key advantage of the setup lies in the microscopy-type

photoelectron detection scheme: In the electrostatic lens system, a real- and a reciprocal-space image of the photoelectrons is formed and either image can be projected onto the photoelectron detector (Fig. 3.0.1a). The real-space mode of the microscope is used to map the spatial structure of the sample system (Fig. 3.0.1c, Extended Fig. 3.0.5f). In direct comparison to an optical microscope image (Extended Fig. 3.0.5e), the monolayer WSe_2 and MoS_2 regions as well as the WSe_2/MoS_2 heterobilayer region can be identified via the differing photoemission contrast. By placing an aperture into the real-space plane of the microscope, either photoelectrons originating from the WSe_2 mono- or the WSe_2/MoS_2 heterobilayer can be selected and projected onto the detector (Extended Fig. 3.0.6). By exploiting this capability of the time-of-flight we collect in-plane momentum- and energy-resolved photoelectron distributions for the regions of interest highlighted by circles in Fig. 3.0.1c of the main text. The energy resolution of the momentum microscope combined with the spectral width of the 26.5 eV extreme ultraviolet (XUV) light pulses lead to an overall Gaussian broadening of the measured photoelectron signal with a full width at half maximum of 200±30 meV [29]. The achievable momentum resolution of the instrument is <0.01 $Å^{-1}$ [135]. From a fit of the cut-off of the photoemission horizon, we can verify that the momentum resolution for the given experimental settings in the article is better than 0.04±0.01 $Å^{-1}$. The time resolution is 54±7 fs for infrared pump pulses of 50±5 fs and XUV probe pulses of 21±5 fs as used in this experiment [29]. This value is confirmed with a fit to the replica signal caused by the laser-assisted photoelectric effect (LAPE) [136, 29] (see, e.g., Fig. 3.0.3a or Extended Fig. 3.0.10c at 0 fs delay), which yields an infrared-pump−XUV-probe cross-correlation of 49±1 fs.

(ii) The laser setup is based on a 300 W fiber laser system (Active Fiber Systems) that operates at a repetition rate of 500 kHz and drives a high-harmonic generation beamline and a high-power optical parametric amplifier (OPA, Orpheus-F/HP from Light Conversion). In order to first induce and subsequently probe excitonic dynamics occurring in the TMD heterostructure (Fig. 3.0.2), we employ a pump-probe scheme: First, bright WSe_2 A_W-excitons are excited with light pulses generated with the OPA (1.7 eV, 50±5 fs measured per autocorrelation). Subsequently, the femto- to picosecond evolution of the intra- and interlayer excitonic dynamics is probed with an extreme ultraviolet light pulse (26.5 eV, *p*-polarized, 21±5 fs [29]), which photoemits the electron contribution of the quasiparticle into the detector. Additional experiments are performed with 1.9 eV and 2.4 eV pump light, which is generated through the OPA and frequency doubling of the compressed laser output, respectively. Data in Figs. 3.0.1b, 3.0.2, and Extended Figs. 3.0.8c, 3.0.8d, 3.0.9, 3.0.11, 3.0.12a, 3.0.12b, 3.0.13 are obtained with *s*-polarized pump light. Data in Figs. 3.0.3, 3.0.4, and Extended Figs. 3.0.8a, 3.0.8b, 3.0.10 are obtained with *p*-polarized pump light. For *p*-polarized pump, one creates band replicas due to the laser-assisted photoelectric effect (LAPE), which then can be used to determine pump probe overlap (time-zero) and the time-resolution [136, 128]. For *s*-polarized pump, the time-resolved signal is free of such LAPE replicas, which is helpful for the analysis of spectral features and exciton dynamics.

Real-space imaging and static band mapping of WSe_2/MoS_2/hBN.

After preparation of the van-der-Waals stack for the momentum microscopy experiment, we first perform real-space imaging of the sample with a UV-diode delivering 4.96 eV photons. In Extended Fig. 3.0.5f, the photoemission real-space map is compared with an optical microscope image. In both images, the WSe_2/MoS_2/hBN heterostructure, the doped Si substrate, the bulk hBN, the WSe_2 and MoS_2 monolayers, and the bulk WSe_2 can be distinguished.

Having identified the regions of interested, we place an aperture into the real-space image of the microscope in order to selectively probe the energy- and momentum-resolved photoelectron distribution of the WSe_2 monolayer and the WSe_2/MoS_2 heterobilayer. For this, we place an aperture with a diameter of 100 μm into the real-space plane of the microscope (cf. Fig. 3.0.1]a), and, using a lens setting with a magnification of 10, we are sensitive to photoelectrons originating from an effective area with diameter of 10 μm on the heterostructure (circles in Fig. 3.0.1c).

Static band mapping of the occupied electronic band structure is shown in Extended Fig. 3.0.6. The high quality of the van-der-Waals stack is evident by the well-resolved features in the band structure and, in particular, by the visible spin-splitting of the WSe_2 valence bands at the K_W and K'_W valleys [99] (marked with (1) and (2) in Extended Fig. 3.0.6). In addition, only in the heterobilayer region, we resolve clear signatures of the valence band maximum of MoS_2 at -1.1 eV with respect to the valence band maximum of WSe_2 (marked with (3) in Extended Fig. 3.0.6b). Due to interlayer interaction between the WSe_2 and MoS_2 layers, we resolve the expected hybridized valence bands at the $\Gamma_{W,M}$ valley (marked with (4) and (5) in Extended Fig. 3.0.6b) [129]. The observation of these hybridized bands is a clear signature that the blisters found in the real-space image in Extended Fig. 3.0.5e,f do not dominate the photoemission yield from the heterobilayer. In contrast, in the monolayer WSe_2 region, the valence band at the Γ_W valley is a single band (Extended Fig. 3.0.6a). Furthermore, the valence band maximum is localized at the K_W (K'_W) valley, as expected for the monolayer limit of WSe_2, where it becomes a direct band gap semiconductor [129]. In addition, we observe a clear signature of the valence band of hBN that we label with (6) in Extended Fig. 3.0.6a). Within our energy- and momentum-resolution, we do not resolve moiré induced mini-band replicas of the valence bands, such as discussed in refs. [134, 137].

Inhomogeneous broadening from sample.

In our experiment, the energy resolution is mainly limited by the bandwidth of the short-pulse extreme ultraviolet light source. Convolved with the instrument resolution, we achieve a total energy resolution on the order of $\approx$200 $\pm$ 30 meV [29]. For reference, Extended Fig. 3.0.7 shows an exemplary energy-distribution curve obtained in a momentum-region of $\pm$ 0.10 $Å^{-1}$ centered at the K'_W valley. As in the case of Ref. [24], we extract a full width

at half maximum (FWHM) of ≈280 ± 10 meV. However, our spectrum is broadened by ≈200 meV by the light source and the instrument, so that the FWHM peak width of the valence band maximum is on the order of 200 meV. This broadening is attributed to, e.g., inhomogeneity of the sample and local field effects.

Twist-angle determination of the WSe_2/MoS_2 heterostack.

In trARPES experiments, it is known that the electron contribution of the A-excitons are identified via spectral weight at the corresponding K-valleys of the TMD structure [25, 27, 24]. In consequence, the photoemission signature of the A_W- and A_{Mo}-excitons can directly be used to determine the twist angle of a heterostructure. Here, for the unambiguous identification of the A_W- and A_{Mo}-excitons in the K_W- and K_{Mo}-valleys, we carry out resonant excitation using 1.7 eV and 1.9 eV pump light, respectively.

In Extended Fig. 3.0.8, we show momentum maps of the resonantly pumped WSe_2 A_W-exciton (3.0.8a), the resonantly pumped MoS_2 A_{Mo}-exciton (4c), and the corresponding signature of the ILX after a delay of 1 ps (4b, d). From the misalignment of the $\Gamma - K_W$ and $\Gamma - K_{Mo}$ directions (orange and brown dashed lines), we calculate the momentum mismatch between the K_W and the K_{Mo} valleys, and, accordingly, determine the twist angle to $\Theta = 9.8 \pm 0.8°$. The direct comparison with the 1 ps data in Extended Fig. 3.0.8b and d then facilitates the correlation of the ILX momentum signature to the in-plane momenta of the K_W and the K_{Mo} valleys.

Spectral assignments of conduction/valence bands and the $A_{W,Mo}$-excitons.

In the main text, we study the ultrafast exciton dynamics of the heterobilayer after resonant excitation of the A_W-exciton of WSe_2 with 1.7 eV pump pulses. In order to unambiguously identify the photoemission signatures shown in Fig. 3.0.2 and 3.0.3 as excitons, Extended Fig. 3.0.9a and b shows energy-momentum cuts when employing above-band-gap excitation conditions with 2.4 eV pump pulses to the monolayer WSe_2 region indicated by the orange circle in Fig. 3.0.1c. In temporal overlap of the pump and probe laser pulses (0 fs), above band-gap excitation allows for the transient occupation of the conduction band and we correspondingly observe parabolic bands with positive dispersion centered at $E\text{-}E_{VBM} \approx 1.8$ eV at the K_W valley. As the delay is increased to 300 fs, the spectral yield at the K_W shifts to smaller energies and the parabolic signature transfers to a more spherical shape. We attribute the photoemission yield from the parabolic dispersion at 0 fs to photoelectrons originating from both higher quantum number excitons and charge carriers from the conduction band of WSe_2, as has been described previously and is in full agreement with Ref. [24]. Subsequently, the delay-dependent shift of the spectral weight to smaller energies can be understood by the formation of excitons (c.f., energy-distribution curves in Extended Fig. 3.0.9b). In Extended Fig. 3.0.9c, we compare the above-band-gap excitation results with energy-distribution-curves obtained from the 1.7 eV pump-light experiment. Under these resonant excitation conditions, already

at 0 fs pump-probe delay the exciton signal is observed at E-E_{VBM} ≈1.7 eV. Importantly, the signal does not decrease in energy with proceeding delay and does not show a positive parabolic dispersion (cf. Fig. 3.0.1b and Extended Fig. 3.0.9).

By repeating the same analysis as described above for a monolayer MoS_2 sample, we can discriminate the A_{Mo}-exciton from charge carriers in the conduction band minimum (Extended Fig. 3.0.9d, e, f). Note that we do not resolve the pump-probe delay-dependent energy shift for the case of MoS_2, but the parabolic momentum-dispersion at 0 fs can again be distinguished from the more spherical shape at 250 fs.

Additional time-resolved momentum microscopy data of the twisted WSe_2/MoS_2 heterostructure.

Extended Fig. 3.0.10 summarizes, in addition to Fig. 3.0.3 (main text), E(k) and k_x-k_y momentum maps of the formation dynamics of the ILX.

Filtering excitonic photoemission signatures in energy- and momentum-space for Fig. 3.0.2c.

The time-of-flight momentum microscope collects in-plane momentum and energy-resolved data cubes for each pump-probe delay [29]. In order to monitor the pump-probe delay-dependent exciton dynamics, the excitonic photoemission signatures need to be filtered on these coordinates in order to avoid mixing of different photoemission signals. Therefore, in Extended Fig. 3.0.11a and b, we show two momentum-maps that are integrated for all measured pump-probe delays in an energy window between E-E_{VBM} = 1.5-2.4 eV and 0.8-1.3 eV, respectively. First, we recognize that the signal of the Σ_W-exciton (black circle) can be easily separated from the A_W-exciton (orange) and the ILX (red) in momentum space. Still, we choose the lower bound of the integration window for the Σ_W-exciton signal well above the energy of the ILX on the energy-axis to determine the pump-probe delay-dependent spectral weight plotted in Fig. 3.0.2c (integration window E-E_{VBM} = 1.5-2.4 eV). The separation of the spectral weight of the A_W-exciton and ILX needs to be further analyzed and filtered on the energy axis as, in momentum-space, the regions of interest are close to each other. From the evolution of the energy distribution curves of the A_W-exciton-momentum-filtered areas in Extended Fig. 3.0.11c (upper panel), it is obvious that the A_W-photoemission signal strongly dominates over the ILX signal for E-E_{VBM} > 1.5 eV. In consequence, in Fig. 3.0.2c, we plot the A_W-exciton signal as obtained within the momentum-region indicated by the orange circles in Extended Fig. 3.0.11a and for E-E_{VBM} = 1.5-2.4 eV (orange boxed energy region in Extended Fig. 3.0.11c (upper panel)). For the ILX signal, the correct identification of the energy integration window is more complex and therefore further analyzed based on the evolution of the energy distribution curves of the ILX-momentum-filtered areas in Extended Fig. 3.0.11c, middle panel. In order to separate the signal of the ILX, which is centered at E-E_{VBM} ≈1.1 eV, from the photoemission yield at higher energies, we systematically vary the energy window that is used to integrate the ILX signal (blueish boxes in

Extended Fig. 3.0.11c, middle panel). The resulting spectral weight vs. pump-probe delay plots are shown in the bottom panel of Extended Fig. 3.0.11c. For small energy integration boxes (dark blue and blue), we find an identical evolution of the spectral weight that we attribute to the ILX. However, as the box becomes too large (light blue), at ≈50 fs, spurious signal from higher energies leads to deviations. In consequence, we use the appearance of this additional photoemission signal at ≈50 fs to determine the upper bound of the maximum energy integration window for the ILX to E-E_{VBM} < 1.3 eV. This sets the boundaries for the energy integration box of the ILX to E-E_{VBM} = 0.8-1.3 eV, which is plotted in Fig. 3.0.2c in the main text.

Correction of space-charge/photovoltage effects.

In trARPES experiments, even in the sub 1 mJ/cm^2 fluence regime, one often observes space-charge and/or photovoltage effects, which are induced by Coulomb interaction of photoelectrons or the remaining holes, which were excited by the pump laser, with the probe-photoelectrons of interest that are studied in the trARPES spectrum [138, 139, 140]. These effects are well known in the trARPES community and, in a moderate regime, only cause a rigid spectral shift of all probe-photoelectrons, i.e., a shift of the entire photoelectron spectrum. In this regime, one automatically monitors space-charge/photo-voltage-induced shifts when collecting the trARPES data and one correspondingly corrects for these 'rigid' shifts before analyzing the data. For all data presented in our manuscript, we observe such rigid shifts of the full ARPES spectrum, which is on the order of several meV up to a maximum of about 70 meV (Extended Fig. 3.0.12a). The pump-probe delay dependent energy difference ΔE is calculated by fitting a selected peak in the full momentum-integrated energy-distribution-curves and subtracting its energy position from the reference measurement data shown in the inset. Although this energy difference ΔE is small in comparison to our energy resolution and barely influences the analysis procedure, we routinely correct our data for these effects before carrying out the data analysis. This means that all data shown in this article are corrected for this rigid energy offset. Note that for the analysis of the ILX momentum-fingerprint, the energy-shift is irrelevant, because the data is analyzed on the picosecond timescale.

Determination of the exciton density.

It has been shown in TMDs that for optical pumping with sufficiently high fluence a Mott transition from excitonic states to free carriers can be induced when the excited exciton density is in the range of 10^{12}-10^{14} cm^{-2} [58, 141, 142, 143, 48]. This transition leads to giant band-gap renormalizations of up to 500 meV [58] and thus might influence our interpretation of A_W-exciton generation and the subsequent dynamics. In the following, we (i) describe the calculation of the exciton density in our experiment, and subsequently show (ii) pump-probe delay dependent energy distribution curves of the valence band maxima of WSe_2 in order to directly exclude the contribution of band renormalizations to our experimental analysis.

(i) Using the real-space mode of the microscope, we can extract the $1/e^2$ radius of the pump

beam on the sample to 151 ± 1 μm. For the data shown in Fig. 3.0.2c, the heterostructure was irradiated with *s*-polarized 1.7 eV photons with a peak fluence of 280 ± 20 $\mu J/\text{cm}^2$. By following the analysis of Ref. [141], we calculate the absorbed fluence to be 1.5 ± 0.2 $\mu J/\text{cm}^2$, which results in an exciton density of $(5.4 \pm 1.0) \times 10^{12}$ cm^{-2}. Because this exciton density is in the 10^{12}-10^{14} cm^{-2} threshold regime [58, 141, 142, 143, 48], it is important to provide experimental evidence that our experiment probes excitons and not quasi-free carriers in the conduction bands.

(ii) We therefore analyze our data for the possible generation of quasi-free carriers and the according renormalization of the band structure. In Extended Fig. 3.0.12b, we monitor the position of the WSe_2 valence band maximum at the K_W valley in comparison to the position at -2 ps as a function of delay, which, in the case of generation of quasi-free carriers, is expected to strongly up-shift in energy (c.f. [58]). In the work by Liu *et al.* using trARPES, for example, the energetic position of the valence band maximum shifts up by 360 meV and then relaxes back to its unperturbed value on the picosecond timescale [48]. Importantly, within the scattering of our data (about $\pm$50 meV in Extended Fig. 3.0.12b), the photoemission energy of the valence band edge at the K_W valley does not change with pump-probe delay. In particular, it does not upshift in energy, as would be expected for an exciton density above the Mott threshold. This directly implies that the dominant excitation in our experiment is governed by A_W-excitons in WSe_2, from which the subsequent exciton dynamics is induced, whereas the role of quasi-free carriers is negligible. Please note that the error bars around 0 fs are enlarged because of a typical broadening of the occupied bands in temporal overlap (c.f. Extended Fig. 3.0.10a,b).

Quantitative analysis of charge-transfer times to the Σ_W-excitons and the ILX.

The intermediate steps of the exciton dynamics occurring in the WSe_2/MoS_2 heterostructure are summarized in the excitation diagram shown in the inset of Fig. 3.0.2c: A_W-excitons are resonantly excited with 1.7 eV pump photons, exciton-phonon scattering leads to the formation of Σ_W-excitons, and, subsequently, ILX are formed via interlayer tunneling at the Σ-valleys. Typically, one would use a rate-equation-model in order to quantify the respective charge transfer times. However, this approach is not feasible here, as it does not accurately describe the coherent polarization induced while the pump pulse is present on the sample [25]. In addition, because of photoemission cross section effects, we cannot unambiguously correlate the measured photoemission signal to the exciton occupation density, as would be necessary in order to extract meaningful transfer rates from a rate-equation model. Therefore, we assume the most simple model for a quantitative analysis: The states are filled by a Gaussian excitation or transfer rate. This rise in spectral weight follows an errorfunction. In Extended Fig. 3.0.13a, we fit the pump-probe delay-dependent spectral weight with error functions $I/I_{\text{max}} = 0.5 \cdot (\text{erf}((t - t_i)/w) + 1)$, which give us access to the delayed onset t_{Σ_W} and t_{ILX} of the photoemission yield from the Σ_W-exciton and the ILX, respectively, in comparison to the build-up of the A_W-exciton (t_{A_W}). We calculate delayed onset times of

$t_{\Sigma_W} - t_{A_W} = 33\pm6$ fs and $t_{ILX} - t_{A_W} = 54\pm7$ fs. These delayed onsets are in overall agreement with earlier reports on charge transfer on the WSe_2/MoS_2 system [89, 88], however, the momentum-resolved data collection scheme now facilitates the separate extraction of this dynamics for the intermediate Σ_W-excitons.

Long-term picosecond relaxation dynamics of the observed excitons.

Extended Fig. 3.0.13b shows the picosecond exciton relaxation dynamics of the WSe_2/MoS_2 heterostructure. In accordance with the snapshots in Extended Fig. 3.0.10, at 10 ps pump-probe delay, photoemission yield from the A_W-exciton and the Σ_W-exciton is at the detection limit of the experiment. In contrast, for the ILX, significant photoemission yield is still present at this time delay and remains beyond delays of 50 ps, which is the largest delay measured in our experiment. In extended Fig. 3.0.13b, we quantify this observation and fit the relaxation dynamics of the excitons with single-exponential decays, for which we extract lifetimes of 3.1 ± 0.3 ps, 3.0 ± 0.4 ps, and 33.2 ± 4.7 ps for the A_W-exciton, the Σ_W-exciton, and the ILX, respectively. We find that the ILX lifetime is an order of magnitude larger than the lifetimes of the intralayer excitons, in agreement with earlier reports [88]. In addition, we note that the lifetimes of the intralayer excitons in the heterostructure are considerably quenched in comparison to the lifetime of the intralayer excitons in the WSe_2 monolayer (see Fig. 3.0.2a and 3.0.2b in the main text), which is caused by the additional decay channel into the ILX.

Construction of the ILX momentum fingerprint in the extended zone scheme in Fig. 3.0.3

We follow the interlayer interaction model by Koshino [133] in order to describe the intensity distribution of the ILX fingerprint in momentum space. In Fig. 3.0.3d, we plot the measured ILX momentum distribution at 10 ps pump-probe delay together with the twisted extended zone schemes of WSe_2 (orange hexagons) and MoS_2 (dotted brown hexagons). The K_{Mo} valleys, at which the electron contribution to the ILX is expected without contribution of the moiré superlattice, are labelled with red filled symbols. The increasing momentum-distance of the K_{Mo} valleys in higher order Brillouin zones with respect to the Γ valley of the center Brillouin zone is indicated by the changing red symbols, i.e., the transition from circles to squares and to triangles. By umklapp scattering with the lattice vector G^i_W of WSe_2 (black arrows), i.e., the periodicity of the layer where the hole contribution to the ILX is localized, the momenta indicated with open symbols can be reached. As detailed in refs. [133, 144], the efficiency for umklapp scattering decreases with increasing distance from the Γ valley of the center Brillouin zone. In consequence, we observe a strong hierarchy of photoemission signal from the ILX: Strongest photoemission signal is found and expected at the momenta labelled with circles. Weaker and negligible signal is found at the momenta labelled with squares and triangles, respectively.

For heterostructures with different twist angles, the ILX momentum structure is modified accordingly. This is exemplarily illustrated in extended Fig. 3.0.14 for twist angles of 9° and 2°. Here, the 2°-illustration corresponds to the sample structure of a recent work by Karni *et al.* [101], and shows that for finite momentum resolution and small twist angles, the ILX momentum structure that we found in our work cannot be resolved.

Real-space reconstruction.

Following the plane-wave model for photoemission, the measured ARPES intensity $I(\vec{k})$ can be expressed as

$$I(\vec{k}) = |\vec{A}\cdot\vec{k}|^2 \; |FT\{\psi(\vec{r})\}|^2 \; \delta(E_b + E_{kin} + \Phi - \hbar\omega), \tag{3.1}$$

which includes the Fourier transform of the real-space electronic wave function $\psi(\vec{r})$, a polarization factor $|\vec{A}\cdot\vec{k}|^2$ which depends on the vector potential $\vec{A}$ of the incident radiation and electron momentum $\vec{k}$, and a Dirac delta function which ensures conservation of energy. Because the electronic contribution to the interlayer excitonic quasiparticle is confined to a single MoS_2 monolayer, we can treat it similar to how it is done for orbital tomography of molecular orbitals in planar aromatic molecules [104, 145], in agreement with the approach that has been recently carried out for excitons in TMDs [27, 26, 101]. Here, the wave function is assumed to be thin in the vertical dimension and photoemission is therefore assumed to be independent of the out-of-plane momentum k_z.

We start our analysis based on the momentum maps of the A_W-exciton and the ILX. As highlighted in the main text based on the insets in Fig. 3.0.4a and 3.0.4b, we perform separate two-dimensional Fourier transforms to each excitonic photoemission feature in order to reconstruct the real-space extension of the electronic contribution to the exciton wavefunction, as plotted in Fig. 3.0.4a and 3.0.4b for the ILX and the A_W-exciton, respectively. In this analysis, we have eliminated broadening effects due to the finite momentum resolution of the momentum microscope (0.04 $Å^{-1}$) using Wiener-Hunt deconvolution and subtracted a weak background determined from the full data set. Finally, we assumed a flat phase profile over the full accessible momentum range, following the approach detailed in Ref. [27]. In order to determine the Bohr radii, we calculate the root-mean-square radii of the real-space probability density distribution. The Bohr radii for the electron contribution to the ILX and the A_W-exciton are r_B^{ILX} =1.6±0.2 nm and $r_B^{A_W}$ =1.1±0.1 nm, respectively, and were acquired by taking the weighted average of the Bohr radii determined for individual κ and K_W valleys. For the ILX, only the features with a signal to noise ratio better than 10 were taken into account.

Note that on the heterostructure with a twist angle >5°, we can safely assume in our analysis that the center-of-mass momentum is narrowly distributed around zero [132, 14], and the momentum-width of the photoemission signatures at the κ and K_W valleys relates to the relative coordinate of the excitons [101]. In a recent report on a 2° twisted WSe_2/MoS_2 heterostructure, Karni *et al.* [101] reported the root-mean-square radius of the relative coordinate

to the ILX wavefunction to 2.6±0.4 nm. This corresponds to a root-means-square radius of the probability density of 1.8±0.3 nm, which is in agreement with our analysis of a Bohr radius of r_B^{ILX} =1.6±0.2 nm. Similarly, our reconstructed Bohr radius of the A_W-exciton of $r_B^{\mathrm{A_W}}$ =1.1±0.1 nm is in agreement with the root-mean-square radius of the probability density of WSe_2 of Ref. [26] (≈1.0 nm).

ACKNOWLEDGEMENTS

This work was funded by the Deutsche Forschungsgemeinschaft (DFG, German Research Foundation) - 432680300/SFB 1456, project B01, 217133147/SFB 1073, projects B07 and B10, and 223848855/SFB 1083, project B9. G.S.M.J. acknowledges financial support by the Alexander von Humboldt Foundation. A.A. and S.H. acknowledge funding from EPSRC (EP/T001038/1, EP/P005152/1). A.A. acknowledges financial support by the Saudi Arabian Ministry of Higher Education. K.W. and T.T. acknowledge support from the Elemental Strategy Initiative conducted by the MEXT, Japan (Grant Number JPMXP0112101001) and JSPS KAKENHI (Grant Numbers 19H05790, 20H00354 and 21H05233). E. M. acknowledges support from the European Unions Horizon 2020 research and innovation programme under grant agreement no. 881603 (Graphene Flagship) as well as Vinnova via the competence centre “2D-TECH".

DATA AVAILABILITY

The data that support the findings of this study are available from the corresponding authors upon reasonable request.

COMPETING INTERESTS

The authors declare no competing interests.

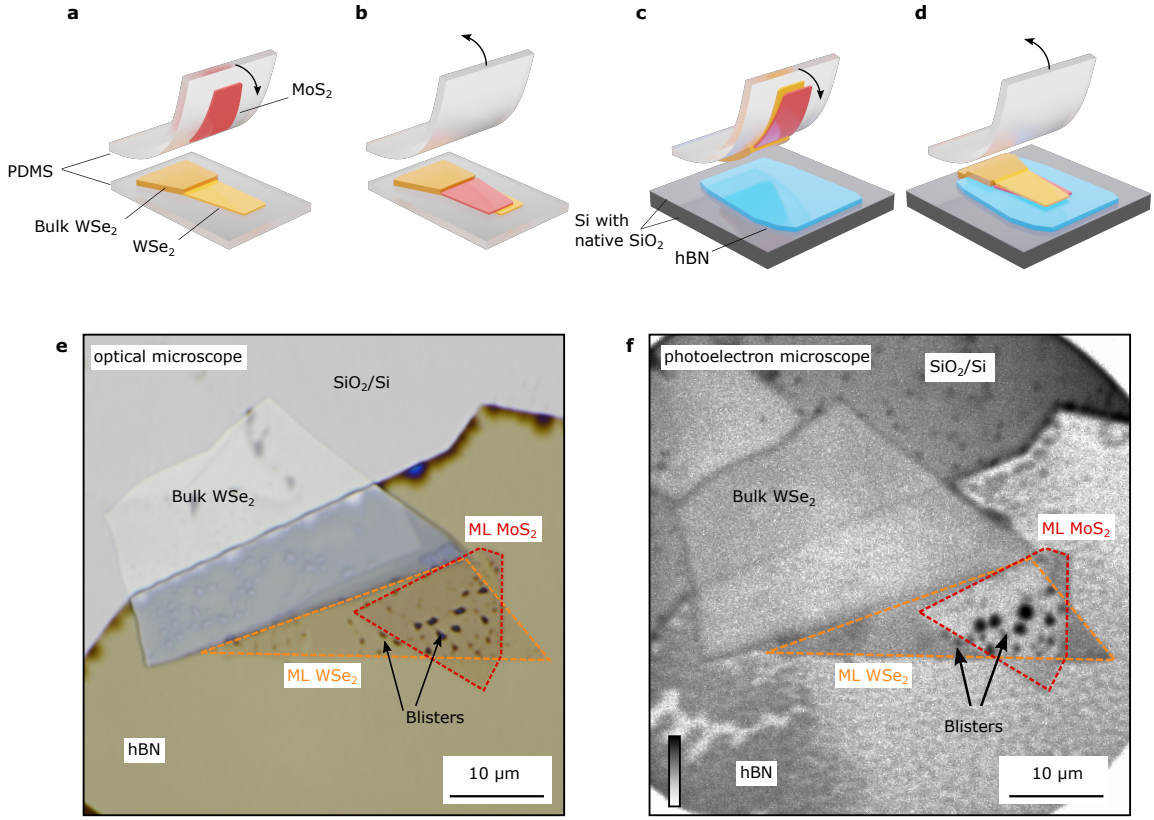

Extended Fig. 3.0.5.: **Fabrication and real-space imaging of the of the WSe_2/MoS_2/hBN heterostructure. a-d** Schematic of the WSe_2/MoS_2/hBN heterostructure assembly on a Si substrate with a native oxide layer. **a** A PDMS stamp with monolayer MoS_2 flake (red) is aligned with another PDMS stamp holding a monolayer WSe_2 (yellow), then the top PDMS stamp is brought in contact with bottom PDMS. **b** The top PDMS stamp is then withdrawn, leaving the MoS_2 on top of the WSe_2. **c** The PDMS stamp holding the WSe_2/MoS_2 is then brought into contact with SiO_2/Si substrate with hBN (blue). **d** the PDMS is then withdrawn, leaving behind the final WSe_2/MoS_2/hBN heterostructure. **e/f** The WSe_2/MoS_2/hBN heterostructure, the uncovered SiO_2/Si substrate, bulk hBN, the WSe_2 and MoS_2 monolayers, and bulk WSe_2 are labelled in the **e** optical microscope and the **f** photoemission real-space image ($\hbar\omega$ = 4.96 eV). Point-like structures (blisters) in the heterostructure region can be attributed to residual gas trapped either at the MoS_2/hBN or the WSe_2/MoS_2 interface. The blisters in the monolayer WSe_2 region are most likely trapped at the WSe_2/hBN interface.

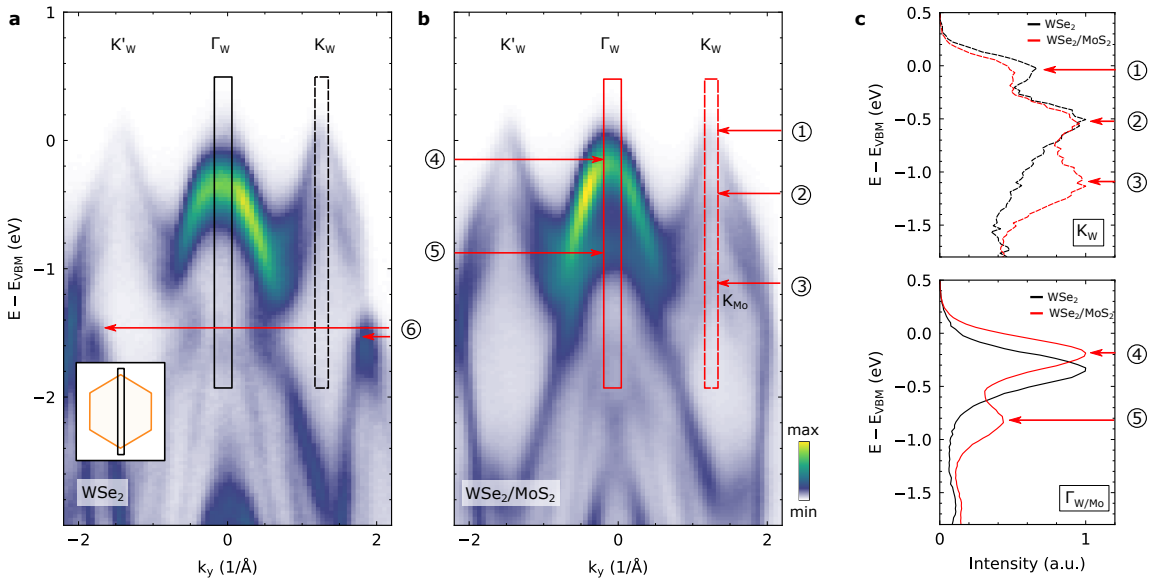

Extended Fig. 3.0.6.: **Static band mapping of the monolayer WSe_2 and the heterobilayer WSe_2/MoS_2. a,b** Energy-momentum representation of the static photoemission intensity obtained in the momentum microscopy experiment along the K'$_W$-Γ-K$_W$ direction (see inset). The important spectroscopic features are labelled in the figure: (1, 2) spin-split valence bands of WSe_2; (3) valence band of MoS_2; (4, 5) valence bands at the $\Gamma_{W,Mo}$ valley; (6) valence band of hBN. **c, d** Energy distribution curves taken around the K$_W$ and $\Gamma_{W,Mo}$ (Γ_W) valley indicated by the colored boxes in **a** and **b**.

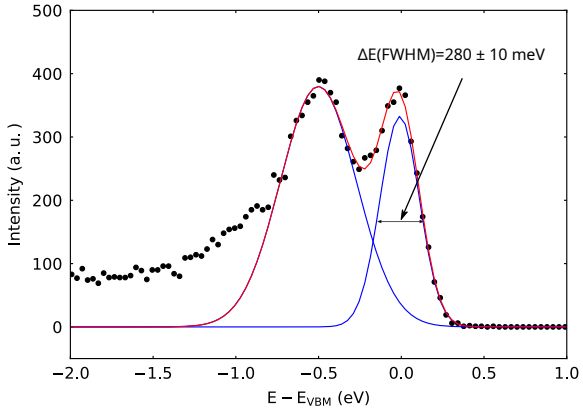

Extended Fig. 3.0.7.: **Inhomogeneous broadening of the photoemission spectra.** The energy-distribution-curve is obtained in a $\pm$ 0.10 Å^{-1} region-of-interest centered at the K'$_W$ valley of WSe_2. Gaussian fitting of the valence band maximum centered at E-E$_{VBM}$=0 eV yields a full width at half maximum of 280$\pm$10 meV.

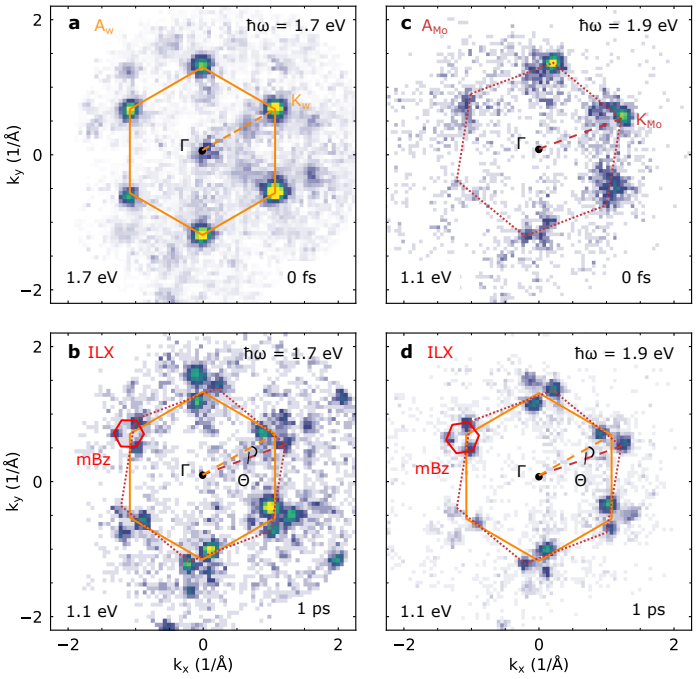

Extended Fig. 3.0.8.: **Determination of the twist-angle Θ of the WSe_2/MoS_2 heterostructure.** The momentum maps in **a** and **c** show the photoemission fingerprint of the A_W- and A_{Mo}-excitons when excited resonantly with 1.7 eV and 1.9 eV photons, respectively, at 0 fs pump-probe delay. Since the MoS_2 A_{Mo}-exciton and the ILX are, within our energy resolution, spectrally degenerate, faint signatures of the ILX are already visible **c** at 0 fs delay. The dashed lines indicate the $\Gamma - K_W$ (orange) and $\Gamma - K_{Mo}$ (brown) direction. From their misalignment, the twist angle is extracted to Θ=9.8±0.8°. **b, d** At 1 ps pump-probe delay, the ILX momentum fingerprint can be identified, as described by the mBZ (red). The dashed lines indicate the relation of the ILX momentum fingerprint and the $\Gamma - K_W$ and $\Gamma - K_{Mo}$ directions. Note the distinctly different intensity distribution of the combined spectral weight of the A_{Mo}-exciton and the faint ILX in **c** vs. the pure signature of the ILX at 1 ps delay in **d**. For each momentum-map, the photoelectron energy with respect to the valence band maximum of WSe_2 and the pump-probe delay are noted in the lower left and right corner, respectively.

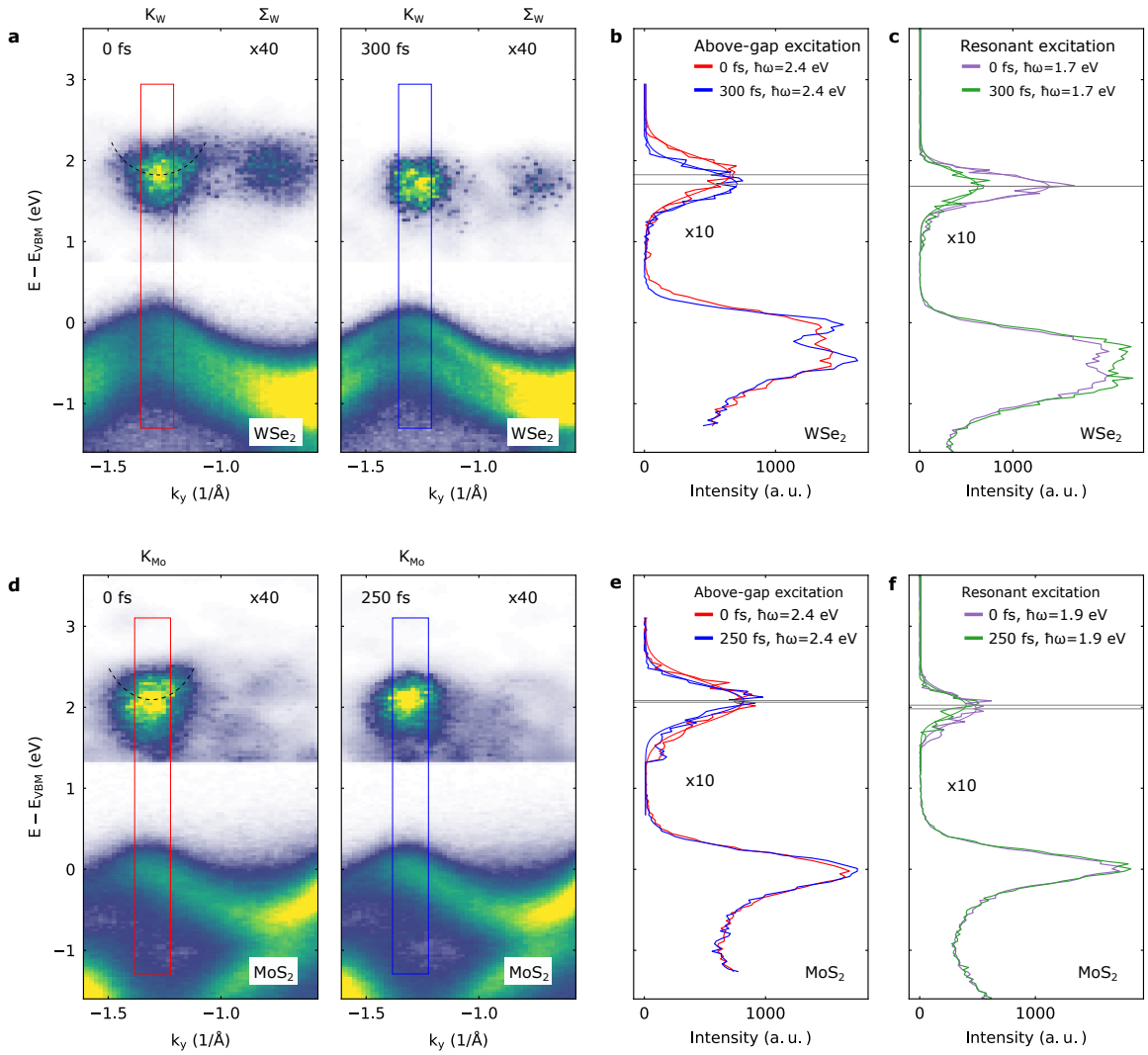

Extended Fig. 3.0.9.: **Above-band-gap excitation of monolayer WSe_2 and monolayer MoS_2.** Photoemission yield from bright intralayer excitons and charge carriers in the conduction can be discriminated based on above-band-gap excitation data collected on **a-c** monolayer WSe_2 (orange circle in Fig. 3.0.1c) and **d-f** monolayer MoS_2 (real-space image not shown). **a** And **d** show energy-momentum cuts along the K-Σ direction measured on WSe_2 and MoS_2, respectively, at 0 fs and 300 fs (respectively 250 fs) pump-probe delay. At 0 fs, a parabolic signature with positive dispersion is detected at the K valley (noted by the black dashed parabolic line). At 300 fs (250 fs), the signature becomes more spherical. **b** and **e** show energy-distribution-curves at the K valleys (momentum-integration region based on the boxes in **a, d**). The peak maxima is indicated by grey horizontal lines. **c** and **f** show the corresponding energy-distribution-curves when excited on resonance with the A_W- and A_{Mo}-exciton, respectively.

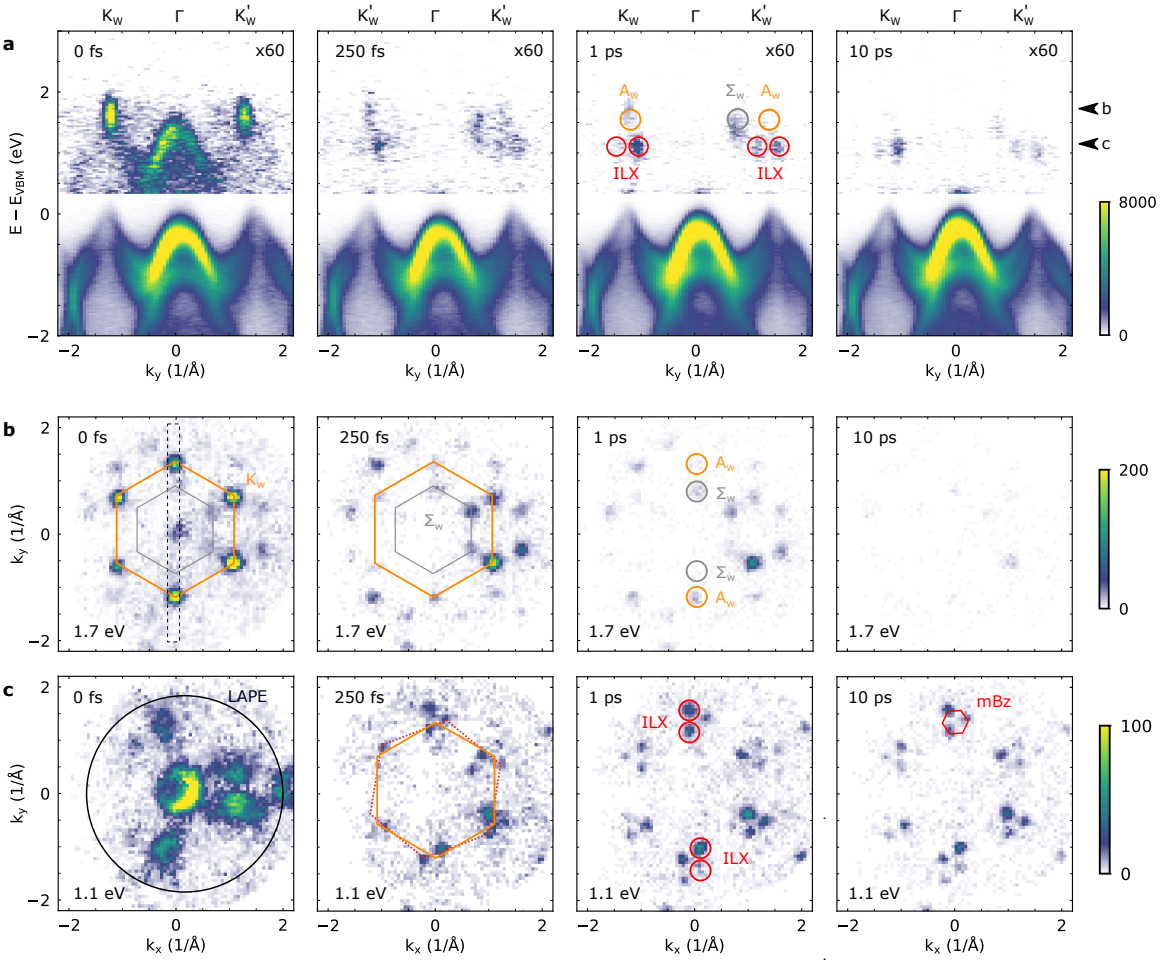

Extended Fig. 3.0.10.: **Additional trARPES data of the ILX formation.** **a** E(k) cut along the K_W-Γ-K'_W-direction integrated in the k-region shown by the black dashed box in **b**, 0 fs. The arrowheads on the right side of the figure indicate the photoelectron energies where the momentum maps in **b** and **c** are centered. **b** Within the energy-window of the k-map (E-E_{VBM} = 1.7 eV) and increasing pump-probe delay, spectral weight from the bright A_W-excitons (orange hexagon) is transferred via exciton-phonon scattering to form dark Σ_W-excitons (grey hexagon). **c** Interlayer tunneling via the Σ-valleys forms the ILX, which is observed at E-E_{VBM} = 1.1 eV. The Brillouin zone of MoS_2 is indicated with a dotted brown hexagon and the mBZ with a red hexagon. Spectroscopic signatures of the A_W-exciton, the Σ_W-exciton, and the ILX are indicated by orange, grey, and red circles, respectively, in the 1 ps data. The pump-probe delay and the binding energy of the k-maps are noted in the top and bottom left corner, respectively. Note that at 0 fs, the strong signal in **c** is mainly caused by LAPE. In addition, in **b** (0 fs), LAPE leads to photoemission yield at the Γ point.

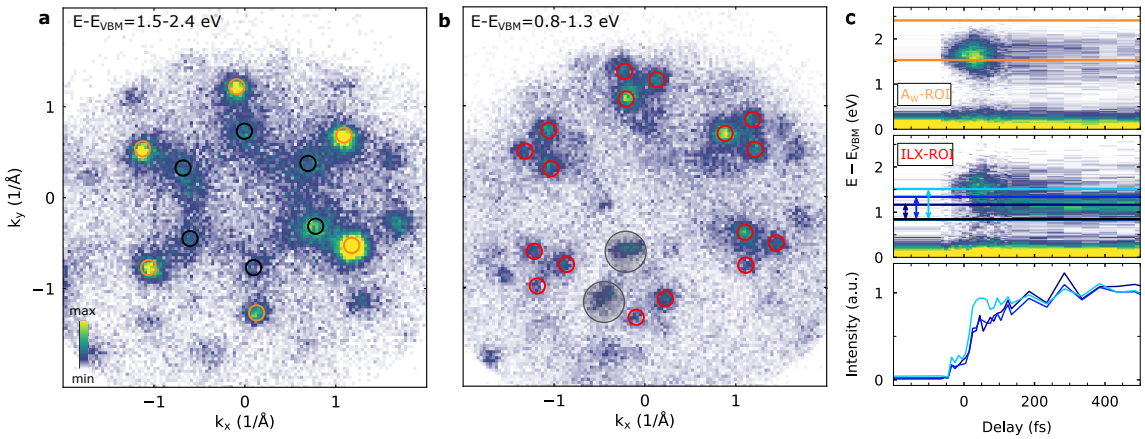

Extended Fig. 3.0.11.: **Selected regions of interest for the analysis of the A_W-, Σ_W-, and ILX formation dynamics shown in Fig. 3.0.2**. **a** and **b** show momentum maps integrated over all measured pump-probe delays in the energy intervals of E-E_{VBM}=1.5-2.4 eV and 0.8-1.3 eV, respectively. The regions-of-interest that are used for filtering the excitonic photoemission signatures in momentum-space are indicated by orange, black, and red circles for the A_W-exciton, the Σ_W-exciton, and the ILX, respectively. The grey shaded areas indicate artefacts of the detector. **c** (top and middle panel) Pump-probe delay evolution of the energy-distribution-curves filtered for the orange and red regions of interest. **c** (bottom panel) Intensity vs. pump-probe delay plots for the energy boxes indicated by the bluish arrows in the middle panel.

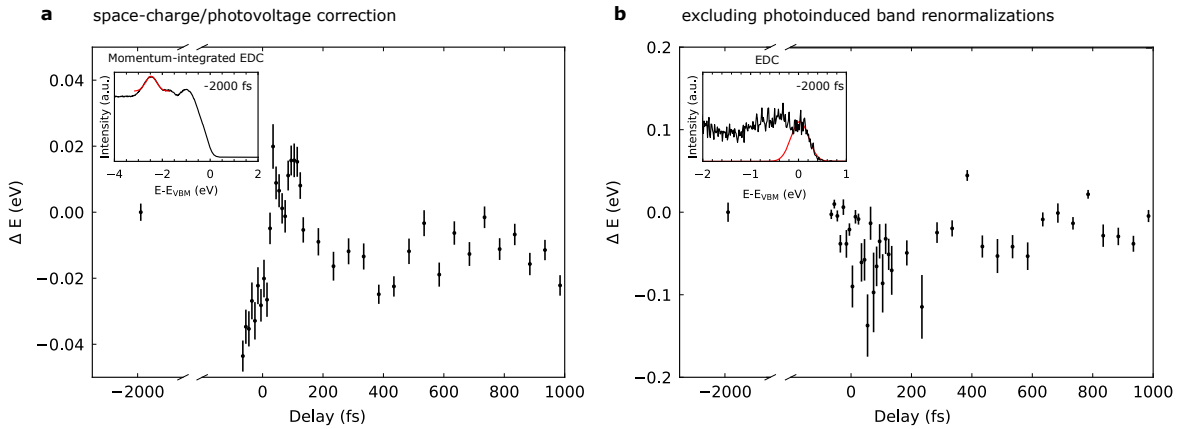

Extended Fig. 3.0.12.: **Correction of space-charge/photovoltage-induced shifts and exclusion of photoinduced band renormalizations.** **a** The rigid band shift ΔE of maximal 70 meV is corrected for each pump-probe delay. ΔE is obtained by fitting (red) momentum integrated energy-distribution-curves (black) for each delay, as exemplary shown for the -2000 fs measurement in the inset. The error bars are standard deviations obtained in each fit. **b** We fit the pump-probe delay dependent energetic peak position of the valence band maximum of WSe_2 at the K_W valley with Gaussian distributions (red, inset) and calculate the energy difference ΔE with respect to the -2000 fs measurement that is plotted in the inset. Within the scattering of the data, ΔE does not upshift with pump-probe delay, excluding a dominant contribution of photoinduced band renormalization such as discussed in refs. [58, 48].

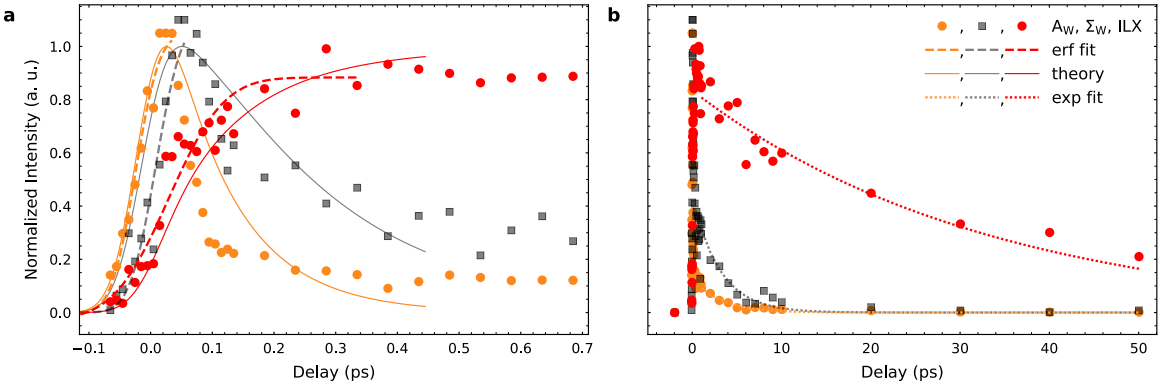

Extended Fig. 3.0.13.: **Charge transfer and charge recombination times of the A_W-exciton (orange), the Σ_W-exciton (grey), and the ILX (red).** **a** The short-time dynamics (symbols) is fitted with error functions (dashed lines), from which the delayed onset times t_i are extracted, as detailed in the text. The solid lines reproduce the model calculations initially shown in Fig. 3.0.2c of the main text. **b** The charge recombination time is extracted by performing single-exponential fits to the data for pump-probe delays larger than 1 ps.

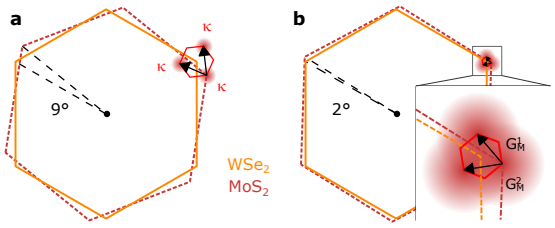

Extended Fig. 3.0.14.: **Sketch of the moiré mBz for small and large twist angles.** The twist angle Θ defines the size of the moiré mBz (red hexagon) and the related moiré reciprocal lattice vectors $G_M^{1,2}$ (black arrows). **a** For twist angles larger than a few degree, $G_M^{1,2}$ is larger than the momentum width of a single κ valley (brownish filled circles). All three κ valleys (and higher order umklapp processes) are detected in the momentum microscopy experiment (Fig. 3.0.3c,d). The electronic contribution to the ILX wavefunction is spread across several moiré potential wells (Fig. 3.0.4). **b** For sufficiently small twist angles, $G_M^{1,2}$ can become smaller than the width of a single κ valley, and the ILX wavefunction can be confined in a single moiré potential well. If the momentum microscopy experiment is performed with a finite momentum-resolution, the photoelectron signal from the ILX can appear as a single peak, as reported in Ref. [101] for a 2° twisted WSe_2/MoS_2 heterostructure.

CHAPTER 4

Ultrafast nano-imaging of dark exciton dynamics

The following article "Ultrafast nano-imaging of dark exciton dynamics" is at the time of the writing process of this thesis in a submission state. Thus, the article version presented in this thesis is not a peer-reviewed manuscript. The presented version of the manuscript is also available in the ArXiv (DOI: 10.48550/arXiv.2305.18908)). Additional to the method part of the presented manuscript, section B.1 will provide additional information on data handling.

Ultrafast nano-imaging of dark exciton dynamics

David Schmitt[1], Jan Philipp Bange[1], Wiebke Bennecke[1], Giuseppe Meneghini[2], AbdulAziz AlMutairi[3], Marco Merboldt[1], Jonas Pöhls[1], Kenji Watanabe[4], Takashi Taniguchi[4], Sabine Steil[1], Daniel Steil[1], R. Thomas Weitz[1,6], Stephan Hofmann[3], Samuel Brem[2], Ermin Malic[2,5], Stefan Mathias[1,6] and Marcel Reutzel[1]

Author contributions

S.S., D.St., R.T.W., S.H., S.B., G.S.M.J., E.M., S.M. and M.R. conceived the research. D.Sch., J.P.B., W.B. and M.M. carried out the time-resolved momentum microscopy experiments. D.Sch. and J.P.B. analyzed the data. G.M. performed the microscopic model calculations. A.A. fabricated the samples. J.P. and D.Sch. performed the AFM measurements. All authors discussed the results. S.M. and M.R. were responsible for the overall project direction and wrote the manuscript with contributions from all co-authors. K.W. and T.T. synthesized the hBN crystals.

[1] I. Physikalisches Institut, Georg-August-Universität Göttingen, Friedrich-Hund-Platz 1, 37077 Göttingen, Germany
[2] Fachbereich Physik, Philipps-Universität, 35032 Marburg, Germany
[3] Department of Engineering, University of Cambridge, Cambridge CB3 0FA, U.K.
[4] International Center for Materials Nanoarchitectonics, National Institute for Materials Science, 1-1 Namiki, Tsukuba 305-0044, Japan
[5] Department of Physics, Chalmers University of Technology, Gothenburg, Sweden
[6] International Center for Advanced Studies of Energy Conversion (ICASEC), University of Göttingen, Göttingen, Germany

Abstract

The role and impact of spatial heterogeneity in two-dimensional quantum materials represents one of the major research quests [20] regarding the future application of these materials in optoelectronics and quantum information science [146, 147, 65]. In the case of transition-metal dichalcogenide heterostructures [3, 87], in particular, direct access to heterogeneities in the dark-exciton landscape [148] with nanometer spatial and ultrafast time resolution is highly desired, but remains largely elusive [18, 19]. Here, we introduce ultrafast dark field momentum microscopy to spatio-temporally resolve dark exciton formation dynamics in a twisted WSe_2/MoS_2 heterostructure with 55 femtosecond time- and 500 nm spatial resolution. This allows us to directly map spatial heterogeneity in the electronic and excitonic structure, and to correlate these with the dark exciton formation and relaxation dynamics. The benefits of simultaneous ultrafast nanoscale dark-field momentum microscopy and spectroscopy is groundbreaking for the present study, and opens the door to new types of experiments with unprecedented spectroscopic and spatiotemporal capabilities.

Direct nanoscale access to the exciton energy landscape and exciton dynamics is at the frontier of two-dimensional quantum materials research. Thinned down to the monolayer limit and stacked to form artificial heterosystems, these materials are highly tuneable and promise the realization of novel optoelectronic devices that can be used in applied [146, 147, 65] and fundamental science [126, 3, 87, 149]. The natural spatio-temporal regime for the quasiparticle dynamics in quantum materials is on the femtosecond-to-picosecond time and nanometer-to-micrometer spatial scale, respectively. In fact, this is the case for any optically-induced and laser-driven process in materials, reaching from direct laser-field manipulations of optically-induced phase transitions to novel transient states of matter [150, 151]. For this reason, a multitude of large scale and laboratory-based research efforts currently aim to develop experiments that can directly access optoelectronics with spatio-temporal and possibly spectroscopic information [152, 153, 154, 155, 18, 100, 156, 157, 158, 19]. In these efforts, however, access to the spatio-temporal dynamics in two-dimensional semiconductors, e.g., transition metal dichalcogenides (TMDs), turns out to be particularly critical and challenging for two reasons: (i) Artificially stacked TMD heterostructures are known to exhibit a significant nanometer-scale heterogeneity [20] which represents a major research obstacle in TMD research with respect to future applications. (ii) The optoelectronic response of these materials is completely driven by Coulomb-correlated electron-hole pairs, i.e., excitons [3]. This strongly involves optically dark excitons [148], and therefore quasiparticles that are for the most part [159] inaccessible using current research approaches.

For the latter challenge, femtosecond momentum microscopy [35, 29], a new variant of time- and angle-resolved photoelectron spectroscopy (trARPES), has just recently been shown to be exceptionally powerful to quantify the dynamics of bright and dark excitons in mono- [24, 25, 69] and twisted bilayer [28, 76, 101, 8] TMDs. As a spatially-integrating method, however, typical trARPES experiments average over sample diameters of 10 μm or more, and are thus blind to nanoscale sample inhomogeneities [160, 20, 18, 100], dielectric disorder [94], regions with strain gradients [161, 154, 162], the presence of correlated phases in the nearest proximity [163] and the local reconstructions of the moiré potential [164, 93, 165]. In

consequence, it is highly desirable to establish ultrafast ARPES on the nanoscale in order to image the energy landscape and dynamics of bright and dark excitons on femtosecond time- and nanometer length scales.

Here, we introduce ultrafast dark-field momentum microscopy as a new technique for simultaneous nano-imaging and nano-spectroscopy of ultrafast dynamics. We showcase the benefits of this technique by elucidating spatio-temporal and spatio-spectral dynamics of bright and dark excitons in a type-II band-aligned WSe_2/MoS_2 heterostructure. We find that this heterostructure, even in seemingly flat areas that exhibit high-quality photoemission spectra, shows distinct spatial heterogeneity. Specifically, we are able to map and correlate the variation of the energy landscape of excitons with its impact on the femtosecond interlayer exciton (ILX) formation dynamics. With many-particle modelling, we elucidate that this correlation is related to nanoscale variations of the strength of interlayer hybridization between the WSe_2 and the MoS_2 layers. Our study sets the stage for the future application of femtosecond dark-field momentum microscopy to the wide class of moiré heterostructures and low-dimensional quantum materials, studying optical excitations and light-induced emergent phenomena on the femtosecond time- and nanometer length scale.

Ultrafast dark-field momentum microscopy of nanoscale exciton dynamics

We start our article with the lateral characterization of the $28.8°\pm0.8°$ twisted WSe_2/MoS_2 heterostructure. Using the real-space mode of the momentum microscope, Fig. 4.0.1b shows the spatial distribution of photoelectrons being emitted from the WSe_2/MoS_2 heterostructure (black polygon). In direct comparison with atomic force microscopy images (AFM, Fig. 4.0.1c and Extended Data Fig. 4.0.7), we find distinct spatial heterogeneity: Beside flat sample areas, significant topographical heights are found that can be attributed to residual gas and hydrocarbons trapped at the interface between both layers ('blisters', exemplary arrows in Fig. 4.0.1b,c). In this inhomogeneous heterostructure, the ultrafast exciton dynamics can be mapped by inserting an aperture into the real-space plane of the momentum microscope to select a region-of-interest on the heterostructure flake (blue circle in Fig. 4.0.1b) [28]. Already, this experimental scheme is extremely powerful in comparison to usual time-resolved ARPES experiments, because we can evaluate the pump-probe delay-dependent photoemission intensity from bright and dark excitons in a diameter of 10 µm. Figure 4.0.1d shows the respective momentum-fingerprints of optically excited A_W-excitons (orange hexagon), the hybrid hΣ-excitons (grey) and the ILXs (black). By evaluating the pump-probe delay dependent photoemission yield from all excitons, consistent with our earlier work on a $9.8\pm0.8°$ twisted heterostructure [28, 8, 166], we find that ILXs in the $28.8°\pm0.8°$ twisted heterosctructure are also formed in a two-step process via interlayer hybridized hΣ-excitons, i.e., via the cascade $A_W \rightarrow h\Sigma \rightarrow ILX$ (Extended Data Fig. 4.0.6). However, we emphasize that this analysis averages over all inhomogeneities within the region-of-interest. Specifically, the

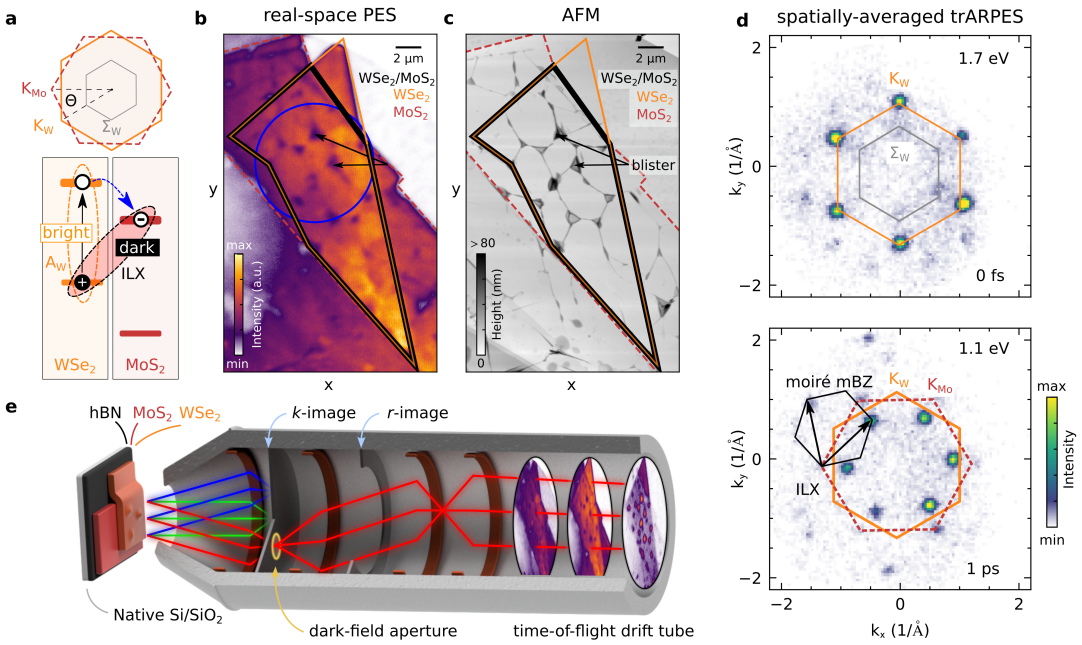

Fig. 4.0.1.: **Real- and momentum-space characterization of the WSe_2/MoS_2 heterostructure and working principle of the ultrafast dark-field momentum microscope. a** Single-particle picture of the type-II band aligned moiré heterostructure. The Brillouin zones of WSe_2 (orange) and MoS_2 (dark-red, dashed) are twisted by $\Theta = 28.8° \pm 0.8°$. Optically excited bright A_W-excitons decay and form optically dark ILX. **b** Real-space resolved photoemission data showing the spatial alignment of the WSe_2 (orange) and MoS_2 (dashed dark-red) monolayers and their region of overlap (black). The black arrows label selected blisters. **c** AFM image of the same sample region. **d** Momentum-resolved photoemission maps from the intralayer A_W-excitons, hybrid $h\Sigma$-excitons and the ILX measured in a spatially-averaged trARPES experiment with an aperture placed into the real-space plane of the momentum microscope (effective diameter of 10 μm, blue circle in **b**). Photoemisison yield is detected at the $K_W^{(\prime)}$ valleys (orange hexagon), the Σ_W valleys (grey), the $K_{Mo}^{(\prime)}$ valleys (dark red dashed) and the high-symmetry points of the moiré mini Brillouin zone (mBZ, black). Additional trARPES data obtained in the spatially averaged mode are shown in Extended Data Fig. 4.0.6. **e** Schematic illustration of the dark-field momentum microscopy experiment. In the electrostatic lens system of the microscope, *k*- and *r*-images are formed in the Fourier and the real-space plane, respectively. The kinetic energy of the photoelectrons is analyzed with a time-of-flight spectrometer. Dark-field momentum microscopy experiments can be performed by placing an aperture into the *k*-image to select a spectroscopic feature of interest (cf. red electron trajectories).

measurement neither excludes the contribution of blister areas, which clearly do not provide a well-defined WSe_2/MoS_2 interface, nor is it sensitive to possible heterogeneity of the energy landscape and dynamics of the excitons in seemingly smooth sample areas.

We overcome this limitation by combining our ultrafast approach with dark-field imaging in the momentum microscope [112] to directly create nanoscale real-space snapshots of the femtosecond exciton dynamics (spatial resolution of 480±80 nm for the used microscope settings, cf. Extended Data Fig. 4.0.12). To do so, a circular aperture is placed in the Fourier plane of the microscope that blocks all photoelectrons except for those emitted in a specific circular momentum range, i.e., with the desired in-plane momenta k_x and k_y, where excitonic photoemission signal emerges (cf. Fig. 4.0.1e; dark-field aperture indicated in inset of Fig. 4.0.2a,b, effective diameter of 0.4 $Å^{-1}$). In this way, we are now able to create spatially-resolved snapshots of the photoelectrons being emitted from bright and dark excitons as a function of pump-probe delay (Supplemental Movies 1 and 2). Figure 4.0.2a shows the real-space formation and relaxation dynamics of the optically excited WSe_2 A_W-exciton at 40 fs, 130 fs and >150 fs delay. Likewise, Fig. 4.0.2b shows the corresponding formation of the dark ILX. At first glance, it is apparent that the exciton dynamics differs in the WSe_2 mono- and the WSe_2/MoS_2 heterobilayer region: Photoemission yield from A_W-excitons is found to be more intense in the WSe_2 monolayer than in the WSe_2/MoS_2 heterobilayer region. Notably, the A_W-exciton photoemission intensity decays significantly faster in the heterobilayer region in comparison to the monolayer region, which is caused by the efficient relaxation channel into the hybrid hΣ-exciton (Fig. 4.0.2a, Extended Data Fig. 6, and ref. [8]). The ILX, on the other hand, are only formed in the region of overlap of the WSe_2 and MoS_2 monolayers. Moreover, it takes more than 200 fs until the photoemission yield of these excitons finally saturates (Fig. 4.0.2b and Extended Data Fig. 4.0.10).

Having recorded such spatio-temporally-resolved data of the bright and dark exciton densities, we can now quantitatively analyze the data for possible heterogeneity in the ILX formation time, which represents spatio-temporal experimental access to dark exciton dynamics that is so far unattainable with any other experimental method. Therefore, we evaluate the pump-probe delay-dependent evolution of the ILX photoemission intensity in a region of the size 1.2×1.2 μm^2. While a certain degree of heterogeneity is to be be expected, we find that, astonishingly, the rise time of the ILX photoemission intensity can vary by more than a factor of 1.7: In the regions indicated by red and blue boxes in Fig. 4.0.2d, the ILX formation time changes from τ_{blue} =115±7 fs to τ_{red} =198±14 fs (Fig. 4.0.2c, error function based fit model described in methods). In order to map the nanoscale heterogeneities in the ILX formation time, we vary the selected region-of-interest pixelwise over the heterobilayer region and plot the formation time τ on a heat-map (Fig. 4.0.2d, relative fit error in Extended Data Fig. 4.0.11). Indeed, this heat-map shows a diverse distribution of the ILX formation time, with a gradient towards faster rise from left to right. Hence, although the spatially-averaged photoelectron spectra indicate a high-quality heterostructure (cf. Extended Data Fig. 4.0.9), the exciton dynamics are strongly affected. Importantly, because we have only evaluated areas that appear smooth in the AFM image (cf. AFM overlay and white areas in Fig. 4.0.2d), we exclude the possibility that blister-regions, where the interface between the WSe_2 and the MoS_2 layer is not well-defined, affect the observed dynamics.

Naturally, the question at hand is the microscopic origin of the spatially distinct ILX formation dynamics. Motivated by the experimental identification that the ILX is formed in a two-step process via layer-hybridized hΣ-excitons (cf. Extended Data Fig. 4.0.6), we make

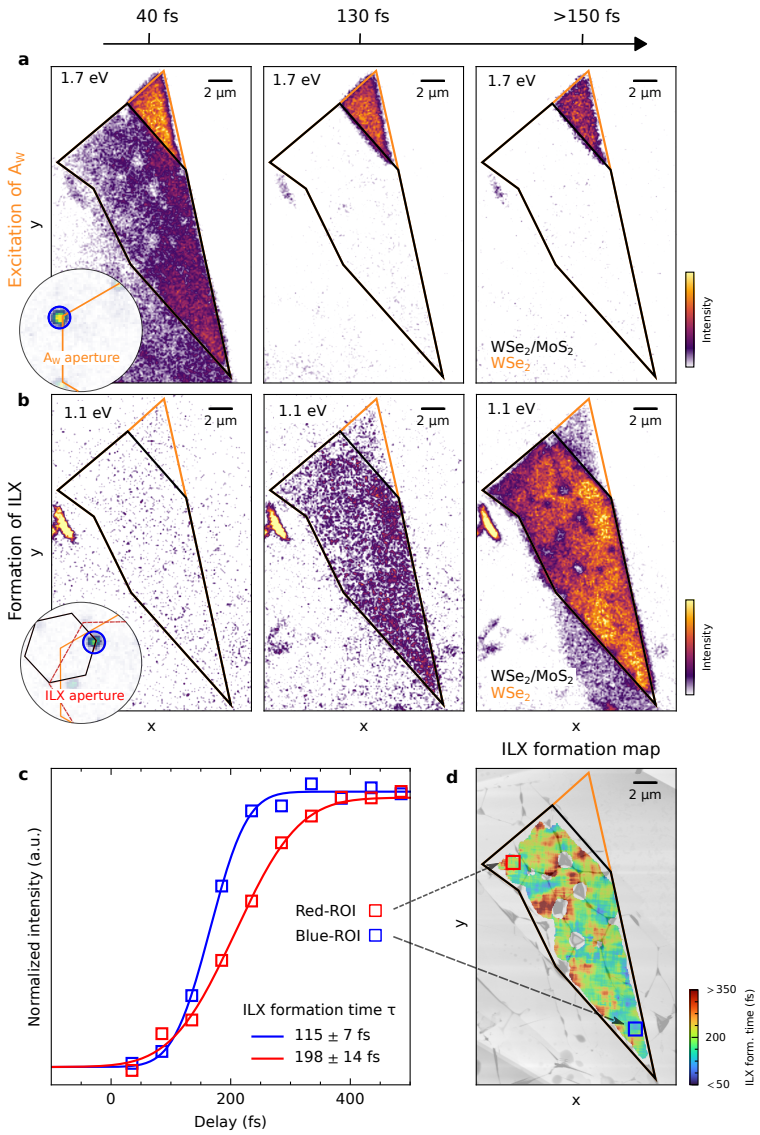

Fig. 4.0.2.: **Spatio-temporal snapshots of the formation and relaxation dynamics of bright A_W-excitons and dark ILXs. a, b** Time- and real-space-resolved snapshots of the dark-field filtered photoemission yield from bright A_W-excitons (**a**) and dark ILXs (**b**). The circular insets show the position of the dark-field aperture (blue circle) in the corresponding momentum-resolved measurement evaluated at the photoemission energies of the A_W-exciton (1.7 eV above WSe_2 VBM) and the ILX (1.1 eV above WSe_2 VBM). **c** Pump-probe delay-dependent evolution of the ILX photoemission intensity evaluated in exemplary regions-of-interest (cf. red and blue squares in **d**). **d** The real-space dependence of the ILX formation time τ is color-coded on a heatmap. τ is only evaluated in regions where the superimposed AFM measurement (grey) shows heights <20 nm.

use of our recently developed microscopic model [28, 166, 167], and search for the key quantities that impact the ILX formation time in the exciton cascade $A_W \rightarrow h\Sigma \rightarrow$ILX (Fig. 4.0.3a).

In order to mimic a spatially inhomogeneous heterostructure with an inherently varying energy landscape [94, 168, 20], we systematically tune the relative energy alignment ΔE_{sp} of the single-particle (sp) valence and conduction bands of WSe_2 and MoS_2, and solve the Wannier equation to calculate the energy landscape of the excitons. For increasing ΔE_{sp}, we find a systematic enhancement of the energies of the hybrid hΣ-exciton and the ILX (Fig. 4.0.3b), and, moreover, a changing degree of hybridization (DoH, c.f. Methods) of the hΣ-exciton (Fig. 4.0.3b). Next, within this energy landscape of excitons, we calculate the formation time of ILX by evaluating the dynamics within the excitonic density matrix formalism. The calculations shown in Fig. 4.0.3c predict that the formation time of the ILX decreases (increases) as the degree of hybridization of the hΣ-exciton is increased (decreased), consistent with earlier reports [166, 6]. Most importantly, this prediction of the microscopic model has a significant implication for the interpretation of the femtosecond dark-field momentum microscopy data: First, the experimentally observed nanoscale variation of the ILX formation is an indication for a changing degree of interlayer hybridization between the WSe_2 and the MoS_2 layers. Second, the model calculations predict a correlation between the ILX formation time and the exciton energies of the hΣ-exciton and the ILX (Fig. 4.0.3c and 4.0.3d, insets). In the following, using the spatio-spectral mode of the dark-field momentum microscopy experiment, we aim to identify this correlation on the WSe_2/MoS_2 heterostructure.

Spatio-spectro-temporal imaging of exciton dynamics

The dark-field aperture inserted in the Fourier plane of the momentum microscope filters a momentum region of 0.4 $\mathrm{Å}^{-1}$ and blocks all remaining photoelectrons. Importantly, it transmits photoelectrons with all accessible kinetic energies within the selected momentum region that can then be analyzed with a time-of-flight spectrometer (cf. Fig. 4.0.1e). In consequence, we can not only monitor the ILX formation time, but also obtain direct spatio-spectroscopic insight to the energy landscape of bright and dark excitons. Figures 4.0.4a,b show such a dark-field-filtered data set that relates the energy-resolved photoemission spectra [i.e., energy-distribution-curves (EDCs)] with the real-space coordinate along the direction of the dashed line in Fig. 4.0.4c (resolution: 480±80 nm). If the dark-field aperture is positioned at the in-plane momentum of the A_W-exciton (Fig. 4.0.4a), the data contains spatio-spectral information of the top and bottom valence bands (VB) of WSe_2 and the A_W-exciton photoemission signal. Intriguingly, even in topographically smooth areas, we find inhomogeneous shifts of the photoemission signatures from the occupied valence bands and the A_W-exciton (EDCs in Fig. 4.0.4a). For example, by plotting the energetic position of the top WSe_2 VB on a heat map, a nanoscale variation of the VB energy by ±0.1 eV can be observed (Fig. 4.0.4c, resolution: 590 nm). We interpret this heterogeneous rigid energy shift as a direct indication for a nanoscale variation of the heterostructure homogeneity that can be attributed to, for example, dielectric disorder [96, 94].

Even more interesting in terms of the optoelectronic response of the sample, our analysis provides unprecedented access to the energy landscape of bright *and* dark excitons: The exciton energies $E_{\mathrm{exc}}^{A_W}$ and E_{exc}^{ILX} of the bright A_W-exciton and the dark ILX can be quantified from the energy difference of the WSe_2 valence band maximum and the respective exciton

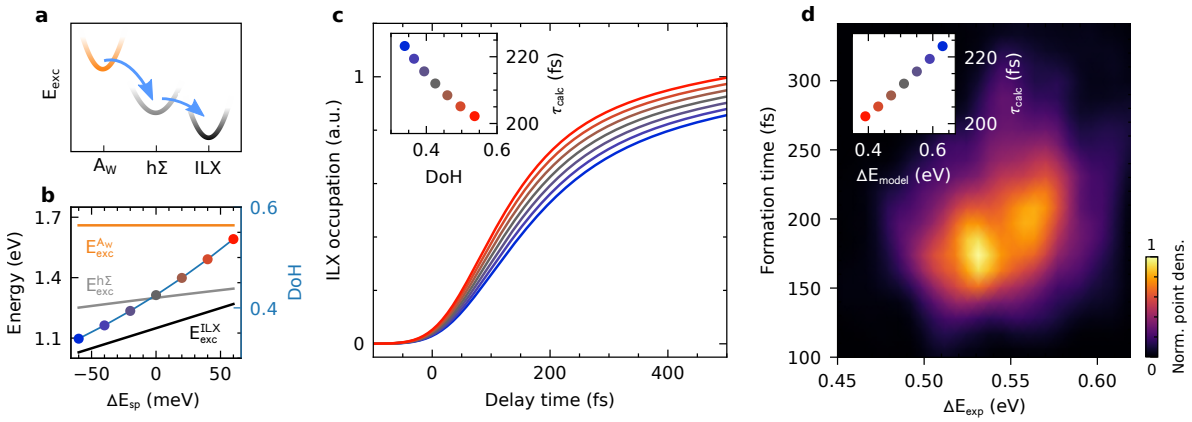

Fig. 4.0.3.: **ILX formation dynamics evaluated with many-particle calculations and correlation of the energy landscape of excitons and ILX formation dynamics. a** The mechanism of the ILX formation process occurs via the cascade $A_W \rightarrow h\Sigma \rightarrow ILX$. **b** In the microscopic model, a spatially inhomogeneous WSe_2/MoS_2 heterostructure and a concomitant varying energy landscape of excitons is mimicked by the systematic variation of the relative band alignment ΔE_{sp} of the single-particle bandstructures of WSe_2 and MoS_2 (cf. Fig. 4.0.1a). The exciton energies E_{exc} of the A_W-exciton, the $h\Sigma$-exciton and the ILX are calculated as a function of ΔE_{sp} by solving the Wannier equation. With increasing ΔE_{sp}, the degree of hybridization (DoH) of the $h\Sigma$-exciton (colored symbols) and the exciton energies of the $h\Sigma$-exciton (grey line) and the ILX (black line) increase. **c** The time-dependent occupation of ILX is calculated by solving the Heisenberg equation of motion for hybrid exciton densities, taking into account the ΔE_{sp} dependent excitonic energies. An increasing degree of hybridisation of the $h\Sigma$-exciton leads to faster ILX formation times τ_{calc} (inset). **d** We observe a correlation between the measured ILX formation time τ and the energy difference $\Delta E_{exp} = E_{exc}^{A_W} - E_{exc}^{ILX}$ (main panel). The theoretical calculation, based on the assumption of a spatially dependent bandstructure alignment, predicts a decreasing formation time τ_{calc} of ILX related to an increase of the hybrid character of the $h\Sigma$-exciton. A change in hybridization can be directly related to the quantity $\Delta E = E_{exc}^{A_W} - E_{exc}^{ILX}$, that can be used in an experiment-theory comparison showing the same qualitative behaviour (inset).

photoemission signal [102, 76, 103] (vertical arrows in Fig. 4.0.4a,b and Methods). In this manner, in Fig. 4.0.4d and 4.0.4e, the nanoscale variation of the energy of the A_W-exciton and the ILX are visualized on a heat map (spatial resolution: 590 nm; error maps in Extended Data Fig. 4.0.11). Notably, we find that the exciton energies vary by ± 0.1 eV with a strong gradient from the left-hand-side to the right-hand-side of the heterostructure (Fig. 4.0.4d,e).

Correlating the spatio-temporal dynamics with the local exciton energy landscape

Finally, we want to show how the measurement approach of the nanoscale spatio-temporal and spatio-spectral exciton dynamics can be used to verify the predictions of our theoretical

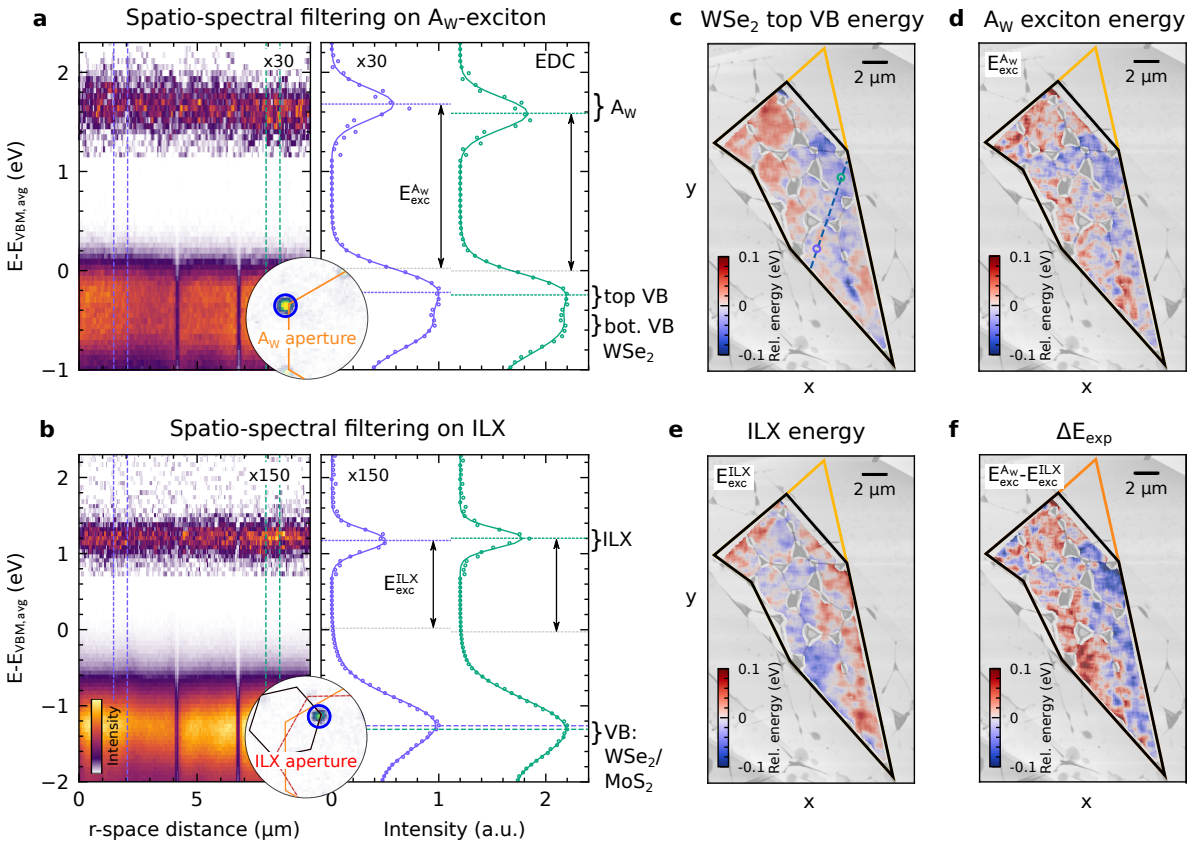

Fig. 4.0.4.: **Spatio-spectral imaging of the energy landscape of bright A_W-excitons and dark ILXs.** **a**,**b** Dark-field filtered photoemission intensity plotted as a function of photoelectron energy and the real-space distance along the blue dashed line in **c**. The data is generated by integrating over all measured pump-probe delays. **a** If the dark-field aperture is positioned on the momenta of the bright A_W-exciton (inset), photoemission yield peaks at the energy of the A_W-exciton (E-$E_{VBM,avg} \approx 1.7$ eV) and the spin-split valence bands of WSe_2 (E-$E_{VBM,avg} \leq 0$ eV). The spatio-spectral variation of the A_W-exciton energy $E^{A_W}_{exc}$ can be read-out from such data by calculating the energy difference between the excitonic photoemission signal and the top WSe_2 valence band (cf. black vertical arrows in the EDCs and Extended Data Fig. 4.0.9). Note that because of the finite width of the dark-field aperture, the energy of the top WSe_2 valence band maxima needs to be corrected by 0.23 eV (cf. grey horizontal line centered at 0 eV and Extended Data Fig. 4.0.9). **b** If the same analysis is performed for the case that the dark-field aperture is positioned on the momenta of the ILX (inset), the spatio-spectral evolution of the exciton energy E^{ILX}_{exc} can be extracted. **c-f** Two-dimensional heatmaps depicting the spatio-spectral variation of the **c** WSe_2 VBM energy, the **d** A_W-exciton energy $E^{A_W}_{exc}$, the **e** ILX energy E^{ILX}_{exc} and the **f** energy difference $\Delta E_{exp} = E^{A_W}_{exc} - E^{ILX}_{exc}$. The energies are evaluated in sample regions with topographical heights <20 nm (cf. superimposed AFM image), and given with respect to their mean value.

modelling. To do so, we generate a correlation map between the nanoscale ILX formation time and exciton energy landscape (Fig. 4.0.3d, main panel). While it would be most

straightforward to correlate the energy of the hybrid hΣ-exciton with the ILX formation time, unfortunately, its photoemission intensity is too weak to be evaluated in a dark-field momentum microscopy experiment (Extended Data Fig. 4.0.6 and Methods). However, we can also focus on the energy separation ΔE_{exp} between the optically-excited A_W-exciton and the ILX (i.e., $\Delta E_{\mathrm{exp}} = E_{\mathrm{exc}}^{\mathrm{A_W}} - E_{\mathrm{exc}}^{\mathrm{ILX}}$, cf. Fig. 4.0.4f). Similar as for the hybrid hΣ-exciton, we expect that an increasing energy separation $\Delta E_{\mathrm{model}} = E_{\mathrm{exc,model}}^{\mathrm{A_W}} - E_{\mathrm{exc,model}}^{\mathrm{ILX}}$ leads to a slower formation time of the ILX (Fig. 4.0.3d, inset). Indeed, the experimental correlation map of these two quantities fully confirms the expectation that the ILX formation time becomes faster with decreasing ΔE_{exp} (Fig. 4.0.3d). Hence, in qualitative agreement between experiment and theory, our analysis demonstrates that the nanoscale heterogeneitiy of the moiré heterostructure leads to distinct ILX formation times, which is dominantly caused by a changing degree of interlayer hybridization between the WSe_2 and the MoS_2 layers.

Discussion

Our work showcases how the femtosecond time-resolved realization of dark-field momentum microscopy enables access to a multitude of spectroscopic signatures with spatio-temporal and spatio-spectral resolution. In our study on a twisted WSe_2/MoS_2 heterostructure, we elucidate that the nanoscale heterogeneity of the heterostructure strongly affects the interlayer hybridization between the WSe_2 and the MoS_2 monolayers, and, accordingly, leads to a renormalization of the energy landscape of excitons and the formation time of ILX. In the future, ultrafast dark-field momentum microscopy will allow direct spatio-spectral and spatio-temporal access to, e.g., diffusion processes [169, 75], new correlated states of matter [163], and the real-space evolution of optically-induced phase transitions [157]. More generally, it opens up unprecedented access to ultrafast quasiparticle dynamics in quantum materials on their fundamental time- and length scales.

ACKNOWLEDGEMENTS

This work was funded by the Deutsche Forschungsgemeinschaft (DFG, German Research Foundation) - 217133147/SFB 1073, projects B07 and B10, 432680300/SFB 1456, project B01 and 223848855/SFB 1083, project B9. A.A. and S.H. acknowledge funding from EPSRC (EP/T001038/1, EP/P005152/1). A.A. acknowledges financial support by the Saudi Arabian Ministry of Higher Education. E. M. acknowledges support from the European Unions Horizon 2020 research and innovation program under grant agreement no. 881603 (Graphene Flagship). K.W. and T.T. acknowledge support from the JSPS KAKENHI (Grant Numbers 20H00354, 21H05233 and 23H02052) and World Premier International Research Center Initiative (WPI), MEXT, Japan.

Methods

Heterostructure fabrication and twist-angle characterization

The WSe_2/MoS_2 heterostructure is fabricated using mechanical exfoliation and dry transfer methods, as detailed in ref. [28]. The heterostructure is stamped on $\approx$ 30 nm hBN [127] on top of a p^+-doped silicon wafer with a native oxide layer. Real-space images of the sample are shown in Fig. 4.0.1b,c of the main text. Before the photoemission experiments, the sample is annealed under ultra-high vacuum conditions to a temperature of 670 K for 1 hour. The twist-angle of the heterostructure is determined to 28.8$\pm$0.8° by direct comparison of the momentum misalignment of the excitonic photoemission signals from WSe_2 and MoS_2 A1s excitons (Extended Data Fig. 4.0.5, cf. analysis in ref. [28]).

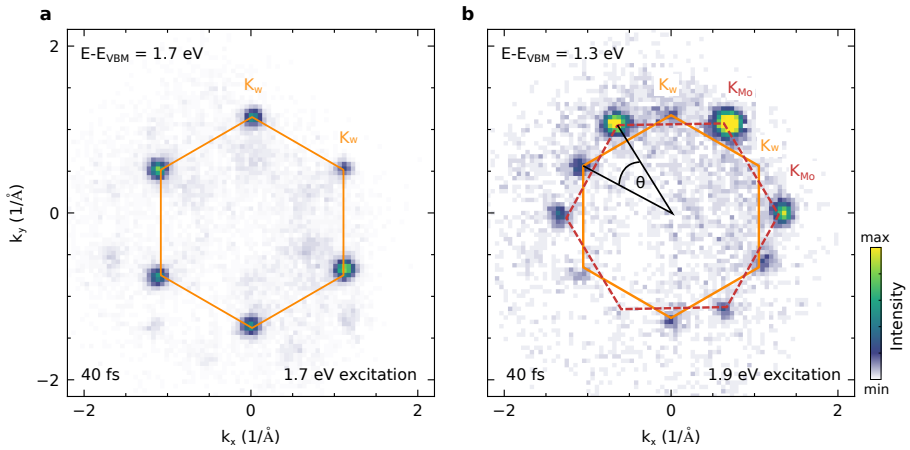

Extended Data Fig. 4.0.5.: **Determination of the twist angle of the WSe_2/MoS_2 heterostructure.** Momentum fingerprints of the WSe_2 A_W-exciton **a** and the MoS_2 A_{Mo}-exciton **b** after photoexcitation with 1.7 eV and 1.9 eV, respectively (pump-probe delay of 40 fs). The Brillouin zones of WSe_2 (orange) and MoS_2 (dark red, dashed) are overlaid onto the data as hexagons. The twist angle θ can be directly determined from the misalignment of the WSe_2 and MoS_2 K valleys (labelled as K_W and K_{Mo}).

ILX formation mechanism: Two-step process via layer hybridized excitons

For the 28.8°± 0.8° twisted WSe_2/MoS_2 heterostructure, the formation mechanism of the ILX is a priori not clear. Because of the large twist angle, an important question is if the ILX formation is still mediated by interlayer hybridized hΣ-excitons, as recently shown for a 9.8±0.8° twisted heterostructure in ref. [28]. In order to address this question, we evaluate the pump-probe delay evolution of all observed excitonic photoemission signals, including the A_W-exciton (orange), the hΣ-exciton (grey) and the ILX (black) (Extended Data Fig.4.0.6). At about 30 fs, we find a peak in the photoemission intensity from optically excited A_W excitons, which is followed by a fast decrease of the signal. During the rise and decrease of the A_W-exciton occupation, spectral yield of the hΣ-exciton builds up (grey symbols). After reaching its maximum at around 50 fs, the signal decreases slowly, and, concomitant, the photoemission yield from the ILX increases and saturates on the 500 fs timescale (black symbols). This hierarchy of timescales was also found in refs. [28, 8] and is consistent with the two-step ILX formation process via hΣ-excitons, i.e., via the cascade $A_W \rightarrow h\Sigma \rightarrow$ILX.

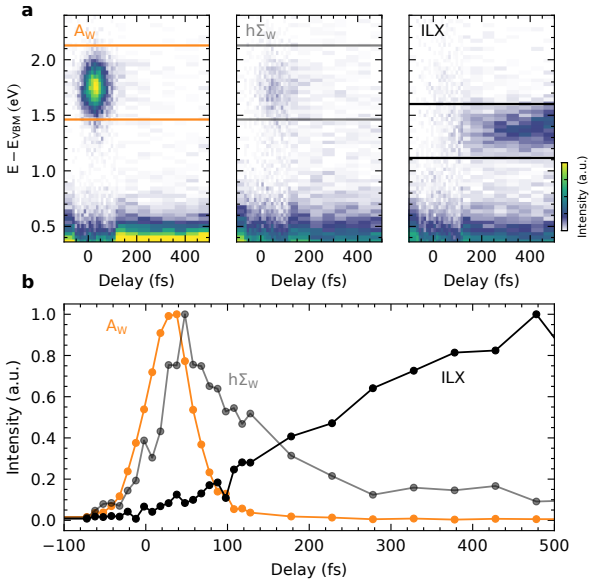

Extended Data Fig. 4.0.6.: **Characterization of the ILX formation mechanism and analysis of the pump-probe-delay-dependent photoemission yield from excitons. a** Pump-probe delay evolution of energy-distribution curves (EDCs) extracted on the momenta of the optically-excited A_W-exciton (left panel), the hybrid hΣ-exciton (middle panel) and the ILX (right panel). **b** By integrating the spectral weight in the energy-windows indicated by the colored rectangles in **a**, the delay-dependent photoemission signal can be directly compared. A temporal hierarchy of photoemission yield from A_W-excitons (orange), hΣ-excitons (grey) and ILX (black) is observed. Note, that panel **a** shows unnormalized EDCs and **b** normalized delay-dependent photoemission signals.

AFM measurements on the WSe_2/MoS_2 heterostructure

AFM measurements are performed to characterize the real-space homogeneity of the WSe_2/MoS_2 heterostructure (Extended Data Fig. 4.0.7). The AFM-image is measured under ambient conditions after the sample has experienced the annealing procedure for the photoemission measurement in ultra-high vacuum conditions. We can clearly resolve the WSe_2 (orange polygon) and MoS_2 (dark red polygon) monolayer regions and their area of overlap. In addition, next to the monolayer flakes, trilayer and bulk regions are found that can be distinguished from the monolayer regions by larger topographic heights. We observe that the heterobilayer region exhibits irregularities with heights up to 100 nm (inset, blue line profile). These areas are identified, for the most part, as residual gas and hydrocarbons being trapped at the interface between the WSe_2 and MoS_2 layers or the MoS_2 and hBN layers. Importantly, in the ultrafast dark-field momentum microscopy experiments, we exclude these blister areas from the analysis (cf. AFM overlays in Fig. 4.0.2 and 4.0.4 of the main text) by removing all regions from the dark-field data with AFM heights larger than 20 nm. Apart from these local areas, the heterobilayer is comparably flat with height differences in the order of 1-2 nm (inset, green line profile).

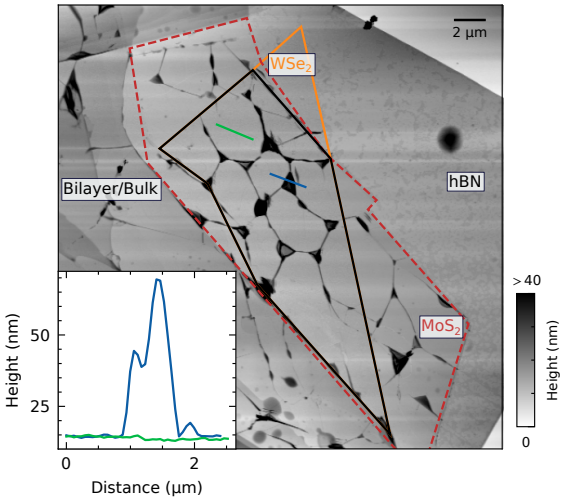

Extended Data Fig. 4.0.7.: **AFM image of the moiré heterostructure**. The WSe_2 and MoS_2 monolayers and the WSe_2/MoS_2 heterostructure are indicated by orange, dark-red (dashed) and black polygons, respectively. In addition, the bulk and the hBN regions are labelled. The inset shows line profiles taken across a blister (blue line) and across a smooth sample area (green line) of the heterostructure.

Experimental setup: ultrafast dark-field momentum microscopy

The dark-field momentum microscopy experiments are performed with a time-of-flight momentum microscope [35] (Surface Concept, ToF-MM) that is operated with a table-top high-repetition rate high-harmonic generation beamline. The beamline is based on a 300 W AFS Fiber laser system and the pump photon energy is tuneable to the bright exciton resonance with an optical parametric amplifier (Orpheus-F/HP from Light Conversion) [29, 128, 50].

All experiments are performed at room temperature with 26.5 eV probe photons (p-polarized, 21±5 fs) and 1.7 eV pump photons (s-polarized, 50±5 fs). The applied pump fluence is 340±20 μJ/cm^{-2} and, following the analysis of ref. [28], the absorbed pump fluence is 1.7±0.3 μJ/cm^{-2} corresponding to an exciton density of (6.5±1.0) × 10^{12} cm^{-2}.

Data handling and image correction

In the dark-field momentum microscopy experiment, we monitor the real-space-resolved exciton dynamics of the A_W-exciton or the ILX by varying the delay between the pump- and the probe laser pulse. As the dark-field aperture blocks a significant amount of photoelectrons, longer integration times are necessary. In the case of the measurement of the ILX dynamics, this implies that we perform overall 23 measurement cycles, whereas, in each cycle, the pump-probe delay is varied between 0 fs and 500 fs in 50 fs steps (10 min integration time per delay step). Overall, this adds up to a measurement duration of 53 h. The overall integration time for the measurement of the A_W-exciton dynamics is 21 h.

Correction of rigid energy-shifts

As typical for measurements on exfoliated TMDs stamped onto Si substrates with a native oxide layer, a pump-probe delay-dependent rigid shift of the full energy spectrum is observed. This rigid energy shift can be attributed to space-charge or surface photovoltage effects [138]. We correct this energy shift for each measurement cycle, as we have detailed in refs. [28, 76].

Correction of rigid real-space shifts

In addition, during the long integration times, rigid shifts of the real-space resolved data can occur due to slight movements of the sample in the momentum microscope. In order to correct for such shifts, we calculate a cross-correlation of each real-space resolved photoelectron image with a reference image. Subsequently, we correct for the rigid real-space shifts before merging the individual data sets.

Correction of image distortions

Momentum microscopy data can be affected by different types of lens errors that can lead to various image distortions such as stretching, shearing or barrel distortions [170, 101].

Moreover, by inserting a contrast-aperture into the Fourier plane of the microscope, off-axis photoelectrons are filtered that are then projected onto the photoelectron detector with an energy-dependent lateral shift. While these distortions can be partly corrected in experiment with magnetic deflectors, further post-processing steps of the measured data are necessary [29, 170]. In conventional momentum-resolved measurements, such corrections are done by a combination of (1) symmetrization of the photoemission signatures (e.g., the known dimension of the Brillouin zone) [171] and/or (2) the symmetrization with a grid which can be placed in the Fourier plane of the objective lens [172, 101].

For the dark-field momentum microscopy experiments, a correction via symmetry-arguments (1) is not possible. A correction by placing a grid in the real-space plane (2) would be possible, but would only correct the lens errors of the projective lens, but not of the objective lens. For our correction procedure, we first (i) correct for the energy-dependent lateral shift and second (ii) use an AFM-image of the heterobilayer sample as a reference image to align the real-space photoelectron images.

First (i), for the correction of the energy-dependent lateral shift, we quantitatively analyze this shift based on a cross-correlation between images at different photoelectron energies. Note that we observe a linear lateral shift for increasing energy, which is then corrected for every image.

The distortion correction (ii) is performed by selecting distinctive points of the heterostructure in the AFM and the photoelectron image (e.g., blisters and edges, Extended Data Fig.4.0.8). Thereafter, we apply an affine transformation that projects the real-space points of the photoelectron image at a certain energy onto respective coordinates extracted from the AFM image; the respective distortion field is visualized in Extended Data Fig. 4.0.8. It is important to note that the energy-dependent shift is corrected before the projection is performed. In that way, the same projection can be applied for each energy in the data set.

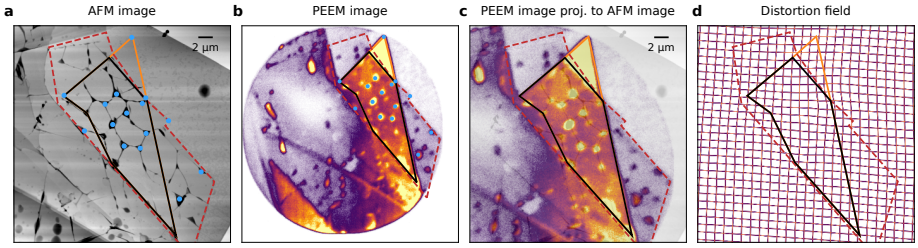

Extended Data Fig. 4.0.8.: **Image correction in dark-field momentum microscopy. a** The WSe_2 (orange) and MoS_2 (dark red, dashed) monolayers and the WSe_2/MoS_2-heterostructure (black) and blisters (blue points) can be identified in the 30 µm×30 µm AFM image. **b** Exemplary real-space image of the full field-of-view measured with the momentum microscope at an energy of $E\text{-}E_{VBM,avg}$ = -0.5 eV. The dark-field aperture is positioned at the in-plane momenta of the ILX. The boundaries of the WSe_2 and MoS_2 monolayers as well as the blister positions are indicated. **c** Based on an affine transformation, the AFM and photoemission images are aligned. **d** Distortion field of the applied transformation.

Calibration of the energy-axis and pump-probe-delay-axis in dark-field momentum microscopy

In addition to the dark-field momentum microscopy experiment, we have performed a typical momentum-resolved photoemission experiment on the WSe_2/MoS_2 heterostructure (cf. Extended Data Fig.4.0.6). We use this spatially averaged trARPES experiment to calibrate the energy- and the pump-probe-delay-axis of the dark-field momentum microscopy experiment.

Energy axis

In most ARPES-related studies on TMDs, the topmost valence-band is set as reference point for the energy axis. For this, the exact position of the VBM must be accessible in experiment. However, this is not straightforwardly realized in dark-field momentum microscopy: The dark-field aperture has an effective diameter of 0.4 Å^{-1} (blue circle in Extended Data Fig.4.0.9a). As such, it integrates over a broad momentum region of the hole-like WSe_2 valence band, and, in consequence, the maximum of the photoemission intensity shifts to smaller energies. This is illustrated in Extended Data Fig.4.0.9a and b where, from typical momentum-resolved measurements, EDCs are evaluated for different apertures sizes, ranging from the original aperture size of dark-field experiment (dark-field apert. size x 1.00 in Extended Data Fig.4.0.9a and b) to roughly 5 times smaller aperture size (dark-field apert. size x 0.21 in Extended Data Fig.4.0.9a and b). From a gaussian peak-fitting procedure, we find an energetic offset of the VBM of 0.23 eV between the respective aperture sizes. In order to provide a meaningful and comparable energy scale in the dark-field momentum microscopy experiment, we shift all data sets with this constant offset. This allows the experiment to provide correct exciton energies that are comparable to other experiments.

Note that the lateral shifts of the energies of the top of the WSe_2 VB as discussed in the main text (Fig. 4.0.4a,c) lead, in principle, to a spatially varying energy scale of the plotted data. In consequence, in Fig. 4.0.4a,b, we plot the data with respect to the spatially averaged VBM, i.e., with respect to $E_{VBM,avg}$.

Alignment of the delay axis for the ILX and the A_W-exciton dark-field momentum microscopy experiment

As the real-space resolved dynamics of the ILX and the A_W-exciton are obtained in separate experiments with long integration times, the pump-probe delay axis of both measurements has to be matched. We do this by directly comparing the dark-field experiments with the spatially averaged trARPES experiment. Therefore, in the spatially averaged trARPES experiment, we evaluate the pump-probe delay-dependent photoemission intensity from the bright A_W-exciton and the ILX as shown in Extended Data 4.0.6 (Extended Data Fig.4.0.9c, grey data points). Importantly, in this analysis, the dynamics of the A_W-exciton and the ILX are measured simultaneously, and, hence, the experiment provides the real delayed onset of the ILX with respect to the A_W exciton. In order to align the delay axis of the ILX and the

A_W-exciton photoemission yield in the dark-field experiment, we spatially integrate photoelectron counts obtained from the ILX (on the heterobilayer region, black squares) and the A_W-exciton (on the heterobilayer region, orange points) and align those with the dynamics in the momentum-resolved trARPES experiment (grey points and squares) in Extended Data Fig.4.0.9c, respectively. Note that this alignment of the pump-probe-delay axis does not impact the quantitative evaluation of the ILX formation time, because here only the formation time is extracted.

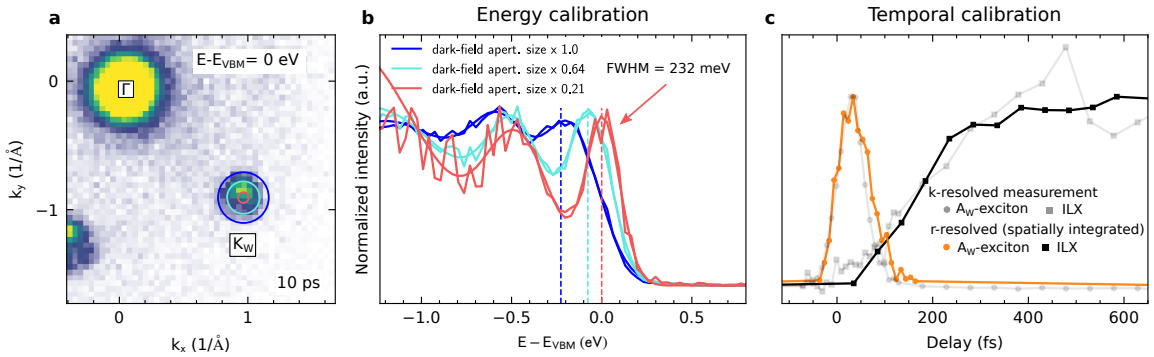

Extended Data Fig. 4.0.9.: **Calibration of the energy- and the pump-probe-delay axis in the dark-field momentum microscopy experiment.** **a** In-plane momentum-resolved photoemission data taken at a pump-probe delay of 10 ps and the energy centered on the WSe_2 VBM. The blue, cyan and red circle indicate different aperture sizes used to create the EDCs in **b**. The size of the dark-field aperture corresponds to the blue circle. **b** EDCs obtained by integrating the photoemission yield in the respective momentum-regions of interest indicated in **a**. In all EDCs, the energetically highest photoemission peak is attributed to the WSe_2 VBM. With increasing diameter of the aperture in momentum space, the peak maxima shift to smaller energies. A quantitative analysis shows an energetic offset of 0.23 eV between the $1\times$ aperture (i.e., the size of the dark-field aperture) and $0.21\times$ aperture. The peak position of the $0.21\times$ aperture is set as reference point and the spatial-resolved data is calibrated with respect to the extracted offset-value. **c** Pump-probe delay-dependent analysis of the photoemission intensity of A_W-excitons and ILXs as extracted in the dark-field experiment (orange and black) and the spatially averaged trARPES experiment (grey).

Additional spatio-temporal snapshots and comparison to the exciton dynamics in the momentum-resolved experiment.

As an extension to Fig. 4.0.2, Extended Data Fig.4.0.10 shows additional spatio-temporal snapshots of the A_W-excitons and the ILX. By spatially integrating over the WSe_2 monolayer region and the WSe_2/MoS_2 heterobilayer region of the A_W signal (orange and black region-of-interest in Extended Data Fig.4.0.10a), we get direct access to the A_W-exciton and ILX dynamics on monolayer WSe_2 and heterobilayer WSe_2/MoS_2 (Extended Data Fig.4.0.10c).

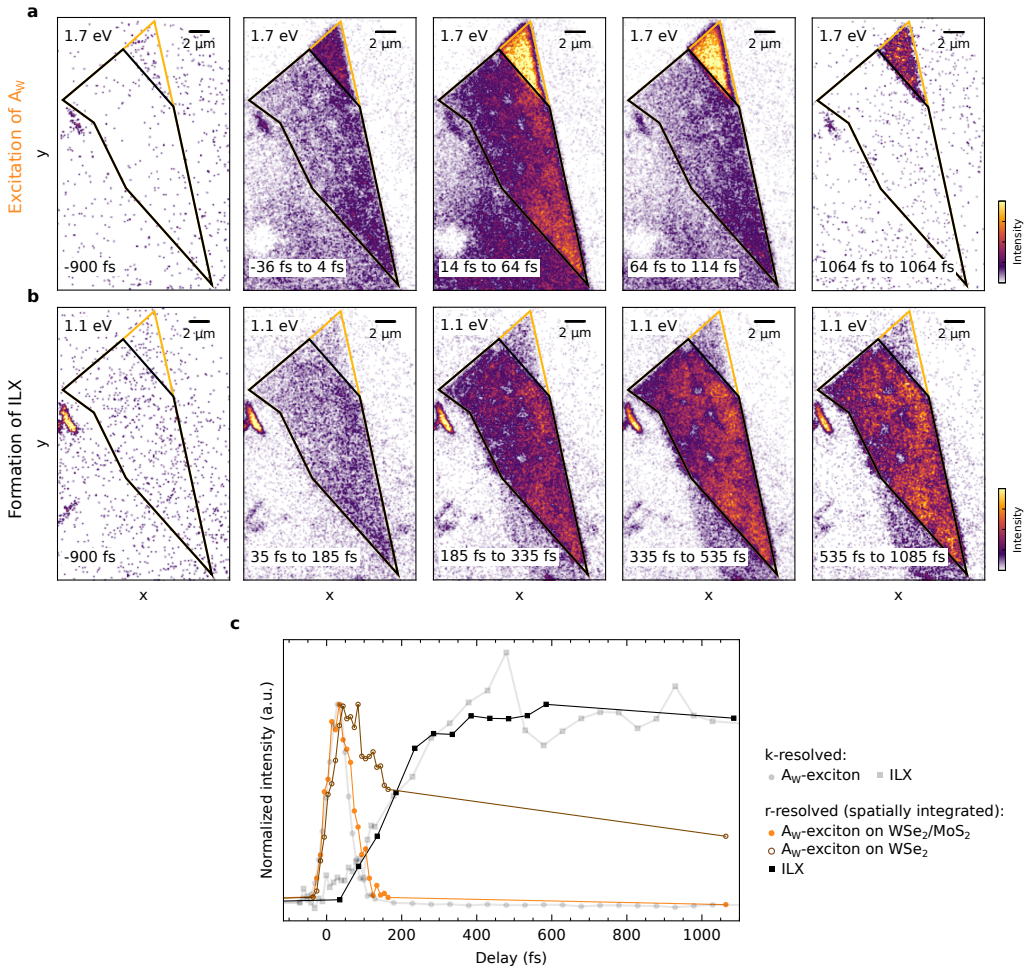

Extended Data Fig. 4.0.10.: **a, b** Real-space snapshots of the formation and relaxation dynamics of bright A_W-excitons (**a**) and ILXs (**b**). **c** Pump-probe delay-dependent analysis of the photoemission yield of the A_W-exciton and the ILX in the WSe_2/MoS_2 heterobilayer (orange and black) and the WSe_2 monolayer (brown). The data points are obtained in the dark-field momentum microscopy experiment by integrating photoelectron counts inside the heterobilayer and monolayer regions. The grey data points are generated from a spatially-averaged trARPES experiment with an aperture positioned in the real-space plane of the microscope (cf. blue circle in Fig. 4.0.1b).

Quantitative analysis of the ILX formation time and the exciton energies

Figures 4.0.2 and 4.0.4 of the main text quantitatively analyze the ILX formation time and the excitonic energy landscape.

Quantitative analysis of the ILX formation time

The rise of photoemission yield of ILX is fitted with error functions of the form

$$I/I_{\max} = 0.5 \cdot \left(\mathrm{erf}\left(\frac{t - t^*}{\sqrt{2}w} \right) + 1 \right), \tag{4.1}$$

where $I/I_{\max}$ describes the photoelectron intensity normalized to the maximum intensity $I_{\max}$, t^* the onset and w the width of the errorfunction. We fit the temporal evolution in the regions-of-interest with this error function and evaluate its full-width at half-maximum value ($w \times 2\sqrt{2\ln 2}$) to quantify the ILX formation time.

Quantitative analysis of the exciton energies

Recent reports have shown that the exciton energy $\mathrm{E}^i_{\mathrm{exc}}$ of bright and dark excitons can be extracted from trARPES experiments by considering the conservation of energy when the Coulomb correlation between the exciton's electron and hole is broken in the photoemission process [102, 76, 103, 173, 71]. This statement is well-described by the relationship

$$E_{\mathrm{elec}} = E_{\mathrm{hole}} + E^i_{\mathrm{exc}} + \hbar\omega, \tag{4.2}$$

which shows that the photoemission energy of the single particle electron $\mathrm{E}_{\mathrm{elec}}$ is detected one exciton energy $\mathrm{E}^i_{\mathrm{exc}}$ above the energy of the single particle hole $\mathrm{E}_{\mathrm{hole}}$ that remains in the sample ($\hbar\omega$: photon energy). When probing photoelectrons from $\mathrm{A_W}$-excitons and the ILXs, the exciton's hole remains in the VBM of WSe_2. Hence, we can extract the spatio-spectral dependence of $\mathrm{A_W}$-excitons and ILXs by fitting the photoemission signals from $\mathrm{A_W}$-excitons, ILX, and the WSe_2 valence bands with Gaussian functions. Subsequently, we calculate the energy difference between the excitonic photoemission signal and the WSe_2 VBM maxima. This is indicated, exemplarily, by the double-headed arrow in the EDCs in Fig. 4.0.4a. Importantly, as discussed in section 4, we correct the extracted energies by a constant energy offset of 0.23 eV because of the momentum-broadening of the EDCs induced by the finite size dark-field aperture.

Real-space resolved heatmaps of the formation time, the energy landscape and the respective absolute errors

In Figs. 4.0.2 and 4.0.4 of the main text, heat-maps that illustrate the formation time of ILX and the electronic and excitonic energy landscape are shown. In Extended Data Fig.4.0.11, the heat-maps are reproduced next to maps that show the spatially resolved absolute errors. For the formation time of ILX, this error is obtained from the fitting of the pump-probe delay-dependent photoemission intensity with equation 4.1. For the energy landscape, the errors are obtained from Gaussian fits to the photoemission feature after the analysis based on equation 4.2.

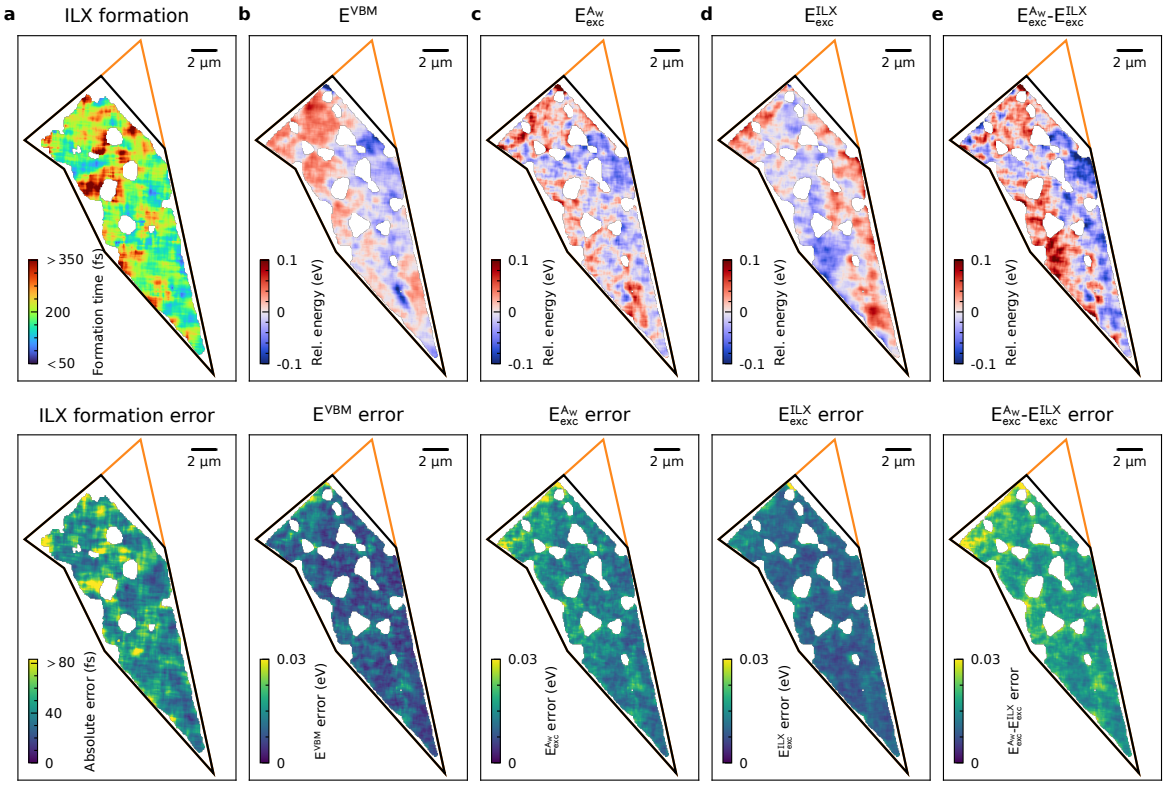

Extended Data Fig. 4.0.11.: **Real-space resolved heatmaps of the formation time, the energy landscape and the respective errors.** **a** ILX formation map and respective absolute errors. **b-e** Spatio-spectral heatmaps (top row) and respective absolute error maps (bottom row)

Spatial resolution of the ultrafast dark-field momentum microscopy experiment

We quantify the real-space resolution of the dark-field momentum microscopy experiment to 472±16 nm (for the used settings). This value is obtained by fitting the change in the photoemission intensity across the lateral interface from bulk hBN to monolayer WSe_2 with an error function (Extended Data Fig.4.0.12a, FWHM). Notably, this spatial-resolution is obtained when the experiment is performed with 26.5 eV photons, the dark-field aperture is positioned on the ILX photoemission signal and photoelectron counts from the occupied valence bands are evaluated in an energy window from 1.69 eV to 1.49 eV. Alternatively, if we directly evaluate photoemission yield from excitons along the same direction on the sample, we find a comparable spatial resolution of 481±79 nm (FWHM) for our settings at a reduced signal-to-noise ratio (Extended Data Fig.4.0.12b). We note that the momentum microscopy instrument itself is in principle capable to achieve a spatial resolution well below 100 nm.

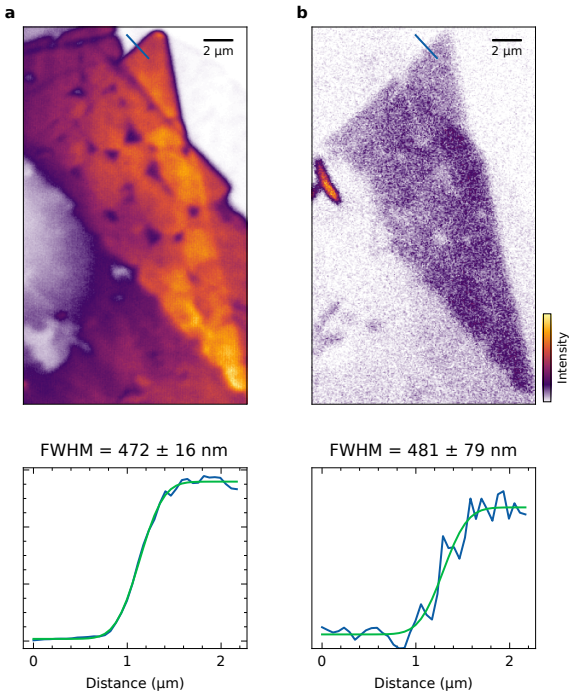

Extended Data Fig. 4.0.12.: **Benchmarking of the real-space resolution of the dark-field momentum microscopy experiment. a** In the momentum microscopy experiment with the dark-field aperture placed on the in-plane momenta of the ILX at an energy range from -1.69 eV to -1.49 eV (occupied valence bands) and a photon energy of 26.5 eV, the spatial resolution is determined to 472±16 nm. **b** If the same analysis is done on the excitonic photoemission yield, i.e., integrated over all energies above 0.6 eV, a spatial resolution of 481±79 nm is extracted. All green lines in the lower panels are error function fits, from which we extract the FWHM has the spatial resolution.

Microscopic modelling

We introduce the main theoretical steps needed in order to access the hybrid exciton dynamics in TMD bilayers. The Hamiltonian of the system can be written as

$$H = H_0 + H_T = \sum_{\mu,\mathbf{Q}} E^{\mu}_{\mathbf{Q}} X^{\mu\dagger}_{\mathbf{Q}} X^{\mu}_{\mathbf{Q}} + \sum_{\mu,\nu,\mathbf{Q}} \mathcal{T}_{\mu\nu} X^{\mu\dagger}_{\mathbf{Q}} X^{\nu}_{\mathbf{Q}} \tag{4.3}$$

whith superindex $\mu = (n^{\mu}, \zeta^{\mu}_e, \zeta^{\mu}_h, L^{\mu}_e, L^{\mu}_h)$ describing the exciton degrees of freedom. Furthermore, $E^{\mu}_{\mathbf{Q}} = E^{c}_{\zeta^{\mu} L^{\mu}_e} - E^{v}_{\zeta^{\mu} L^{\mu}_h} + E^{\mu}_{bind} + E^{\mu}_{\mathbf{Q},kin}$ are the excitonic energies, where E^{μ}_{bind} are obtained after solving a bilayer Wannier equation [174, 7]. Moreover, $E^{c/v}_{\zeta^{\mu} L^{\mu}_e}$ is the conduction and valence band energy and $E^{\mu}_{\mathbf{Q},kin} = \hbar^2\mathbf{Q}^2/(2M^{\mu})$ is the kinetic energy of the exciton with mass $M^{\mu} = (m^{\mu}_e + m^{\mu}_h)$. We address the excitonic tunneling between the TMD monolayers by starting from the electronic tunnelling matrix elements

$$\mathcal{T}_{\mu\nu} = (\delta_{L^{\mu}_h L^{\nu}_h}(1-\delta_{L^{\mu}_e L^{\nu}_e})\delta_{\zeta^{\mu}\zeta^{\nu}} T^{c}_{\mu_e,\nu_e} - \delta_{L^{\mu}_e L^{\nu}_e}(1-\delta_{L^{\mu}_h L^{\nu}_h})\delta_{\zeta^{\mu}\zeta^{\nu}} T^{v}_{\mu_h,\nu_h}) \sum_{\mathbf{k}} \psi^{\mu *}(\mathbf{k})\psi^{\nu}(\mathbf{k}), \tag{4.4}$$

where ψ^{μ} is the excitonic wave function of the state μ defined over the relative momentum between electron and hole. Here, $T^{\lambda}_{ij} = \langle \lambda i\mathbf{p}| H |\lambda j\mathbf{p}\rangle (1-\delta_{L_i L_j})\delta_{\zeta_i\zeta_j}$ denotes the electronic tunneling elements obtained by averaging DFT values of $MoSe_2$-WSe_2 and MoS_2-WS_2 heterostructures in [175]. Diagonalizing Eq. 4.3 leads to a new set of hybrid excitonic energies $\mathscr{E}^{\eta}_{\mathbf{Q}}$ that are obtained by solving the hybrid eigenvalue equation [7, 175],

$$E^{\mu}_{\mathbf{Q}} c^{\eta}_{\mu}(\mathbf{Q}) + \sum_{\nu} \mathcal{T}_{\mu\nu} c^{\eta}_{\nu}(\mathbf{Q}) = \mathscr{E}^{\eta}_{\mathbf{Q}} c^{\eta}_{\mu}(\mathbf{Q}). \tag{4.5}$$

The diagonilized hybrid exciton Hamiltonian reads [166, 28]

$$H = \sum_{\eta} \mathscr{E}^{\eta}_{\mathbf{Q}} Y^{\eta\dagger}_{\mathbf{Q}} Y^{\eta}_{\mathbf{Q}} \tag{4.6}$$

with the hybrid exciton annihilation/creation operators $Y^{\eta(\dagger)}_{\mathbf{Q}} = \sum_{\mu} c^{\eta}_{\mu}(\mathbf{Q}) X^{\mu(\dagger)}_{\mathbf{Q}}$. Using 4.6 we have access to the hybrid exciton energy landscape for the investigated WSe_2-MoS_2 heterostructure.

When treating hybrid states consisting of two main contributions (intra- and interlayer state of one species), and considering that $\left|c^{\eta}_{\mu}(\mathbf{Q})\right|^2$ is related to the percentage of intra- or interlayer character inside the hybrid state, it is useful to define a new quantity called degree of hybridization (DoH)

$$DoH(Q) = 1 - \left| \left|c^{\eta}_{intra}(\mathbf{Q})\right|^2 - \left|c^{\eta}_{inter}(\mathbf{Q})\right|^2 \right| \tag{4.7}$$

The DoH has maximum at 1 when the new state is maximally hybridized (50-50% mixture) between the two starting states, and minimum at 0 in the extreme case of purely in-

tra/interlayer state.

The hybrid exciton-phonon scattering plays a crucial role at the low excitation regime [176, 166]. The corresponding Hamiltonian can be written as [7]

$$H_{Y-ph} = \sum_{j,\mathbf{Q},\mathbf{q},\eta,\xi} \tilde{\mathscr{D}}^{\xi\eta}_{j,\mathbf{q},\mathbf{Q}} Y^{\xi\dagger}_{\mathbf{Q}+\mathbf{q}} Y^{\eta}_{\mathbf{Q}} b_{j,\mathbf{q}} + h.c. \tag{4.8}$$

with the hybrid exciton-phonon coupling $\tilde{\mathscr{D}}^{\xi\eta}_{j,\mathbf{q},\mathbf{Q}}$. The electron-phonon matrix elements, single-particle energies and effective masses are taken from DFT calculations [177]. The excitation of the system through a laser pulse is described semi-classically via the minimal-coupling Hamiltonian that can be written as [7]

$$H_{Y-l} = \sum_{\sigma,\mathbf{Q},\eta} \mathbf{A}\cdot\tilde{\mathscr{M}}^{\eta}_{\sigma\mathbf{Q}} Y^{\eta}_{\mathbf{Q}_{\parallel}} + h.c. \tag{4.9}$$

with hybrid exciton-light coupling $\tilde{\mathscr{M}}^{\eta}_{\sigma\mathbf{Q}}$. Details on the transformation and the definition of the hybrid interaction matrix elements and couplings are given in Ref. [7, 175].

Direct access to the dynamics of the system is obtained by solving the Heisenberg equation of motion for the hybrid occupation $N^{\eta} = \langle Y^{\eta\dagger} Y^{\eta}\rangle$, including $H = H_Y + H_{Y-ph} + H_{Y-l}$, and truncating the Martin-Schwinger hierarchy using a second order Born-Markov approximation [178, 179, 180], separating coherent $P^{\eta}_{\mathbf{Q}} = \langle Y^{\eta\dagger}_{\mathbf{Q}}\rangle$ and incoherent hybrid populations $\delta N^{\eta}_{\mathbf{Q}} = \langle Y^{\eta\dagger}_{\mathbf{Q}} Y^{\eta}_{\mathbf{Q}}\rangle - \langle Y^{\eta\dagger}_{\mathbf{Q}}\rangle\langle Y^{\eta}_{\mathbf{Q}}\rangle = N^{\eta}_{\mathbf{Q}} - |P^{\eta}_{\mathbf{Q}}|^2$. This leads to the following semiconductor Bloch equations

$$\begin{aligned} i\hbar\partial_t P^{\eta}_0 &= -(\mathscr{E}^{\eta}_0 + i\Gamma^{\eta}_0)P^{\eta}_0 - \tilde{\mathscr{M}}^{\eta}_0\cdot\mathbf{A}(t) \\ \delta\dot{N}^{\eta}_{\mathbf{Q}} &= \sum_{\xi} W^{\xi\eta}_{\mathbf{0Q}} |P^{\eta}_0|^2 + \sum_{\xi,\mathbf{Q}'} \left(W^{\xi\eta}_{\mathbf{Q}'\mathbf{Q}} \delta N^{\xi}_{\mathbf{Q}'} - W^{\eta\xi}_{\mathbf{QQ}'} \delta N^{\eta}_{\mathbf{Q}} \right) \end{aligned} \tag{4.10}$$

with $W^{\eta\xi}_{\mathbf{QQ}'} = \frac{2\pi}{\hbar}\sum_{j,\pm} |\mathscr{D}^{\eta\xi}_{j,\mathbf{Q}'-\mathbf{Q}}|^2 \left(\frac{1}{2}\pm\frac{1}{2} + n^{ph}_{j,\mathbf{Q}'-\mathbf{Q}}\right)\delta\left(\mathscr{E}^{\xi}_{\mathbf{Q}'} - \mathscr{E}^{\eta}_{\mathbf{Q}} \mp \hbar\Omega_{j\mathbf{Q}'-\mathbf{Q}}\right)$ as the phonon mediated scattering tensor.

The large twist angle in the experiment gives rise to very short moire periods with a length scale comparable with the exciton Bohr radius. Therefore, a strong modification of the exciton center-of-mass motion, i.e. a moire-trapping of excitons is not expected [10]. Therefore, we neglect the twist angle, aiming to a more qualitative description of the spatial exciton dependence. A spatial change in dynamics as observed in the experiment could be caused by several processes, such as spatially dependent dielectric environment or change in the layer distance. These changes have as common effect that the general energy landscape of the system is strongly modified. This can be included in our model by introducing a spatially dependent relative energy shift ΔE_{sp} between the two layer band structures. Note that we neglect possible changes in the tunnelling strength.

CHAPTER 5

Outlook

In the two publications, the unprecedented access of momentum-resolved and dark-field trMM to the (dark) exciton landscape and dynamics was demonstrated. The momentum-resolved trMM provides access to the electronic and excitonic bandstructure and the respective dynamics of µm-sized samples. The dark-field experiment allows to map momentum-selected regions-of-interest of the electronic (excitonic) band structure to real-space coordinates and enables tracking of the respective dynamics with 500 nm spatial-resolution. In these particular studies, the capabilities of the trMM setup were demonstrated on a twisted WSe_2/MoS_2 heterostructure. Due to the high dimensionality of the datasets and the pristine phenomena observed in this work, the data features much more interesting physics as shown in this thesis and highly motivates further investigation. The first part of the outlook should provide a motivation for the further evaluation of the data sets presented in this thesis and provides ideas for future (complementary) measurements on similar sample structures with different twist angles. In the second part, possible prospective changes of the existing setup are presented that could significantly improve data acquisition and overcome some of the limitations listed in the Appendix A.9.

5.1. Formation of moiré interlayer excitons in space and time

The first article presents a comprehensive study of the (1) unexpected momentum distribution of the interlayer exciton moiré fingerprint, (2) the experimental identification of the interlayer formation process collaborated with microscopic modelling and (3) the reconstruction of the electron contribution of the exciton wave function performed on a 9.8° twisted WSe_2/MoS_2 heterostructure. All these points contain other interesting phenomena that would be interesting to evaluate.

5.1.1. Moiré fingerprint

Moiré fingerprint for different twist angles:
In chapter 3 it has been demonstrated that the distinct intensity distribution of the ILX momentum fingerprint can be constructed with the help of generalized Umklapp processes, where the first order leads to bright intensity spots and the higher order Umklapp processes

lead to much smaller intensities. This approach could be verified on the 9.8° twisted heterostructure, but it should be applicable to all various twist angles. Indeed, performing measurements on the 28.8° [30] and a 5° twisted WSe_2/MoS_2 heterostructure, the ILX intensity distribution in momentum space follows the distinct moiré fingerprint of the respective twist as demonstrated in Fig. 5.1.1 and can be reproduced by the generalized first order Umklapp process.

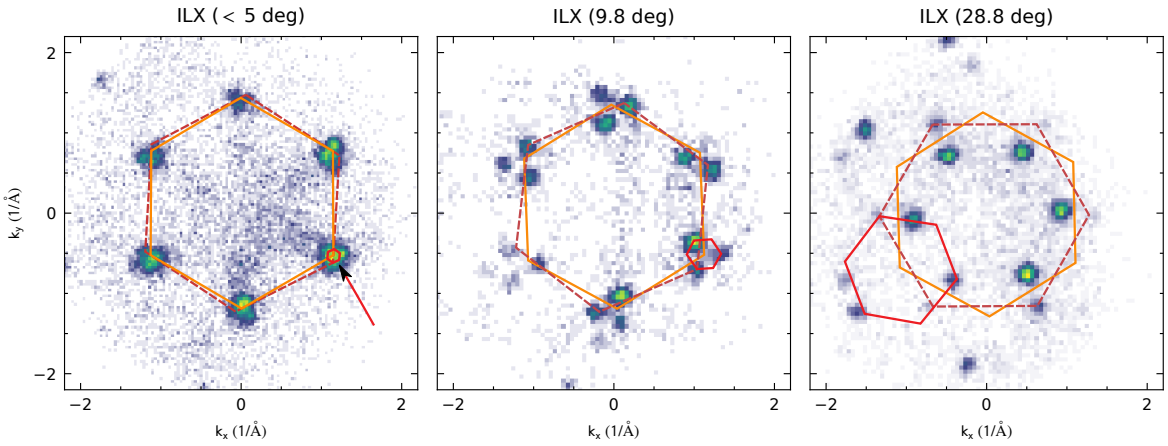

Fig. 5.1.1.: Distinct ILX moiré fingerprint for a <5° a), 9.8° b) and 28.8° c) twisted heterostructure.

For very small twist angles ($\leq 2°$) two effects have to be taken into account. Fig. 3.0.14 in the method part of the first publication (chapter 3), demonstrates that for very small twist angles (2°), the ILX momentum structure cannot be resolved due to the finite momentum resolution of the experiment. In this case, the ILX still has the moiré momentum structure, but it would merge to a single peak observed in the experiment. For such small twist angles, confinement effects of the interlayer exciton's center-of-mass momentum could already affect the momentum distribution. Because of the flat exciton dispersion [10], the interlayer exciton can be distributed over the whole moiré mini Brillouin zone, which results in a broader momentum distribution observed in the experiment [101]. Consequently, the question arises if for small twist angles both effects have to be taken into account, which could strongly affect the interpretation and evaluation of confinement effects measured with the trARPES experiments. Systematic measurements of the interlayer exciton momentum distribution for a series of small twist angles, could provide an answer.

Microscopic origin of the moiré fingerprint:
While the description of the distinct moiré fingerprint is possible by the generalized Umklapp process, the exact microscopic origin is yet unclear. Because the Umklapp process is only observed for the interlayer exciton and not for other exciton species and occupied bands, suggests that the Umklapp process is mediated through the Coulomb interaction between electron and hole in the separated layers. Thus, an open question is the microscopic origin of

the intensity distribution.
From Fig. 5.1.1 it is directly evident that even for the intensity spots described by the first order Umklapp process, a systematic intensity distribution is observed. The intensity of the spots seem to decrease with larger distances in momentum space. This behavior is particularly pronounced for the 28.8° sample, where the inner ILX spots show much larger photoemission intensities than for the ILX intensity found at the K_{Mo} valley. It would be also highly interesting to investigate the observed systematic behavior in detail.

A closer comparison of the ILX moiré fingerprint with the constructed moiré mini Brillouin zone shows that there are small deviations between the intensity distribution and the mBZ. While this behavior could be a residual effect of lens errors, leading to a not-perfectly symmetric alignment of the image, such deviations could be also caused by strain [165]. A quantitative investigation of the deviation could possibly gain access to strain effects.

5.1.2. ILX formation dynamics

The proposed mechanism K→ hΣ →ILX, where the interlayer exciton formation is mediated by the hybrid hΣ-excitons, confirms excellent qualitative agreement with the measured delay-dependent photoemission yield of the respective excitons. Despite the agreement, there are slight deviations between theory and experiment in the decay of the A_W and the build-up of Σ-excitons. The fast decay could hint for additional decay channels that are not yet covered by the microscopic model.

In section 2.3 it was discussed, that in a follow-up publication [8], performed with the same data set presented in this work, the reduced energy of the hybrid hΣ-exciton was confirmed in comparison to the Σ intralayer exciton on a monolayer WSe_2. Additionally, the publication shows that both exciton states are formed by exciton-phonon scattering and that the presence of the energetically lower hΣ-exciton strongly affects the respective exciton dynamics. Also in the second publication of this thesis [30], it could be shown that the hybridization of the hΣ-exciton is the crucial parameter that is responsible for the varying interlayer exciton formation time. The results of both works highly motivates to perform hybridization dependent measurement of the exciton dynamics by, e.g., systematically changing the twist-angle. As a first demonstration, the difference between the 9.8° and 28.8° heterostructure is shown in Fig. 5.1.2. The latter shows a slower formation of the ILX which could be explained by a less hybridized hΣ-exciton, caused by a larger momentum offset between the respective monolayer Σ-valleys.

The exact evaluation and comparison of the energy landscape and possible consequences for the dynamics for the given 5°, 9.8° and 28.8° twisted heterostructures (c.f. Fig. 5.1.1) would reveal further insights of the scattering mechanism for large twist angles, which are usually very difficult to access by experiment and theory. Thus, these measurements would also provide a basis for the theoretical description. On the other hand, also the experimental investigation of very small twist angles, in the presence of moiré- and exciton confinement-

effects could present highly desirable insights into the exact formation mechanism.

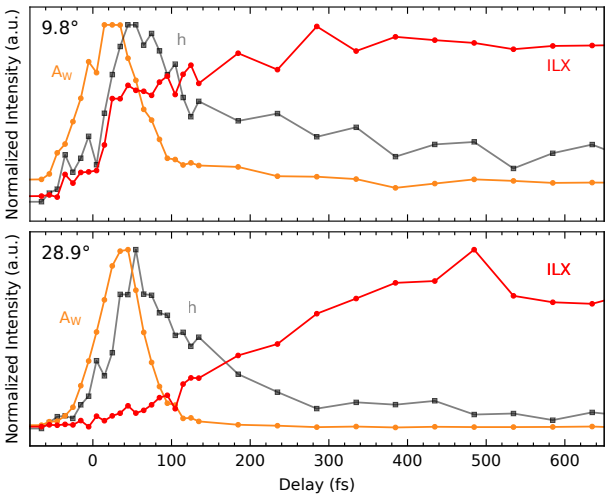

Fig. 5.1.2.: Comparison of the exciton dynamics of the 9.8° a) and 28.8° b) twisted heterostructure, including the A_W, hΣ and the ILX temporal evolution.

5.1.3. Reconstruction of the ILX wave function

The reconstruction of the wavefunction of the electronic contribution of the A_W-exciton and the ILX was successfully performed on the 9.8° twisted heterostructure. As stated in the method part of 3 for twist angles of more than 5° the center-of-mass momentum is assumed to be around zero. For that, the size of the momentum distribution directly relates to the size of the exciton. For smaller twist angles, exciton confinement effects could affect the momentum distribution of the interlayer excitons, leading to a broader momentum distribution. The various phenomena of exciton confinement motivate to investigate heterostructures with small twist angles, as it was demonstrated in reference [101]. However, as stated before, the observed moiré fingerprint and the confinement of center-of-mass momentum of the interlayer exciton can lead to distinct photoemission momentum distributions which can impede the reconstruction of the exciton wavefunction.

5.2. Ultrafast nano-imaging of dark excitons

The second article presents the dark-field momentum microscopy as a new approach to image the exciton landscape and respective dynamics with spectral, spatial and temporal resolution. It has been demonstrated that even in seemingly flat areas the formation of interlayer exciton and the energy landscape can be drastically different. With the help of a microscopic model, the spatially varying ILX formation dynamics could be assigned to a nanoscale variation of the degree of interlayer hybridization. Beside these important observations, the multidimensional data sets include much more quantities which can be evaluated in further detail.

5.2.1. Accessible quantities of the dark-field experiment

Because of the high-dimensionality of the spatio-spectral-temporal data sets, the data accommodates a plethora of potentially valuable information extending the quantities evaluated in the submitted manuscript. The possible quantities, which can be directly extracted as function of spatial coordinates, including also already evaluated quantities, are listed in the following:

(1) A_W photoemission yield,

(2) A_W formation and depletion,

(3) ILX photoemission yield,

(4) ILX formation time,

(5) ILX onset time,

(6) WSe_2 VBM energy,

(7) A_W exciton energy,

(8) ILX exciton energy.

(9) and many more.

The evaluation of these quantities, with regard to possible correlation, might help to find interesting relations that are usually inaccessible by other experimental means.

5.2.2. Direct measurement of the hybridization

The manuscript suggests that the varying ILX formation is a direct consequence of a changing degree of hybridization of the hΣ-exciton, which is correlated with a change of the exciton landscape. However, a more direct evidence would be given if the experiment directly provides the spatio-spectral information of the hΣ-exciton. In the presented study, the intensity of the hΣ-exciton is much smaller than the other exciton states, so that a time-resolved measurement was not feasible at the time. Such measurements would be possible by further changes in the setup, leading to much higher statistics (see next section) or by measuring other twist-angles, where the photoemission yield of hΣ-exciton are more pronounced.

5.2.3. Tracking exciton energies as a function of pump-probe delay

The exciton energies are evaluated by averaging over all measured pump-probe delay times in order to increase the signal-to-noise ratio. The measured data sets also allow to track the respective exciton energies with temporal resolution. In Figure 5.2.1 a), b) the temporal evolution of energy-distribution curves within the ILX aperture of two selected regions-of-interest are shown. In both regions, the ILX photoemission signal is first observed at higher energies and the energies decrease with the pump-probe delay time, whereby the effect seems to be stronger in region B. An evaluation of the energetic position of the interlayer exciton confirms the energy shift of the ILX with increasing pump-probe delay and shows also a stronger effect for region B. This observation could be a sign of a hot interlayer exciton population or a population of higher interlayer exciton states, that thermalizes with increasing pump-probe delay time. The observation could also be a residual effect of blisters (or inhomogeneities), which also lead to a photoemission yield at higher energies present at short pump-probe delay times (see next section). An exact spatial evaluation of the time-dependent evolution of the exciton energies could, e.g., provide additional information about the spatially varying interlayer exciton formation.

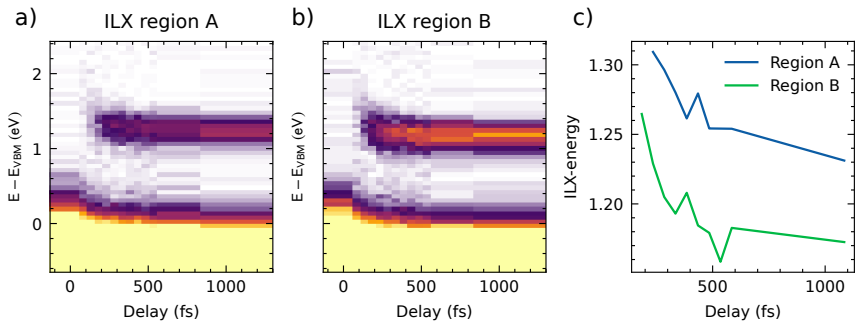

Fig. 5.2.1.: a), b) Temporal evolution of energy-distribution curves extracted for two regions A and B. c) Absolute energy position of the ILX for the respective region A and B as function of pump-probe delay.

5.2.4. Blister analysis

In the main and method part of the manuscript, the 'blister' regions are intentionally removed from the evaluation, because these regions can be strongly affected by strain, dielectric environment, decoupling of the layers and charging effects (see section 2.3). Additionally, due to the topography in the vicinity of the blisters, it is a not clear what kind of momentum space and real-space signature is to be expected from those regions. However, under the assumption that blister regions provide valid photoemission data, the blister regions might show strong influences on the exciton landscape and dynamics, due to the presence of the aforementioned effects. Fig. 5.2.2 a) shows a time-integrated real-space snapshot of the interlayer exciton similar to the snapshots shown in Fig. 4.0.2. It is directly evident, that the photoemission

intensity in the heterobilayer region is not uniformly distributed. Beside the observation of an increasing intensity from left to right, there are regions where almost no ILX signal appears, which can be perfectly matched to the position of blisters observed in the AFM-image. In the time-integrated snapshot, the ILX signal at the blisters seems to suppressed. Surprisingly, photoemission yield at the blister regions is observed for earlier delay times (c.f. Fig. 5.2.2 b)), as demonstrated in an energy-real-space map. The observed blister signal is found energetically above the ILX energies, whereas at the energy of the ILX, the photoemission yield at the blisters is suppressed. For later delay times, the observed photoemission yield at the blisters in the considered energy-window is fully depleted (Fig. 5.2.2 c)). This trend can be confirmed by comparing the time-evolution of the photoemission yield of the ILX to the blister regions in Fig. 5.2.2 d). The photoemission yield at the blisters is present for early pump-probe delays and is rapidly depleted with increasing pump-probe delay, contrary to the ILX photoemission yield, which starts to build up significantly later. A detailed analysis of the observations could be help to identify the presence of one of the aforementioned effects.

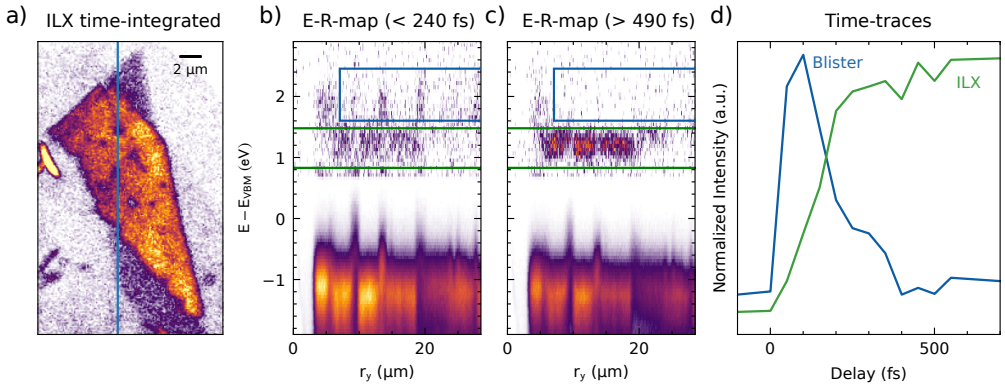

Fig. 5.2.2.: a) Time-integrated real space snapshot of the interlayer exciton. b) Energy-real-space map (E-R-map) for pump-probe delays < 240 fs. The selected cut is indicated in a) by the vertical blue line. c) Same E-R-map for pump-probe delays > 490 fs. d) Comparison of the temporal-evolution of the photoemission yield of the ILX (green) and 'blisters' (blue). The energy-integration windows are indicated in b) and c) as rectangular regions-of-interest.

5.2.5. Measuring the sample quality

In the spatial-averaged ARPES experiments, the energetic linewidth of the bands are typically affected by inhomogeneous broadening caused by the presence of impurities, blisters and the surface potential. The linewidth is typically determined by evaluating the spin-split valence bands of WSe_2 as shown in Fig. A.9.2. In the dark-field ARPES experiment the width of the spin-split of WSe_2 can be extracted and, thus, the sample quality can be monitored spatially, which could provide complementary information for other experiments.

5.3. The trMM setup

In section A.9 the main limitations of the trMM experiment are listed. This section provides suggestions for improvements of the experiment, especially in terms of faster integration times and stable measurement conditions.

Increasing count statistics
The total photoelectron counts of the μARPES experiment are limited by space-charge effects. Because the inserted aperture blocks a large amount of the photoelectrons, the effective count rate is limited to 1-3 $\cdot 10^5$ (see section A.9). The count statistics can be drastically increased if (1) the fluence of the EUV beam is increased and/or (2) the repetition rate of the laser is increased. There are two ways to increase the EUV probe fluence (1), either by increasing the efficiency of the HHG process or by reducing the EUV spot size in the momentum microscope. In the experiment, the former approach does not provide better count statistics because the photoelectron yield already exceeds the space-charge limit significantly and an even larger photoelectron yield leads to space-charge induced blurring and energetically shifts of the ARPES spectra [181]. However, by reducing the EUV spot size, the amount of photoelectrons emitted from the selected region-of-interest increases. In the best case, the spot size is of similar size as the region-of-interest, so that the every photoelectron passes the aperture, yielding a total photoelectron count of about 5 $\cdot 10^5$ with 1 e^-/pulse comparable to the repetition rate of 500 kHz of the laser system. Since the experiment works also way above the 1 e^-/pulse limit, the photoelectron counts could be even further increased. Approaches to decrease the HHG spot sized could include the insertion of a toroidal mirror in front of the sample or a focussing capillary.
The second point concerns the increasing of the repetition rate, which directly leads to higher count statistics. The used fiber laser system allows tuning the repetition rate from 50 kHz to 20 MHz. Notably, applying larger repetition rates at constant average powers reduce the pulse energy, which are required for the nonlinear process and especially the HHG process. However, the extremely high average power of the 300 W laser system should allow to drive these non-linear processes efficiently even for increased repetition-rates.

A combination of the higher fluence and repetition rates would drastically increase the photoelectron counts and would allow an efficient data acquisition below the 1 e^-/pulse limit. The optimization would lower the integration times by an estimated factor of > 10.

Selection of apertures
Due to the fixed geometry of the apertures, the selected region-of-interest does not exactly match the size of the sample. More variability in the apertures sizes would allow the adjustment to the sample size and would increase the total count rate. Especially the dark-field experiment would profit of variable sizes and the possibility to select multiple signatures in momentum space. In the case of the imaging of interlayer exciton, the integration times could be reduced by a factor of 18 (three ILX points for every K-point). Unfortunately, the change of apertures would include the whole detachment of the lens system and the aperture could only be used for the specific sample system.

CHAPTER 6

List of publications

Publications where the author had significantly contributions, which are partly (reference 1: only a few figures) and completely (2,3) integrated in this thesis.

1. M. Keunecke, C. Möller, **D. Schmitt**, H. Nolte, G. S. M. Jansen, M. Reutzel, M. Gutberlet, G. Halasi, D. Steil, S. Steil, and S. Mathias:
   Time-resolved momentum microscopy with a 1 MHz high-harmonic extreme ultraviolet beamline
   Review of Scientific Instruments 91 (6) (2020)
   DOI: 10.1063/5.0006531

2. **D. Schmitt**, J. P. Bange, W. Bennecke, A. AlMutairi, K. Watanabe, T. Taniguchi, D. Steil, D. R. Luke, R. T. Weitz, S. Steil, G. S. M. Jansen, S. Hofmann, M. Reutzel, and S. Mathias:
   Formation of moiré interlayer excitons in space and time
   Nature 608, 499 (2022)
   DOI: 10.1038/s41586-022-04977-7

3. **D. Schmitt**, J. P. Bange, W. Bennecke, G. Meneghini, A. AlMutairi, M. Merboldt, J. Pöhls, K. Watanabe, T. Taniguchi, S. Steil, D. Steil, R. T. Weitz, S. Hofmann, S. Brem, G. S. M. Jansen, E. Malic, S. Mathias, and M. Reutzel
   Ultrafast nano-imaging of dark exciton
   arXiv (2023)
   DOI: 10.48550/arXiv.2305.18908

Other publications, where the author was involved in the experimental measurements, partly in the analysis of the data and partly in the overall discussion.

1. M. Keunecke, M. Reutzel, **D. Schmitt**, A. Osterkorn, T. A. Mishra, C. Möller, W. Bennecke, G. S. M. Jansen, D. Steil, S. R. Manmana, S. Steil, S. Kehrein, and S. Mathias:
   Electromagnetic dressing of the electron energy spectrum of Au(111) at high momenta
   Physical Review B 102.16 (2020): 161403
   DOI: 10.1103/PhysRevB.102.161403

2. M. Keunecke, **D. Schmitt**, M. Reutzel, M. Weber, C. Möller, G. S. M. Jansen, T. A. Mishra, A. Osterkorn, W. Bennecke, K. Pierz, H.W. Schumacher, D.M. Pakdehi, D. Steil, S. R. Manmana, S. Steil, S. Kehrein, H.C. Schneider, and S. Mathias:

Direct Access to Auger Recombination in Graphene
arXiv (2020)
DOI: 10.48550/arXiv.2012.01256

3. G. S. M. Jansen, M. Keunecke, M. Düvel, C. Möller, **D. Schmitt**, W. Bennecke, F. J. S. Kappert, D. Steil, D. R. Luke, S. Steil, and S. Mathias:
Efficient orbital imaging based on ultrafast momentum microscopy and sparsity-driven phase retrieval
New Journal of Physics 22 (6) (2020)
DOI: 10.1088/1367-2630/ab8aae

4. A. Li, M. Reutzel, Z. Wang, **D. Schmitt**, M. Keunecke, W. Bennecke, G. S. M. Jansen, D. Steil, S. Steil, D. Novko, B. Gumhalter, S. Mathias,and H. Petek:
Multidimensional multiphoton momentum microscopy of the anisotropic Ag(110) surface
Phys. Rev. B 105 (Editors' Suggestion), 075105 (2022)
DOI: 10.1103/PhysRevB.105.075105

5. W. Bennecke, A. Windischbacher, **D. Schmitt**, J. P. Bange, R. Hemm, C. S. Kern, G. D'Avino, X. Blase, D. Steil, S. Steil, M. Aeschlimann, B. Stadtmueller, M. Reutzel, P. Puschnig, G.S. Jansen, S. Mathias:
Multiorbital exciton formation in an organic semiconductor
arXiv (2023)
DOI: 10.48550/arXiv.2303.13904

6. J. P. Bange, **D. Schmitt**, W. Bennecke, G. Meneghini, A. AlMutairi, K. Watanabe, T. Taniguchi, D. Steil, S. Steil, R. T. Weitz, G.S. Jansen, S. Hofmann, S. Brem, E. Malic, M. Reutzel, and S. Mathias:
Probing correlations in the exciton landscape of a moiré heterostructure
arXiv (2023)
DOI: 10.48550/arXiv.2303.17886

7. J. P. Bange, P. Werner, **D. Schmitt**, W. Bennecke, G. Meneghini, A. AlMutairi, M. Merboldt, K. Watanabe, T. Taniguchi, S. Steil, D. Steil, R. T. Weitz, S. Hofmann, G.S. Jansen, S. Brem, E. Malic, M. Reutzel, and S. Mathias:
Ultrafast dynamics of bright and dark excitons in monolayer WSe_2 and heterobilayer WSe_2/MoS_2
2D Materials (2023)
DOI: 10.1088/2053-1583/ace067

8. T. Potočnik, O. Burton, M. Reutzel, **D. Schmitt**, J. P. Bange, S. Mathias, F. R. Geisenhof, R. T. Weitz, L. Xin, H. J. Joyce, S. Hofmann, and J. A. Alexander-Webber
   Fast twist angle mapping of bilayer graphene using spectroscopic ellipsometric contrast microscopy
   Nano Letters (2023)
   DOI: 10.1021/acs.nanolett.3c00619

Bibliography

[1] E. C. Regan, D. Wang, E. Y. Paik, Y. Zeng, L. Zhang, J. Zhu, A. H. MacDonald, H. Deng, and F. Wang, "Emerging exciton physics in transition metal dichalcogenide heterobilayers," *Nature Reviews Materials*, vol. 7, no. 10, pp. 778–795, 2022.

[2] N. P. Wilson, W. Yao, J. Shan, and X. Xu, "Excitons and emergent quantum phenomena in stacked 2D semiconductors," *Nature*, vol. 599, no. 7885, pp. 383–392, 2021.

[3] G. Wang, A. Chernikov, M. M. Glazov, T. F. Heinz, X. Marie, T. Amand, and B. Urbaszek, "Colloquium: Excitons in atomically thin transition metal dichalcogenides," *Reviews of Modern Physics*, vol. 90, no. 2, p. 021001, 2018.

[4] A. K. Geim and I. V. Grigorieva, "Van der Waals heterostructures," *Nature*, vol. 499, no. 7459, pp. 419–425, 2013.

[5] Y. Jiang, S. Chen, W. Zheng, B. Zheng, and A. Pan, "Interlayer exciton formation, relaxation, and transport in tmd van der Waals heterostructures," *Light: Science & Applications*, vol. 10, no. 1, p. 72, 2021.

[6] P. Merkl, F. Mooshammer, S. Brem, A. Girnghuber, K.-Q. Lin, L. Weigl, M. Liebich, C.-K. Yong, R. Gillen, J. Maultzsch, J. M. Lupton, E. Malic, and R. Huber, "Twist-tailoring coulomb correlations in van der Waals homobilayers," *Nature Communications*, vol. 11, no. 1, p. 2167, 2020.

[7] S. Brem, K.-Q. Lin, R. Gillen, J. M. Bauer, J. Maultzsch, J. M. Lupton, and E. Malic, "Hybridized intervalley moiré excitons and flat bands in twisted WSe_2 bilayers," *Nanoscale*, vol. 12, no. 20, pp. 11088–11094, 2020.

[8] J. P. Bange, P. Werner, D. Schmitt, W. Bennecke, G. Meneghini, A. AlMutairi, M. Merboldt, K. Watanabe, T. Taniguchi, S. Steil, D. Steil, R. T. Weitz, S. Hofmann, G. S. M. Jansen, S. Brem, E. Malic, M. Reutzel, and S. Mathias, "Ultrafast dynamics of bright and dark excitons in monolayer WSe_2 and heterobilayer WSe_2/MoS_2," *2D Materials*, vol. 10, no. 3, p. 035039, 2023.

[9] K. L. Seyler, P. Rivera, H. Yu, N. P. Wilson, E. L. Ray, D. G. Mandrus, J. Yan, W. Yao, and X. Xu, "Signatures of moiré-trapped valley excitons in $MoSe_2/WSe_2$ heterobilayers," *Nature*, vol. 567, no. 7746, pp. 66–70, 2019.

[10] S. Brem, C. Linderälv, P. Erhart, and E. Malic, "Tunable phases of moiré excitons in van der Waals heterostructures," *Nano letters*, vol. 20, no. 12, pp. 8534–8540, 2020.

[11] Y. Bai, S. Liu, Y. Guo, J. Pack, J. Wang, C. R. Dean, J. Hone, and X.-Y. Zhu,

"Evidence for exciton crystals in a 2D semiconductor heterotrilayer," *arXiv preprint arXiv:2207.09601*, 2022.

[12] A. Chernikov, A. M. van der Zande, H. M. Hill, A. F. Rigosi, A. Velauthapillai, J. Hone, and T. F. Heinz, "Electrical tuning of exciton binding energies in monolayer WS_2," *Physical Review Letters*, vol. 115, no. 12, p. 126802, 2015.

[13] P. Rivera, J. R. Schaibley, A. M. Jones, J. S. Ross, S. Wu, G. Aivazian, P. Klement, K. Seyler, G. Clark, N. J. Ghimire, J. Yan, D. G. Mandrus, W. Yao, and X. Xu, "Observation of long-lived interlayer excitons in monolayer $MoSe_2$–WSe_2 heterostructures," *Nature Communications*, vol. 6, no. 1, p. 6242, 2015.

[14] E. M. Alexeev, D. A. Ruiz-Tijerina, M. Danovich, M. J. Hamer, D. J. Terry, P. K. Nayak, S. Ahn, S. Pak, J. Lee, J. I. Sohn, M. R. Molas, M. Koperski, K. Watanabe, T. Taniguchi, K. S. Novoselov, R. V. Gorbachev, H. S. Shin, V. I. Fal'ko, and A. I. Tartakovskii, "Resonantly hybridized excitons in moiré superlattices in van der Waals heterostructures," *Nature*, vol. 567, no. 7746, pp. 81–86, 2019.

[15] X. Hong, J. Kim, S.-F. Shi, Y. Zhang, C. Jin, Y. Sun, S. Tongay, J. Wu, Y. Zhang, and F. Wang, "Ultrafast charge transfer in atomically thin MoS_2/WS_2 heterostructures," *Nature Nanotechnology*, vol. 9, no. 9, pp. 682–686, 2014.

[16] F. Ceballos, M.-G. Ju, S. D. Lane, X. C. Zeng, and H. Zhao, "Highly efficient and anomalous charge transfer in van der Waals trilayer semiconductors," *Nano letters*, vol. 17, no. 3, pp. 1623–1628, 2017.

[17] J. Choi, M. Florian, A. Steinhoff, D. Erben, K. Tran, D. S. Kim, L. Sun, J. Quan, R. Claassen, S. Majumder, J. A. Hollingsworth, T. Taniguchi, K. Watanabe, K. Ueno, A. Singh, G. Moody, F. Jahnke, and X. Li, "Twist angle-dependent interlayer exciton lifetimes in van der Waals heterostructures," *Phys. Rev. Lett.*, vol. 126, no. 4, p. 047401, 2021.

[18] M. Plankl, P. E. Faria Junior, F. Mooshammer, T. Siday, M. Zizlsperger, F. Sandner, F. Schiegl, S. Maier, M. A. Huber, M. Gmitra, J. Fabian, J. L. Boland, T. L. Cocker, and R. Huber, "Subcycle contact-free nanoscopy of ultrafast interlayer transport in atomically thin heterostructures," *Nature Photonics*, vol. 15, no. 8, pp. 594–600, 2021.

[19] W. Luo, B. G. Whetten, V. Kravtsov, A. Singh, Y. Yang, D. Huang, X. Cheng, T. Jiang, A. Belyanin, and M. B. Raschke, "Ultrafast nanoimaging of electronic coherence of monolayer wse_2," *Nano Letters*, vol. 23, no. 5, pp. 1767–1773, 2023.

[20] D. Rhodes, S. H. Chae, R. Ribeiro-Palau, and J. Hone, "Disorder in van der Waals heterostructures of 2D materials," *Nature Materials*, vol. 18, no. 6, pp. 541–549, 2019.

[21] G. Berghäuser, P. Steinleitner, P. Merkl, R. Huber, A. Knorr, and E. Malic, "Mapping of the dark exciton landscape in transition metal dichalcogenides," *Physical Review B*, vol. 98, no. 2, p. 020301, 2018.

[22] S. Brem, A. Ekman, D. Christiansen, F. Katsch, M. Selig, C. Robert, X. Marie, B. Urbaszek, A. Knorr, and E. Malic, "Phonon-assisted photoluminescence from indirect excitons in monolayers of transition-metal dichalcogenides," *Nano letters*, vol. 20, no. 4, pp. 2849–2856, 2020.

[23] X.-X. Zhang, Y. You, S. Y. F. Zhao, and T. F. Heinz, "Experimental evidence for dark excitons in monolayer WSe_2," *Physical review letters*, vol. 115, no. 25, p. 257403, 2015.

[24] J. Madéo, M. K. L. Man, C. Sahoo, M. Campbell, V. Pareek, E. L. Wong, A. Al-Mahboob, N. S. Chan, A. Karmakar, B. M. K. Mariserla, X. Li, T. F. Heinz, T. Cao, and K. M. Dani, "Directly visualizing the momentum-forbidden dark excitons and their dynamics in atomically thin semiconductors," *Science*, vol. 370, no. 6521, pp. 1199–1204, 2020.

[25] R. Wallauer, R. Perea-Causin, L. Münster, S. Zajusch, S. Brem, J. Güdde, K. Tanimura, K.-Q. Lin, R. Huber, E. Malic, and U. Höfer, "Momentum-resolved observation of exciton formation dynamics in monolayer WS_2," *Nano Letters*, vol. 21, no. 13, pp. 5867–5873, 2021.

[26] M. K. L. Man, J. Madéo, C. Sahoo, K. Xie, M. Campbell, V. Pareek, A. Karmakar, E. L. Wong, A. Al-Mahboob, N. S. Chan, D. R. Bacon, X. Zhu, M. M. M. Abdelrasoul, X. Li, T. F. Heinz, F. H. da Jornada, T. Cao, and K. M. Dani, "Experimental measurement of the intrinsic excitonic wave function," *Science Advances*, vol. 7, no. 17, p. eabg0192, 2021.

[27] S. Dong, M. Puppin, T. Pincelli, S. Beaulieu, D. Christiansen, H. Hübener, C. W. Nicholson, R. P. Xian, M. Dendzik, Y. Deng, Y. W. Windsor, M. Selig, E. Malic, A. Rubio, A. Knorr, M. Wolf, L. Rettig, and R. Ernstorfer, "Direct measurement of key exciton properties: Energy, dynamics, and spatial distribution of the wave function," *Natural Sciences*, vol. 1, no. 1, p. e10010, 2021.

[28] D. Schmitt, J. P. Bange, W. Bennecke, A. AlMutairi, G. Meneghini, K. Watanabe, T. Taniguchi, D. Steil, D. R. Luke, R. T. Weitz, S. Steil, G. S. M. Jansen, S. Brem, E. Malic, S. Hofmann, M. Reutzel, and S. Mathias, "Formation of moiré interlayer excitons in space and time," *Nature*, vol. 608, no. 7923, pp. 499–503, 2022.

[29] M. Keunecke, C. Möller, D. Schmitt, H. Nolte, G. S. M. Jansen, M. Reutzel, M. Gutberlet, G. Halasi, D. Steil, S. Steil, and S. Mathias, "Time-resolved momentum microscopy with a 1 MHz high-harmonic extreme ultraviolet beamline," *Review of Scientific Instruments*, vol. 91, no. 6, p. 063905, 2020.

[30] D. Schmitt, J. P. Bange, W. Bennecke, G. Meneghini, A. AlMutairi, M. Merboldt, J. Pöhls, K. Watanabe, T. Taniguchi, S. Steil, D. Steil, R. T. Weitz, S. Hofmann, S. Brem, G. S. M. Jansen, E. Malic, S. Mathias, and M. Reutzel, "Ultrafast nanoimaging of dark excitons," *arXiv preprint arXiv:2305.18908*, 2023.

[31] S. Hüfner, *Photolectron Spectroscopy - Principles and Applications*. Berlin: Springer, 3rd ed., 2003.

[32] A. Damascelli, Z. Hussain, and Z.-X. Shen, "Angle-resolved photoemission studies of the cuprate superconductors," *Reviews of modern physics*, vol. 75, no. 2, p. 473, 2003.

[33] B. Lv, T. Qian, and H. Ding, "Angle-resolved photoemission spectroscopy and its application to topological materials," *Nature Reviews Physics*, vol. 1, no. 10, pp. 609–626, 2019.

[34] H. Zhang, T. Pincelli, C. Jozwiak, T. Kondo, R. Ernstorfer, T. Sato, and S. Zhou, "Angle-resolved photoemission spectroscopy," *Nature Reviews Methods Primers*, vol. 2, no. 1, p. 54, 2022.

[35] K. Medjanik, O. Fedchenko, S. Chernov, D. Kutnyakhov, M. Ellguth, A. Oelsner, B. Schönhense, T. R. F. Peixoto, P. Lutz, C.-H. Min, F. Reinert, S. Däster, Y. Acremann, J. Viefhaus, W. Wurth, H. J. Elmers, and G. Schönhense, "Direct 3D mapping of the Fermi surface and Fermi velocity," *Nature Materials*, vol. 16, pp. 615–621, June 2017.

[36] Q. Peng, Z. Wang, B. Sa, B. Wu, and Z. Sun, "Electronic structures and enhanced optical properties of blue phosphorene/transition metal dichalcogenides van der Waals heterostructures," *Scientific reports*, vol. 6, no. 1, pp. 1–10, 2016.

[37] H. Lüth, *Solid surfaces, interfaces and thin films*, vol. 4. Springer, 2001.

[38] S. Moser, "A toy model for dichroism in angle resolved photoemission," *Journal of Electron Spectroscopy and Related Phenomena*, vol. 262, p. 147278, 2023.

[39] H. Petek and S. Ogawa, "Femtosecond time-resolved two-photon photoemission studies of electron dynamics in metals," *Progress in surface science*, vol. 56, no. 4, pp. 239–310, 1997.

[40] M. Puppin, C. W. Nicholson, C. Monney, Y. Deng, R. P. Xian, J. Feldl, S. Dong, A. Dominguez, H. Hübener, A. Rubio, M. Wolf, L. Rettig, and R. Ernstorfer, "Excited-state band structure mapping," *Physical Review B*, vol. 105, no. 7, p. 075417, 2022.

[41] H. Soifer, A. Gauthier, A. F. Kemper, C. R. Rotundu, S.-L. Yang, H. Xiong, D. Lu, M. Hashimoto, P. S. Kirchmann, J. A. Sobota, and Z. X. Shen, "Band-resolved imaging of photocurrent in a topological insulator," *Physical Review Letters*, vol. 122, no. 16, p. 167401, 2019.

[42] S. Ulstrup, J. C. Johannsen, A. Crepaldi, F. Cilento, M. Zacchigna, C. Cacho, R. T. Chapman, E. Springate, F. Fromm, C. Raidel, T. Seyller, F. Parmigiani, M. Grioni, and P. Hofmann1, "Ultrafast electron dynamics in epitaxial graphene investigated with time-and angle-resolved photoemission spectroscopy," *Journal of Physics: Condensed Matter*, vol. 27, no. 16, p. 164206, 2015.

[43] I. Gierz, "Probing carrier dynamics in photo-excited graphene with time-resolved arpes," *Journal of Electron Spectroscopy and Related Phenomena*, vol. 219, pp. 53 – 56, 2017. SI: The electronic structure of 2D and layered materials.

[44] T. Rohwer, S. Hellmann, M. Wiesenmayer, C. Sohrt, A. Stange, B. Slomski, A. Carr, Y. Liu, L. M. Avila, M. Kalläne, S. Mathias, L. Kipp, K. Rossnagel, and M. Bauer, "Collapse of long-range charge order tracked by time-resolved photoemission at high momenta," *Nature*, vol. 471, no. 7339, pp. 490–493, 2011.

[45] S. Hellmann, M. Beye, C. Sohrt, T. Rohwer, F. Sorgenfrei, H. Redlin, M. Kalläne, M. Marczynski-Bühlow, F. Hennies, M. Bauer, A. Föhlisch, L. Kipp, W. Wurth, and K. Rossnagel, "Ultrafast melting of a charge-density wave in the mott insulator 1T-TaS_2," *Physical Review Letters*, vol. 105, no. 18, p. 187401, 2010.

[46] P. Majchrzak, K. Volckaert, A. G. Čabo, D. Biswas, M. Bianchi, S. K. Mahatha, M. Dendzik, F. Andreatta, S. S. Grønborg, I. Marković, J. M. Riley, J. C. Johannsen, D. Lizzit, L. Bignardi, S. Lizzit, C. Cacho, O. Alexander, D. Matselyukh, A. S. Wyatt, R. T. Chapman, E. Springate, J. V. Lauritsen, P. D. King, C. E. Sanders, J. A. Miwa, P. Hofmann, and S. Ulstrup, "Spectroscopic view of ultrafast charge carrier dynamics in single-and bilayer transition metal dichalcogenide semiconductors," *Journal of Electron Spectroscopy and Related Phenomena*, vol. 250, p. 147093, 2021.

[47] S. Hellmann, T. Rohwer, M. Kalläne, K. Hanff, C. Sohrt, A. Stange, A. Carr, M. Murnane, H. Kapteyn, L. Kipp, M. Bauer, and K. Rossnagel, "Time-domain classification of charge-density-wave insulators," *Nature communications*, vol. 3, no. 1, p. 1069, 2012.

[48] F. Liu, M. E. Ziffer, K. R. Hansen, J. Wang, and X. Zhu, "Direct Determination of Band-Gap Renormalization in the Photoexcited Monolayer MoS_2," *Physical Review Letters*, vol. 122, no. 24, p. 246803, 2019.

[49] Y. Lin, Y.-h. Chan, W. Lee, L.-S. Lu, Z. Li, W.-H. Chang, C.-K. Shih, R. A. Kaindl, S. G. Louie, and A. Lanzara, "Exciton-driven renormalization of quasiparticle band structure in monolayer MoS_2," *Physical Review B*, vol. 106, no. 8, p. L081117, 2022.

[50] M. Düvel, M. Merboldt, J. P. Bange, H. Strauch, M. Stellbrink, K. Pierz, H. W. Schumacher, D. Momeni, D. Steil, G. S. M. Jansen, S. Steil, D. Novko, S. Mathias, and M. Reutzel, "Far-from-equilibrium electron–phonon interactions in optically excited graphene," *Nano Letters*, vol. 22, no. 12, pp. 4897–4904, 2022.

[51] F. Mahmood, C.-K. Chan, Z. Alpichshev, D. Gardner, Y. Lee, P. A. Lee, and N. Gedik, "Selective scattering between Floquet-Bloch and Volkov states in a topological insulator," *Nature Physics*, vol. 12, no. 4, pp. 306–310, 2016.

[52] Y. H. Wang, H. Steinberg, P. Jarillo-Herrero, and N. Gedik, "Observation of floquet-bloch states on the surface of a topological insulator," *Science*, vol. 342, no. 6157, pp. 453–457, 2013.

[53] S. Zhou, C. Bao, B. Fan, H. Zhou, Q. Gao, H. Zhong, T. Lin, H. Liu, P. Yu, P. Tang, S. Meng, W. Duan, and S. Zhou, "Pseudospin-selective floquet band engineering in black phosphorus," *Nature*, vol. 614, no. 7946, pp. 75–80, 2023.

[54] M. Reutzel, A. Li, Z. Wang, and H. Petek, "Coherent multidimensional photoelectron spectroscopy of ultrafast quasiparticle dressing by light," *Nature Communications*, vol. 11, no. 1, p. 2230, 2020.

[55] M. Keunecke, "Ultrafast electron dynamics measured with a novel time-resolved high-repetition rate momentum microscopy setup," PhD-Thesis, Georg-August-Universität Göttingen, 2021.

[56] M. Keunecke, D. Schmitt, M. Reutzel, M. Weber, C. Möller, G. Jansen, T. A. Mishra, A. Osterkorn, W. Bennecke, K. Pierz, H. W. Schumacher, D. M. Pakdehi, D. Steil, S. R. Manmana, S. Steil, S. Kehrein, H. C. Schneider, and S. Mathias, "Direct access to auger recombination in graphene," *arXiv preprint arXiv:2012.01256*, 2020.

[57] J. M. Riley, F. Mazzola, M. Dendzik, M. Michiardi, T. Takayama, L. Bawden, C. Granerød, M. Leandersson, T. Balasubramanian, M. Hoesch, T. K. Kim, H. Takagi, W. Meevasana, P. Hofmann, M. S. Bahramy, J. W. Wells, and P. D. C. King, "Direct observation of spin-polarized bulk bands in an inversion-symmetric semiconductor," *Nature Physics*, vol. 10, no. 11, pp. 835–839, 2014.

[58] A. Chernikov, C. Ruppert, H. M. Hill, A. F. Rigosi, and T. F. Heinz, "Population inversion and giant bandgap renormalization in atomically thin WS_2 layers," *Nature Photonics*, vol. 9, no. 7, pp. 466–470, 2015.

[59] S. Manzeli, D. Ovchinnikov, D. Pasquier, O. V. Yazyev, and A. Kis, "2D transition metal dichalcogenides," *Nature Reviews Materials*, vol. 2, no. 8, pp. 1–15, 2017.

[60] L. Balents, C. R. Dean, D. K. Efetov, and A. F. Young, "Superconductivity and strong correlations in moiré flat bands," *Nature Physics*, vol. 16, no. 7, pp. 725–733, 2020.

[61] Y. Tang, L. Li, T. Li, Y. Xu, S. Liu, K. Barmak, K. Watanabe, T. Taniguchi, A. H. MacDonald, J. Shan, and K. F. Mak, "Simulation of hubbard model physics in WSe_2/WS_2 moiré superlattices," *Nature*, vol. 579, no. 7799, pp. 353–358, 2020.

[62] K. S. Novoselov, A. Mishchenko, o. A. Carvalho, and A. Castro Neto, "2D materials and van der Waals heterostructures," *Science*, vol. 353, no. 6298, p. aac9439, 2016.

[63] Q. H. Wang, K. Kalantar-Zadeh, A. Kis, J. N. Coleman, and M. S. Strano, "Electronics and optoelectronics of two-dimensional transition metal dichalcogenides," *Nature nanotechnology*, vol. 7, no. 11, pp. 699–712, 2012.

[64] G. Wang, A. Chernikov, M. M. Glazov, T. F. Heinz, X. Marie, T. Amand, and B. Urbaszek, "Colloquium: Excitons in atomically thin transition metal dichalcogenides," *Reviews of Modern Physics*, vol. 90, no. 2, p. 021001, 2018.

[65] T. Mueller and E. Malic, "Exciton physics and device application of two-dimensional transition metal dichalcogenide semiconductors," *npj 2D Materials and Applications*, vol. 2, no. 1, pp. 1–12, 2018.

[66] X. Zhang, X.-F. Qiao, W. Shi, J.-B. Wu, D.-S. Jiang, and P.-H. Tan, "Phonon and raman scattering of two-dimensional transition metal dichalcogenides from monolayer,

multilayer to bulk material," *Chemical Society Reviews*, vol. 44, no. 9, pp. 2757–2785, 2015.

[67] X. Chen, L. Wang, H.-Y. Wang, X.-P. Wang, Y. Luo, and H.-B. Sun, "Electronic structure evolution and exciton energy shifting dynamics in WSe_2: from monolayer to bulk," *Journal of Physics D: Applied Physics*, vol. 54, no. 35, p. 354002, 2021.

[68] R. Bertoni, C. W. Nicholson, L. Waldecker, H. Hübener, C. Monney, U. De Giovannini, M. Puppin, M. Hoesch, E. Springate, R. T. Chapman, C. Cacho, M. Wolf, A. Rubio, and R. Ernstorfer, "Generation and evolution of spin-, valley-, and layer-polarized excited carriers in inversion-symmetric WSe_2," *Physical review letters*, vol. 117, no. 27, p. 277201, 2016.

[69] A. Kunin, S. Chernov, J. Bakalis, Z. Li, S. Cheng, Z. H. Withers, M. G. White, G. Schönhense, X. Du, R. K. Kawakami, and T. K. Allison, "Momentum-resolved exciton coupling and valley polarization dynamics in monolayer WS_2," *Physical Review Letters*, vol. 130, no. 4, p. 046202, 2023.

[70] P. Werner, "Time-resolved momentum-microscopy on a tungsten-diselenide monolayer," bachelor's thesis, Georg-August-Universität Göttingen, 2021.

[71] A. Rustagi and A. F. Kemper, "Photoemission signature of excitons," *Physical Review B*, vol. 97, no. 23, p. 235310, 2018.

[72] H. Yu, Y. Wang, Q. Tong, X. Xu, and W. Yao, "Anomalous Light Cones and Valley Optical Selection Rules of Interlayer Excitons in Twisted Heterobilayers," *Physical Review Letters*, vol. 115, no. 18, p. 187002, 2015.

[73] H. Yu, G.-B. Liu, and W. Yao, "Brightened spin-triplet interlayer excitons and optical selection rules in van der Waals heterobilayers," *2D Materials*, vol. 5, no. 3, p. 035021, 2018.

[74] M. Selig, G. Berghäuser, A. Raja, P. Nagler, C. Schüller, T. F. Heinz, T. Korn, A. Chernikov, E. Malic, and A. Knorr, "Excitonic linewidth and coherence lifetime in monolayer transition metal dichalcogenides," *Nature communications*, vol. 7, no. 1, p. 13279, 2016.

[75] R. Rosati, R. Schmidt, S. Brem, R. Perea-Causín, I. Niehues, J. Kern, J. A. Preuß, R. Schneider, S. Michaelis de Vasconcellos, R. Bratschitsch, and E. Malic, "Dark exciton anti-funneling in atomically thin semiconductors," *Nature Communications*, vol. 12, no. 1, p. 7221, 2021.

[76] J. P. Bange, D. Schmitt, W. Bennecke, G. Meneghini, A. AlMutairi, K. Watanabe, T. Taniguchi, D. Steil, S. Steil, R. T. Weitz, G. S. Matthijs Jansen, S. Hofmann, S. Brem, E. Malic, M. Reutzel, and S. Mathias, "Probing correlations in the exciton landscape of a moiré heterostructure," *arXiv e-prints*, p. arXiv:2303.17886, Mar. 2023.

[77] P. Merkl, F. Mooshammer, P. Steinleitner, A. Girnghuber, K. Q. Lin, P. Nagler,

J. Holler, C. Schüller, J. M. Lupton, T. Korn, S. Ovesen, S. Brem, E. Malic, and R. Huber, "Ultrafast transition between exciton phases in van der Waals heterostructures," *Nature Materials*, vol. 18, no. 7, pp. 691–696, 2019.

[78] C. Jiang, W. Xu, A. Rasmita, Z. Huang, K. Li, Q. Xiong, and W.-b. Gao, "Microsecond dark-exciton valley polarization memory in two-dimensional heterostructures," *Nature communications*, vol. 9, no. 1, p. 753, 2018.

[79] J. Kunstmann, F. Mooshammer, P. Nagler, A. Chaves, F. Stein, N. Paradiso, G. Plechinger, C. Strunk, C. Schüller, G. Seifert, D. R. Reichman, and T. Korn, "Momentum-space indirect interlayer excitons in transition-metal dichalcogenide van der Waals heterostructures," *Nature Physics*, vol. 14, no. 8, pp. 801–805, 2018.

[80] L. Zhang, Z. Zhang, F. Wu, D. Wang, R. Gogna, S. Hou, K. Watanabe, T. Taniguchi, K. Kulkarni, T. Kuo, S. R. Forrest, and H. Deng, "Twist-angle dependence of moiré excitons in WS_2/$MoSe_2$ heterobilayers," *Nature communications*, vol. 11, no. 1, p. 5888, 2020.

[81] A. Ciarrocchi, F. Tagarelli, A. Avsar, and A. Kis, "Excitonic devices with van der Waals heterostructures: valleytronics meets twistronics," *Nature Reviews Materials*, vol. 7, no. 6, pp. 449–464, 2022.

[82] H. Yu, G.-B. Liu, J. Tang, X. Xu, and W. Yao, "Moiré excitons: From programmable quantum emitter arrays to spin-orbit–coupled artificial lattices," *Science advances*, vol. 3, no. 11, p. e1701696, 2017.

[83] D. Huang, J. Choi, C.-K. Shih, and X. Li, "Excitons in semiconductor moiré superlattices," *Nature Nanotechnology*, vol. 17, no. 3, pp. 227–238, 2022.

[84] R. Perea-Causin, D. Erkensten, J. M. Fitzgerald, J. J. Thompson, R. Rosati, S. Brem, and E. Malic, "Exciton optics, dynamics, and transport in atomically thin semiconductors," *APL Materials*, vol. 10, no. 10, p. 100701, 2022.

[85] M. Selig, G. Berghäuser, M. Richter, R. Bratschitsch, A. Knorr, and E. Malic, "Dark and bright exciton formation, thermalization, and photoluminescence in monolayer transition metal dichalcogenides," *2D Materials*, vol. 5, no. 3, p. 035017, 2018.

[86] C. Trovatello, F. Katsch, N. J. Borys, M. Selig, K. Yao, R. Borrego-Varillas, F. Scotognella, I. Kriegel, A. Yan, A. Zettl, P. J. Schuck, A. Knorr, G. Cerullo, and S. Dal Conte, "The ultrafast onset of exciton formation in 2D semiconductors," *Nature communications*, vol. 11, no. 1, p. 5277, 2020.

[87] C. Jin, E. Y. Ma, O. Karni, E. C. Regan, F. Wang, and T. F. Heinz, "Ultrafast dynamics in van der Waals heterostructures," *Nature Nanotechnology*, vol. 13, no. 11, pp. 994–1003, 2018.

[88] H. Zhu, J. Wang, Z. Gong, Y. D. Kim, J. Hone, and X. Y. Zhu, "Interfacial charge transfer circumventing momentum mismatch at two-dimensional van der Waals heterojunctions," *Nano Letters*, vol. 17, no. 6, pp. 3591–3598, 2017.

[89] J. E. Zimmermann, M. Axt, F. Mooshammer, P. Nagler, C. Schüller, T. Korn, U. Höfer, and G. Mette, "Ultrafast Charge-Transfer Dynamics in Twisted MoS_2/WSe_2 Heterostructures," *ACS Nano*, vol. 15, no. 9, pp. 14725–14731, 2021.

[90] Y. Li, Q. Cui, F. Ceballos, S. D. Lane, Z. Qi, and H. Zhao, "Ultrafast interlayer electron transfer in incommensurate transition metal dichalcogenide homobilayers," *Nano Letters*, vol. 17, no. 11, pp. 6661–6666, 2017.

[91] D. G. Purdie, N. Pugno, T. Taniguchi, K. Watanabe, A. Ferrari, and A. Lombardo, "Cleaning interfaces in layered materials heterostructures," *Nature communications*, vol. 9, no. 1, p. 5387, 2018.

[92] A. Rodriguez, M. Kalbáč, and O. Frank, "Strong localization effects in the photoluminescence of transition metal dichalcogenide heterobilayers," *2D Materials*, vol. 8, no. 2, p. 025028, 2021.

[93] T. A. de Jong, T. Benschop, X. Chen, E. E. Krasovskii, M. J. A. de Dood, R. M. Tromp, M. P. Allan, and S. J. van der Molen, "Imaging moiré deformation and dynamics in twisted bilayer graphene," *Nature Communications*, vol. 13, no. 1, p. 70, 2022.

[94] A. Raja, L. Waldecker, J. Zipfel, Y. Cho, S. Brem, J. D. Ziegler, M. Kulig, T. Taniguchi, K. Watanabe, E. Malic, T. F. Heinz, T. C. Berkelbach, and A. Chernikov, "Dielectric disorder in two-dimensional materials," *Nature Nanotechnology*, vol. 14, no. 9, pp. 832–837, 2019.

[95] C. Steinke, T. O. Wehling, and M. Rösner, "Coulomb-engineered heterojunctions and dynamical screening in transition metal dichalcogenide monolayers," *Physical Review B*, vol. 102, no. 11, p. 115111, 2020.

[96] L. Waldecker, A. Raja, M. Rösner, C. Steinke, A. Bostwick, R. J. Koch, C. Jozwiak, T. Taniguchi, K. Watanabe, E. Rotenberg, T. O. Wehling, and T. F. Heinz, "Rigid band shifts in two-dimensional semiconductors through external dielectric screening," *Physical Review Letters*, vol. 123, no. 20, p. 206403, 2019.

[97] Z. Khatibi, M. Feierabend, M. Selig, S. Brem, C. Linderälv, P. Erhart, and E. Malic, "Impact of strain on the excitonic linewidth in transition metal dichalcogenides," *2D Materials*, vol. 6, no. 1, p. 015015, 2018.

[98] S. B. Desai, G. Seol, J. S. Kang, H. Fang, C. Battaglia, R. Kapadia, J. W. Ager, J. Guo, and A. Javey, "Strain-induced indirect to direct bandgap transition in multilayer WSe_2," *Nano letters*, vol. 14, no. 8, pp. 4592–4597, 2014.

[99] S. Ulstrup, R. J. Koch, D. Schwarz, K. M. McCreary, B. T. Jonker, S. Singh, A. Bostwick, E. Rotenberg, C. Jozwiak, and J. Katoch, "Imaging microscopic electronic contrasts at the interface of single-layer WS_2 with oxide and boron nitride substrates," *Applied Physics Letters*, vol. 114, no. 15, p. 151601, 2019.

[100] T. L. Purz, E. W. Martin, W. G. Holtzmann, P. Rivera, A. Alfrey, K. M. Bates, H. Deng, X. Xu, and S. T. Cundiff, "Imaging dynamic exciton interactions and coupling in

transition metal dichalcogenides," *The Journal of Chemical Physics*, vol. 156, no. 21, p. 214704, 2022.

[101] O. Karni, E. Barré, V. Pareek, J. D. Georgaras, M. K. L. Man, C. Sahoo, D. R. Bacon, X. Zhu, H. B. Ribeiro, A. L. O'Beirne, J. Hu, A. Al-Mahboob, M. M. M. Abdelrasoul, N. S. Chan, A. Karmakar, A. J. Winchester, B. Kim, K. Watanabe, T. Taniguchi, K. Barmak, J. Madéo, F. H. da Jornada, T. F. Heinz, and K. M. Dani, "Structure of the moiré exciton captured by imaging its electron and hole," *Nature*, vol. 603, no. 7900, pp. 247–252, 2022.

[102] M. Weinelt, M. Kutschera, T. Fauster, and M. Rohlfing, "Dynamics of exciton formation at the si(100) c(4 x 2) surface," *Phys. Rev. Lett.*, vol. 92, no. 12, p. 126801, 2004.

[103] W. Bennecke, A. Windischbacher, D. Schmitt, J. P. Bange, R. Hemm, C. S. Kern, G. D'Avino, X. Blase, D. Steil, S. Steil, M. Aeschlimann, B. Stadtmueller, M. Reutzel, P. Puschnig, G. S. Matthijs Jansen, and S. Mathias, "Multiorbital exciton formation in an organic semiconductor," *arXiv e-prints*, p. arXiv:2303.13904, Mar. 2023.

[104] P. Puschnig, S. Berkebile, A. J. Fleming, G. Koller, K. Emtsev, T. Seyller, J. D. Riley, C. Ambrosch-Draxl, F. P. Netzer, and M. G. Ramsey, "Reconstruction of Molecular Orbital Densities from Photoemission Data," *Science*, vol. 326, no. 5953, pp. 702–706, 2009.

[105] O. Karni, I. Esin, and K. M. Dani, "Through the lens of a momentum microscope: Viewing light-induced quantum phenomena in 2D materials," *Advanced Materials*, p. 2204120, 2022.

[106] M. Gutberlet, "High-harmonic generation in the tight focusing regime," Master's thesis, Georg-August-Universität Göttingen, 2020.

[107] A. M. Schulte, "Hoch-repetitive xuv-pulserzeugung mit hoher harmonischer generation," bachelor's thesis, Georg-August-Universität Göttingen, 2017.

[108] W. Bennecke, "Towards time- and spin-resolved orbital imaging using a time-of-flight momentum microscope," Master's thesis, Georg-August-Universität Göttingen, 2021.

[109] H. Nolte, "Darstellung und Analyse multidimensionaler Photoelektronenspektroskopie-Daten," Master's thesis, Georg-August-Universität Göttingen, 2019.

[110] M. Stellbrink, "2D elektronische strukturen an der oberfläche von $SrTiO_3$," bachelor's thesis, Georg-August-Universität Göttingen, 2019.

[111] S. Eich, A. Stange, A. V. Carr, J. Urbancic, T. Popmintchev, M. Wiesenmayer, K. Jansen, A. Ruffing, S. Jakobs, T. Rohwer, S. Hellmann, C. Chen, P. Matyba, L. Kipp, K. Rossnagel, M. Bauer, M. M. Murnane, H. C. Kapteyn, S. Mathias, and M. Aeschlimann, "Time- and angle-resolved photoemission spectroscopy with optimized high-harmonic pulses using frequency-doubled ti:sapphire lasers," *Journal of Electron Spectroscopy and Related Phenomena*, vol. 195, pp. 231–236, 2014.

[112] N. Barrett, E. Conrad, K. Winkler, and B. Krömker, "Dark field photoelectron emission microscopy of micron scale few layer graphene," *Review of Scientific Instruments*, vol. 83, no. 8, p. 083706, 2012.

[113] J. Kim, C. Jin, B. Chen, H. Cai, T. Zhao, P. Lee, S. Kahn, K. Watanabe, T. Taniguchi, S. Tongay, M. F. Crommie, and F. Wang, "Observation of ultralong valley lifetime in WSe_2/MoS_2 heterostructures," *Science Advances*, vol. 3, no. 7, p. e1700518, 2017.

[114] Y. Wang, Z. Wang, W. Yao, G.-B. Liu, and H. Yu, "Interlayer coupling in commensurate and incommensurate bilayer structures of transition-metal dichalcogenides," *Physical Review B*, vol. 95, p. 115429, Mar 2017.

[115] S. Ovesen, S. Brem, C. Linderälv, M. Kuisma, T. Korn, P. Erhart, M. Selig, and E. Malic, "Interlayer exciton dynamics in van der Waals heterostructures," *Communications Physics*, vol. 2, no. 1, p. 23, 2019.

[116] M. Förg, A. S. Baimuratov, S. Y. Kruchinin, I. A. Vovk, J. Scherzer, J. Förste, V. Funk, K. Watanabe, T. Taniguchi, and A. Högele, "Moiré excitons in $MoSe_2$-WSe_2 heterobilayers and heterotrilayers," *Nature Communications*, vol. 12, no. 1, p. 1656, 2021.

[117] H. Yu, G.-B. Liu, J. Tang, X. Xu, and W. Yao, "Moiré excitons: From programmable quantum emitter arrays to spin-orbit-coupled artificial lattices," *Science Advances*, vol. 3, no. 11, p. e1701696, 2017.

[118] F. Wu, T. Lovorn, and A. H. MacDonald, "Theory of optical absorption by interlayer excitons in transition metal dichalcogenide heterobilayers," *Physical Review B*, vol. 97, no. 3, p. 035306, 2018.

[119] K. Tran, G. Moody, F. Wu, X. Lu, J. Choi, K. Kim, A. Rai, D. A. Sanchez, J. Quan, A. Singh, J. Embley, A. Zepeda, M. Campbell, T. Autry, T. Taniguchi, K. Watanabe, N. Lu, S. K. Banerjee, K. L. Silverman, S. Kim, E. Tutuc, L. Yang, A. H. MacDonald, and X. Li, "Evidence for moiré excitons in van der Waals heterostructures," *Nature*, vol. 567, no. 7746, pp. 71–75, 2019.

[120] J.-J. Su and A. H. MacDonald, "How to make a bilayer exciton condensate flow," *Nature Physics*, vol. 4, no. 10, pp. 799–802, 2008.

[121] F. Wu, T. Lovorn, E. Tutuc, and A. H. MacDonald, "Hubbard Model Physics in Transition Metal Dichalcogenide Moiré Bands," *Physical Review Letters*, vol. 121, no. 2, p. 026402, 2018.

[122] Y. Cao, V. Fatemi, S. Fang, K. Watanabe, T. Taniguchi, E. Kaxiras, and P. Jarillo-Herrero, "Unconventional superconductivity in magic-angle graphene superlattices," *Nature*, vol. 556, no. 7699, pp. 43–50, 2018.

[123] L. Wang, E.-M. Shih, A. Ghiotto, L. Xian, D. A. Rhodes, C. Tan, M. Claassen, D. M. Kennes, Y. Bai, B. Kim, K. Watanabe, T. Taniguchi, X. Zhu, J. Hone, A. Rubio, A. N. Pasupathy, and C. R. Dean, "Correlated electronic phases in twisted bilayer transition metal dichalcogenides," *Nature Materials*, vol. 19, no. 8, pp. 861–866, 2020.

[124] E. C. Regan, D. Wang, C. Jin, M. I. Bakti Utama, B. Gao, X. Wei, S. Zhao, W. Zhao, Z. Zhang, K. Yumigeta, M. Blei, J. D. Carlström, K. Watanabe, T. Taniguchi, S. Tongay, M. Crommie, A. Zettl, and F. Wang, "Mott and generalized Wigner crystal states in WSe_2/WS_2 moiré superlattices," *Nature*, vol. 579, no. 7799, pp. 359–363, 2020.

[125] P. Rivera, H. Yu, K. L. Seyler, N. P. Wilson, W. Yao, and X. Xu, "Interlayer valley excitons in heterobilayers of transition metal dichalcogenides," *Nature Nanotechnology*, vol. 13, no. 11, pp. 1004–1015, 2018.

[126] K. S. Novoselov, V. I. Fal'ko, L. Colombo, P. R. Gellert, M. G. Schwab, and K. Kim, "A roadmap for graphene," *Nature*, vol. 490, no. 7419, pp. 192–200, 2012.

[127] T. Taniguchi and K. Watanabe, "Synthesis of high-purity boron nitride single crystals under high pressure by using Ba–BN solvent," *Journal of Crystal Growth*, vol. 303, no. 2, pp. 525–529, 2007.

[128] M. Keunecke, M. Reutzel, D. Schmitt, A. Osterkorn, T. A. Mishra, C. Möller, W. Bennecke, G. S. M. Jansen, D. Steil, S. R. Manmana, S. Steil, S. Kehrein, and S. Mathias, "Electromagnetic dressing of the electron energy spectrum of Au(111) at high momenta," *Physical Review B*, vol. 102, p. 161403, Oct 2020.

[129] N. R. Wilson, P. V. Nguyen, K. Seyler, P. Rivera, A. J. Marsden, Z. P. L. Laker, G. C. Constantinescu, V. Kandyba, A. Barinov, N. D. M. Hine, X. Xu, and D. H. Cobden, "Determination of band offsets, hybridization, and exciton binding in 2D semiconductor heterostructures," *Science Advances*, vol. 3, no. 2, p. e1601832, 2017.

[130] O. Karni, E. Barré, S. C. Lau, R. Gillen, E. Y. Ma, B. Kim, K. Watanabe, T. Taniguchi, J. Maultzsch, K. Barmak, R. H. Page, and T. F. Heinz, "Infrared Interlayer Exciton Emission in MoS_2/WSe_2 Heterostructures," *Physical Review Letters*, vol. 123, no. 24, p. 247402, 2019.

[131] R. Wallauer, P. Marauhn, J. Reimann, S. Zoerb, F. Kraus, J. Güdde, M. Rohlfing, and U. Höfer, "Momentum-resolved observation of ultrafast interlayer charge transfer between the topmost layers of MoS_2," *Physical Review B*, vol. 102, no. 12, p. 125417, 2020.

[132] S. Brem, C. Linderälv, P. Erhart, and E. Malic, "Tunable Phases of Moiré Excitons in van der Waals Heterostructures," *Nano Letters*, vol. 20, no. 12, pp. 8534–8540, 2020.

[133] M. Koshino, "Interlayer interaction in general incommensurate atomic layers," *New Journal of Physics*, vol. 17, no. 1, p. 015014, 2015.

[134] C. H. Stansbury, M. I. B. Utama, C. G. Fatuzzo, E. C. Regan, D. Wang, Z. Xiang, M. Ding, K. Watanabe, T. Taniguchi, M. Blei, Y. Shen, S. Lorcy, A. Bostwick, C. Jozwiak, R. Koch, S. Tongay, J. Avila, E. Rotenberg, F. Wang, and A. Lanzara, "Visualizing electron localization of WS_2/WSe_2 moiré superlattices in momentum space," *Science Advances*, vol. 7, no. 37, p. eabf4387, 2021.

[135] C. Tusche, A. Krasyuk, and J. Kirschner, "Spin resolved bandstructure imaging with

a high resolution momentum microscope," *Ultramicroscopy*, vol. 159, pp. 520–529, Dec. 2015.

[136] L. Miaja-Avila, C. Lei, M. Aeschlimann, J. Gland, M. Murnane, H. Kapteyn, and G. Saathoff, "Laser-assisted photoelectric effect from surfaces," *Physical Review Letters*, vol. 97, no. 11, p. 113604, 2006.

[137] A. J. H. Jones, R. Muzzio, S. Pakdel, D. Biswas, D. Curcio, N. Lanatà, P. Hofmann, K. M. McCreary, B. T. Jonker, K. Watanabe, T. Taniguchi, S. Singh, R. J. Koch, C. Jozwiak, E. Rotenberg, A. Bostwick, J. A. Miwa, J. Katoch, and S. Ulstrup, "Visualizing band structure hybridization and superlattice effects in twisted MoS_2/WS_2 heterobilayers," *2D Materials*, vol. 9, no. 1, p. 015032, 2021.

[138] G. Schönhense, D. Kutnyakhov, F. Pressacco, M. Heber, N. Wind, S. Y. Agustsson, S. Babenkov, D. Vasilyev, O. Fedchenko, S. Chernov, L. Rettig, B. Schönhense, L. Wenthaus, G. Brenner, S. Dziarzhytski, S. Palutke, S. K. Mahatha, N. Schirmel, H. Redlin, B. Manschwetus, I. Hartl, Y. Matveyev, A. Gloskovskii, C. Schlueter, V. Shokeen, H. Duerr, T. K. Allison, M. Beye, K. Rossnagel, H. J. Elmers, and K. Medjanik, "Suppression of the vacuum space-charge effect in fs-photoemission by a retarding electrostatic front lens," *Review of Scientific Instruments*, vol. 92, no. 5, p. 053703, 2021.

[139] S. Hellmann, K. Rossnagel, M. Marczynski-Bühlow, and L. Kipp, "Vacuum space-charge effects in solid-state photoemission," *Physical Review B*, vol. 79, p. 035402, Jan 2009.

[140] S. Passlack, S. Mathias, O. Andreyev, D. Mittnacht, M. Aeschlimann, and M. Bauer, "Space charge effects in photoemission with a low repetition, high intensity femtosecond laser source," *Journal of Applied Physics*, vol. 100, p. 024912, July 2006.

[141] M. Dendzik, R. P. Xian, E. Perfetto, D. Sangalli, D. Kutnyakhov, S. Dong, S. Beaulieu, T. Pincelli, F. Pressacco, D. Curcio, S. Y. Agustsson, M. Heber, J. Hauer, W. Wurth, G. Brenner, Y. Acremann, P. Hofmann, M. Wolf, A. Marini, G. Stefanucci, L. Rettig, and R. Ernstorfer, "Observation of an Excitonic Mott Transition through Ultrafast Core-cum-Conduction Photoemission Spectroscopy," *Physical Review Letters*, vol. 125, no. 9, p. 096401, 2020.

[142] P. Steinleitner, P. Merkl, P. Nagler, J. Mornhinweg, C. Schüller, T. Korn, A. Chernikov, and R. Huber, "Direct observation of ultrafast exciton formation in a monolayer of WSe_2," *Nano Letters*, vol. 17, no. 3, pp. 1455–1460, 2017.

[143] A. Steinhoff, M. Florian, M. Rösner, G. Schönhoff, T. O. Wehling, and F. Jahnke, "Exciton fission in monolayer transition metal dichalcogenide semiconductors," *Nature Communications*, vol. 8, no. 1, p. 1166, 2017.

[144] S. J. Ahn, P. Moon, T.-H. Kim, H.-W. Kim, H.-C. Shin, E. H. Kim, H. W. Cha, S.-J. Kahng, P. Kim, M. Koshino, Y.-W. Son, C.-W. Yang, and J. R. Ahn, "Dirac electrons

in a dodecagonal graphene quasicrystal," *Science*, vol. 361, no. 6404, pp. 782–786, 2018.

[145] G. S. M. Jansen, M. Keunecke, M. Düvel, C. Möller, D. Schmitt, W. Bennecke, F. J. S. Kappert, D. Steil, D. R. Luke, S. Steil, and S. Mathias, "Efficient orbital imaging based on ultrafast momentum microscopy and sparsity-driven phase retrieval," *New Journal of Physics*, vol. 22, no. 6, p. 063012, 2020.

[146] Y. Liu, N. O. Weiss, X. Duan, H.-C. Cheng, Y. Huang, and X. Duan, "van der Waals heterostructures and devices," *Nature Reviews Materials*, vol. 1, no. 9, p. 16042, 2016.

[147] S.-J. Liang, B. Cheng, X. Cui, and F. Miao, "Van der Waals heterostructures for high-performance device applications: Challenges and opportunities," *Advanced Materials*, vol. 32, no. 27, p. 1903800, 2020.

[148] E. Malic, M. Selig, M. Feierabend, S. Brem, D. Christiansen, F. Wendler, A. Knorr, and G. Berghäuser, "Dark excitons in transition metal dichalcogenides," *Physical Review Materials*, vol. 2, no. 1, p. 014002, 2018.

[149] R. Perea-Causin, D. Erkensten, J. M. Fitzgerald, J. J. P. Thompson, R. Rosati, S. Brem, and E. Malic, "Exciton optics, dynamics, and transport in atomically thin semiconductors," *APL Materials*, vol. 10, no. 10, p. 100701, 2022.

[150] D. N. Basov, R. D. Averitt, and D. Hsieh, "Towards properties on demand in quantum materials," *Nature Materials*, vol. 16, no. 11, pp. 1077–1088, 2017.

[151] A. de la Torre, D. M. Kennes, M. Claassen, S. Gerber, J. W. McIver, and M. A. Sentef, "Colloquium: Nonthermal pathways to ultrafast control in quantum materials," *Rev. Mod. Phys.*, vol. 93, p. 041002, Oct 2021.

[152] T. L. Cocker, D. Peller, P. Yu, J. Repp, and R. Huber, "Tracking the ultrafast motion of a single molecule by femtosecond orbital imaging," *Nature*, vol. 539, no. 7628, pp. 263–267, 2016.

[153] M. Garg and K. Kern, "Attosecond coherent manipulation of electrons in tunneling microscopy," *Science*, vol. 367, no. 6476, pp. 411–415, 2020.

[154] K.-D. Park, O. Khatib, V. Kravtsov, G. Clark, X. Xu, and M. B. Raschke, "Hybrid tip-enhanced nanospectroscopy and nanoimaging of monolayer WSe_2 with local strain control," *Nano Letters*, vol. 16, no. 4, pp. 2621–2627, 2016.

[155] M. Dąbrowski, Y. Dai, and H. Petek, "Ultrafast photoemission electron microscopy: imaging plasmons in space and time," *Chemical Reviews*, vol. 120, no. 13, pp. 6247–6287, 2020.

[156] T. Jakubczyk, G. Nayak, L. Scarpelli, W.-L. Liu, S. Dubey, N. Bendiab, L. Marty, T. Taniguchi, K. Watanabe, F. Masia, G. Nogues, J. Coraux, W. Langbein, J. Renard, V. Bouchiat, and J. Kasprzak, "Coherence and density dynamics of excitons in a single-layer mos2 reaching the homogeneous limit," *ACS Nano*, vol. 13, no. 3, pp. 3500–3511, 2019.

[157] T. Danz, T. Domröse, and C. Ropers, "Ultrafast nanoimaging of the order parameter in a structural phase transition," *Science*, vol. 371, no. 6527, pp. 371–374, 2021.

[158] A. S. Johnson, D. Perez-Salinas, K. M. Siddiqui, S. Kim, S. Choi, K. Volckaert, P. E. Majchrzak, S. Ulstrup, N. Agarwal, K. Hallman, R. F. Haglund, C. M. Günther, B. Pfau, S. Eisebitt, D. Backes, F. Maccherozzi, A. Fitzpatrick, S. S. Dhesi, P. Gargiani, M. Valvidares, N. Artrith, F. de Groot, H. Choi, D. Jang, A. Katoch, S. Kwon, S. H. Park, H. Kim, and S. E. Wall, "Ultrafast x-ray imaging of the light-induced phase transition in vo2," *Nature Physics*, vol. 19, no. 2, pp. 215–220, 2023.

[159] C. Poellmann, P. Steinleitner, U. Leierseder, P. Nagler, G. Plechinger, M. Porer, R. Bratschitsch, C. Schüller, T. Korn, and R. Huber, "Resonant internal quantum transitions and femtosecond radiative decay of excitons in monolayer WSe_2," *Nature Materials*, vol. 14, no. 9, pp. 889–893, 2015.

[160] S. J. Haigh, A. Gholinia, R. Jalil, S. Romani, L. Britnell, D. C. Elias, K. S. Novoselov, L. A. Ponomarenko, A. K. Geim, and R. Gorbachev, "Cross-sectional imaging of individual layers and buried interfaces of graphene-based heterostructures and superlattices," *Nature Materials*, vol. 11, no. 9, pp. 764–767, 2012.

[161] S. Kumar, A. Kaczmarczyk, and B. D. Gerardot, "Strain-induced spatial and spectral isolation of quantum emitters in mono- and bilayer WSe_2," *Nano Letters*, vol. 15, no. 11, pp. 7567–7573, 2015.

[162] Y. Bai, L. Zhou, J. Wang, W. Wu, L. J. McGilly, D. Halbertal, C. F. B. Lo, F. Liu, J. Ardelean, P. Rivera, N. R. Finney, X.-C. Yang, D. N. Basov, W. Yao, X. Xu, J. Hone, A. N. Pasupathy, and X. Y. Zhu, "Excitons in strain-induced one-dimensional moiré potentials at transition metal dichalcogenide heterojunctions," *Nature Materials*, vol. 19, no. 10, pp. 1068–1073, 2020.

[163] Y. Xu, S. Liu, D. A. Rhodes, K. Watanabe, T. Taniguchi, J. Hone, V. Elser, K. F. Mak, and J. Shan, "Correlated insulating states at fractional fillings of moiré superlattices," *Nature*, vol. 587, no. 7833, pp. 214–218, 2020.

[164] M. R. Rosenberger, H.-J. Chuang, M. Phillips, V. P. Oleshko, K. M. McCreary, S. V. Sivaram, C. S. Hellberg, and B. T. Jonker, "Twist angle-dependent atomic reconstruction and moiré patterns in transition metal dichalcogenide heterostructures," *ACS Nano*, vol. 14, no. 4, pp. 4550–4558, 2020.

[165] M. Kapfer, B. S. Jessen, M. E. Eisele, M. Fu, D. R. Danielsen, T. P. Darlington, S. L. Moore, N. R. Finney, A. Marchese, V. Hsieh, P. Majchrzak, Z. Jiang, D. Biswas, P. Dudin, J. Avila, K. Watanabe, T. Taniguchi, S. Ulstrup, P. Bøggild, P. J. Schuck, D. N. Basov, J. Hone, and C. R. Dean, "Programming moiré patterns in 2D materials by bending," *arXiv preprint arXiv:2209.10696*, 2022.

[166] G. Meneghini, S. Brem, and E. Malic, "Ultrafast phonon-driven charge transfer in van der Waals heterostructures," *Natural Sciences*, vol. 2, no. 4, p. e20220014, 2022.

[167] G. Meneghini, M. Reutzel, S. Mathias, S. Brem, and E. Malic, "Direct visualization of hybrid excitons in van der Waals heterostructures," *arXiv: 2305.03437*, 2023.

[168] Y. Cho and T. C. Berkelbach, "Environmentally sensitive theory of electronic and optical transitions in atomically thin semiconductors," *Physical Review B*, vol. 97, no. 4, p. 041409, 2018.

[169] J. Choi, W.-T. Hsu, L.-S. Lu, L. Sun, H.-Y. Cheng, M.-H. Lee, J. Quan, K. Tran, C.-Y. Wang, M. Staab, K. Jones, T. Taniguchi, K. Watanabe, M.-W. Chu, S. Gwo, S. Kim, C.-K. Shih, X. Li, and W.-H. Chang, "Moiré potential impedes interlayer exciton diffusion in van der Waals heterostructures," *Science Advances*, vol. 6, no. 39, p. eaba8866, 2020.

[170] R. P. Xian, Y. Acremann, S. Y. Agustsson, M. Dendzik, K. Bühlmann, D. Curcio, D. Kutnyakhov, F. Pressacco, M. Heber, S. Dong, J. Demsar, W. Wurth, P. Hofmann, M. Wolf, L. Rettig, and R. Ernstorfer, "An open-source, end-to-end workflow for multidimensional photoemission spectroscopy," *Scientific data*, vol. 7, no. 1, p. 442, 2020.

[171] R. P. Xian, L. Rettig, and R. Ernstorfer, "Symmetry-guided nonrigid registration: The case for distortion correction in multidimensional photoemission spectroscopy," *Ultramicroscopy*, vol. 202, pp. 133–139, 2019.

[172] J. Maklar, S. Dong, S. Beaulieu, T. Pincelli, M. Dendzik, Y. W. Windsor, R. P. Xian, M. Wolf, R. Ernstorfer, and L. Rettig, "A quantitative comparison of time-of-flight momentum microscopes and hemispherical analyzers for time- and angle-resolved photoemission spectroscopy experiments," *Review of Scientific Instruments*, vol. 91, no. 12, p. 123112, 2020.

[173] D. Christiansen, M. Selig, E. Malic, R. Ernstorfer, and A. Knorr, "Theory of exciton dynamics in time-resolved ARPES: Intra- and intervalley scattering in two-dimensional semiconductors," *Physical Review B*, vol. 100, no. 20, p. 205401, 2019.

[174] S. Ovesen, S. Brem, C. Linderälv, M. Kuisma, T. Korn, P. Erhart, M. Selig, and E. Malic, "Interlayer exciton dynamics in van der Waals heterostructures," *Communications Physics*, vol. 2, no. 1, pp. 1–8, 2019.

[175] J. Hagel, S. Brem, C. Linderälv, P. Erhart, and E. Malic, "Exciton landscape in van der Waals heterostructures," *Physical Review Research*, vol. 3, no. 4, p. 043217, 2021.

[176] S. Brem, M. Selig, G. Berghaeuser, and E. Malic, "Exciton relaxation cascade in two-dimensional transition metal dichalcogenides," *Scientific reports*, vol. 8, no. 1, p. 8238, 2018.

[177] Z. Jin, X. Li, J. T. Mullen, and K. W. Kim, "Intrinsic transport properties of electrons and holes in monolayer transition-metal dichalcogenides," *Physical Review B*, vol. 90, p. 045422, Jul 2014.

[178] M. Kira and S. W. Koch, "Many-body correlations and excitonic effects in semicon-

ductor spectroscopy," *Progress in quantum electronics*, vol. 30, no. 5, pp. 155–296, 2006.

[179] H. Haug and S. W. Koch, *Quantum theory of the optical and electronic properties of semiconductors*. World Scientific Publishing Company, 2009.

[180] E. Malic and A. Knorr, *Graphene and carbon nanotubes: ultrafast optics and relaxation dynamics*. John Wiley & Sons, 2013.

[181] J. Maklar, S. Dong, S. Beaulieu, T. Pincelli, M. Dendzik, Y. W. Windsor, R. P. Xian, M. Wolf, R. Ernstorfer, and L. Rettig, "A quantitative comparison of time-of-flight momentum microscopes and hemispherical analyzers for time-and angle-resolved photoemission spectroscopy experiments," *Review of Scientific Instruments*, vol. 91, no. 12, p. 123112, 2020.

[182] A. Klenke, M. Müller, H. Stark, M. Kienel, C. Jauregui, A. Tünnermann, and J. Limpert, "Coherent beam combination of ultrafast fiber lasers," *IEEE Journal of Selected Topics in Quantum Electronics*, vol. 24, no. 5, pp. 1–9, 2018.

[183] G. Schönhense, K. Medjanik, and H.-J. Elmers, "Space-, time- and spin-resolved photoemission," *Journal of Electron Spectroscopy and Related Phenomena*, vol. 200, pp. 94–118, Apr. 2015.

[184] B. Krömker, M. Escher, D. Funnemann, D. Hartung, H. Engelhard, and J. Kirschner, "Development of a momentum microscope for time resolved band structure imaging," *Rev. Sci. Instrum.*, vol. 79, no. 5, pp. 053702–7, 2008.

[185] L. Britnell, R. M. Ribeiro, A. Eckmann, R. Jalil, B. D. Belle, A. Mishchenko, Y.-J. Kim, R. V. Gorbachev, T. Georgiou, S. V. Morozov, A. N. Grigorenko, A. K. Geim, C. Casiraghi, A. H. C. Neto, and K. S. Novoselov, "Strong light-matter interactions in heterostructures of atomically thin films," *Science*, vol. 340, no. 6138, pp. 1311–1314, 2013.

[186] D. K. Schroder, "Surface voltage and surface photovoltage: history, theory and applications," *Measurement Science and Technology*, vol. 12, no. 3, p. R16, 2001.

[187] M. Ogawa, S. Yamamoto, K. Fujikawa, R. Hobara, R. Yukawa, S. Yamamoto, S. Kitagawa, D. Pierucci, M. G. Silly, C.-H. Lin, R.-Y. Liu, H. Daimon, F. Sirotti, S.-J. Tang, and I. Matsuda, "Relaxations of the surface photovoltage effect on the atomically controlled semiconductor surfaces studied by time-resolved photoemission spectroscopy," *Phys. Rev. B*, vol. 88, p. 165313, Oct 2013.

APPENDIX A

Additional information to the trMM setup

A.1. The 300-W Yb fiber-based laser system

The optical setup is based on a 300-W Yb fiber-based laser system from Active Fiber Systems (AFS). Such large average powers are achieved by using a coherent combination of multiple large power laser beams [182]. The laser is operated at a repetition rate of 500 kHz with pulse lengths of about 250 fs and a central wavelength of 1030 nm. A part of the light is propagating through a hollow-core-fibre (HFC), whereby through nonlinear self-phase-modulation new frequency components are generated. A pair of chirped mirrors provides a compression of the light to a pulse duration of about 30-40 fs (Gaussian). After that, the beam is frequency doubled to 515 nm and then used for high-harmonic generation (schematic beam path as solid green line in Fig. 2.6.1). The uncompressed part of the light is used as a driver for the optical parametric amplification (OPA: light conversion), whereby through a combination of WLG (white light generation), SFG (sum frequency generation) and DFG (difference frequency generation) processes a wide range of wavelengths from 310 nm to 16 µm can be generated. The output light of the OPA is directed to a motorized delay stage in order to exactly adjust the temporal overlap between pump and probe. After that, the beam is focussed into the momentum microscope (schematic beam path as solid red line in Fig. 2.6.1). Prior to focussing, the polarization and fluence can be changed by a $\frac{\lambda}{2}$-waveplate and by a ND-filter wheel. The spot profile for 1.7 eV pump photon energies inside the momentum microscope is shown in Fig. A.2.1 a).

A.2. High harmonic generation and XUV monochromatization

The efficiency and the general generation scheme of the high harmonic generation process and its monochromatization scheme is described in detail, ref. [55] and [29]. In short, the high harmonics are generated with the frequency-doubled output at 515 nm with a fluence of about 16 µJ (p-polarized, 65 fs) by focussing (75 mm focal length) into an argon gas jet (2 bar backing pressure). This results in a high-harmonic spectrum ranging from 20 to 32 eV with a high-harmonic separation of 4.8 eV [55]. To avoid overlapping photoemission spectra and influences of the driving light in the photoemission detection scheme, it is necessary to select a certain high-harmonic from the high-harmonic spectra. For that, a monochromati-

zation is performed using a combination of two grazing incidence plates (GIP), reflecting only the high-harmonics and transmitting the driving light, and two multilayer mirrors, reflecting selectively the 11th harmonic (46.6 nm = 26.4 eV, 5 nm bandwidth). The second one of these two multilayer mirrors is a concave mirror with a curvature of 1200 mm, which focuses the selected harmonic onto the sample inside the momentum microscope. Prior to that, the selected high harmonic passes through an 100 nm Aluminum filter in order to absorb the residual fundamental light. In this work, in comparison to ref.[55] and [29] the first GIP was exchanged by a curved GIP (Radius of curvature 3000 mm) that enables better beam focussing and minimizes astigmatism. By that, the beam diameter in the horizontal direction can be decreased by a factor of about four, which increases the fluence by a factor of four (c.f. A.2.1 b), c), d)). Beside the high-repetition rate, a large fluence (small beam diameter) is one of the main requirements for efficient momentum microscopy of µm-sized samples and dark-field ARPES measurements (detailed in section A.4 and section A.5).

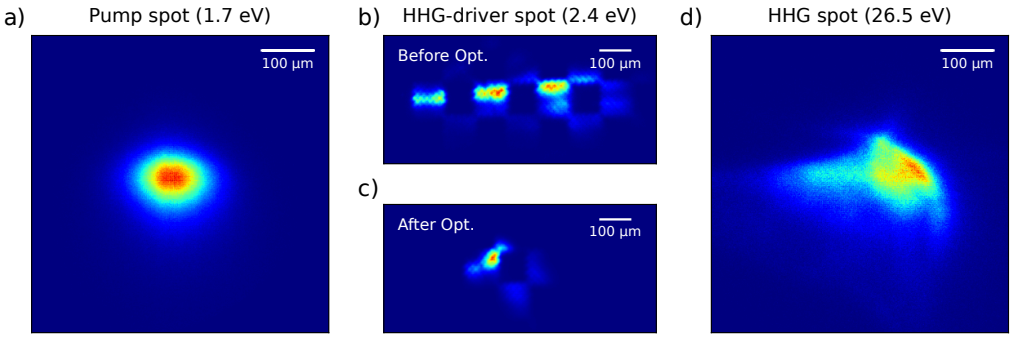

Fig. A.2.1.: a) Beam profile of the pump (1.7 eV) beam. b), c) Profile of the HHG-driver (2.4 eV) before and after inserting the curved rejector. The spotsize is optimized from about 800x200 µm^2 to about 200x200 µm^2. d) Profile of the optimized HHG (26.6 eV). All profiles are directly measured using the real space mode of the momentum microscope. Profiles b), c) and d) are measured on a gold chessy sample (periodic array of SiO_2 and gold), which provides a real-space calibration but also leads to a modulation of the photoemission yield due to the different work functions of SiO_2 and gold regions. Profile a) was measured on a pristine Graphene sample. Note that the respective photon energies of a), b), c) are below the material's work function and, hence, multiphoton processes alter the true spot size of the beam.

A.3. Momentum microscopy

The working scheme of the momentum microscope including the function of the lens system is described in detail in ref.[55, 29, 35, 183]. Here, only a brief introduction into the basic working principle will be given. One of the major advantages of the momentum microscope compared to photoemission detection schemes using hemispherical analyzers is the simultaneous detection of three-dimensional data sets containing the real-space (x, y) coordinates or the momentum-space coordinates (k_x, k_y) and the respective kinetic energy of photoemitted electrons. The functional principle is based on a combination of different electrostatic lens sections and the delay line detector (DLD) that allows the multidimensional detection scheme. The microscope lens system allows effortless switching between real-space and momentum-space imaging, and allows additional manipulation of the respective image planes by inserting apertures. This opens up the possibility to image micrometer-sized samples in momentum-space and also enables dark-field momentum microscopy. These operational modes are the essential key-requirements for the data acquisition of this Phd-thesis and the resulting publications listed in chapter (2.7). In the following, a more detailed description of the operation principle is provided.

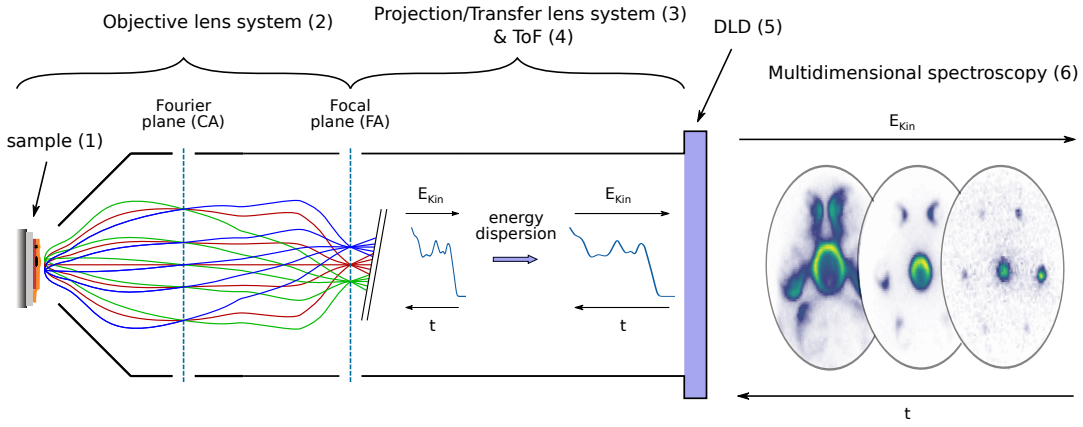

Fig. A.3.1.: Schematic layout of the momentum microscope. From left to right starting with the sample (1), the objective- (2) and projective/transfer (3) lens system, the time-of-flight drift tube (4) and the delay-line-detector (5), which is able to measure the k_x, k_y, E coordinates of the incoming photoelectrons simultaneously. (6) Multidimensional photoemission detection scheme illustrated for the WSe_2/MoS_2 heterostructure. Image adapted from [55].

A.3.1. Lens system and delay line detector

A schematic illustration of the microscope is given in Fig. A.3.1 including exemplary beam paths of the photoemitted electrons. The different section of the momentum microscope are separated into the objective lens system (2), including the sample (1), the projection/transfer lens system (3), the time-of-flight drift tube (4) and the photoelectron detector (DLD) (5),

which enables the multidimensional photoemission detection scheme (6). The different sections are now briefly described.

(1, 2) Sample and objective lens system: The sample (1) is mounted onto a hexapod, allowing sample movements (and slight rotations) in every possible direction in space. The hexapod can also be operated at cryogenic temperatures down to 12 K. The sample and the hexapod as part of the lens system usually are on a constant potential (0 - 22 V dependent on the selected sharp energy range, cf. see further in text). The extractor, as the second element of the objective lens system, is operated at very high voltages (typically 16 kV) and ensures that each photoelectron leaving the sample is accelerated into the lens system. In that way, the whole half-plane of photoemitted electrons ($\pm 90°$) is accessible. After that, the lens system creates achromatic images in the Fourier plane and the image plane. In the Fourier plane, all photoelectrons emitted under the same emission angle are focussed on one point. Since the emission angle is directly connected to the in-plane-momentum of the photoemitted electron, the achromatic momentum-resolved electron distribution is mapped at this plane. In the image plane, all photoelectrons emitted from the same region of the sample are focussed, resulting in a mapping of the achromatic real-space distribution of the photoemitted electrons. The settings of the objective lens, and especially the extractor voltage, define strongly the magnification of the respective images.

(3) The projective/transfer lens: Next, the electrons travel through the projective/transfer lens. Here, the previously generated images are transferred to the photoemission detector with an additional magnification. In this section, the images can be shifted and further optimized by introducing magnetic deflectors. Before entering the drift tube of the momentum microscope, the electrons are decelerated. The deceleration is defined by the potential difference of the last lens element (before the drift tube) and the sample potential.

(4) The drift tube: In the drift tube, the electron beam propagate freely in a constant potential. Because of the different kinetic energies, the electron beam disperses over the length of the drift tube, resulting in an effective stretching of the photoelectron spectra. The dispersion is determined by the length of the drift tube and the entry velocity, e.g., for smaller entry velocities, the dispersion increases. Because of the finite energy (time-of-flight)-resolution of the photoelectron detector, the dispersion has direct influence on the energy-resolution of the microscope (c.f. A.6.1).

(5, 6) The photoelectron detector and multidimensional detection scheme: The last part of the microscope is the photoelectron detector, which consists of a microchannel plate (MCP) array and the delay-line-detector (DLD). The MCP multiplies the incoming electrons and generates an electron-bunch. This bunch then impinges on two intertwined wires, where a voltage pulse is generated. By measuring the time difference of the propagating voltage pulse on both sides of the wire, the incidence point of the bunch can be exactly determined. In addition, this detection scheme gives simultaneous access to the detection time of the electron. With the help of the pulsed trigger signal of the laser system, this provides access to the time of flight and therefore (with a given length of the drift tube) the kinetic energy of

the photoemitted electrons. In that way, the momentum-space or real-space coordinates and the corresponding energy of the photoelectrons can be measured simultaneously, enabling the multidimensional imaging of photoelectrons.

A.4. Momentum microscopy of µm-sized samples

The momentum-resolved mode of the momentum microscope allows the simultaneous acquisition of the two in-plane momentum-coordinates and the energy coordinate of the photoelectrons. This mode provides direct access to the 3D band structure within µm-sized probing areas. A schematic illustration of the working principle of the momentum-resolved mode and exemplary resulting data sets are shown in Fig. A.4.1.

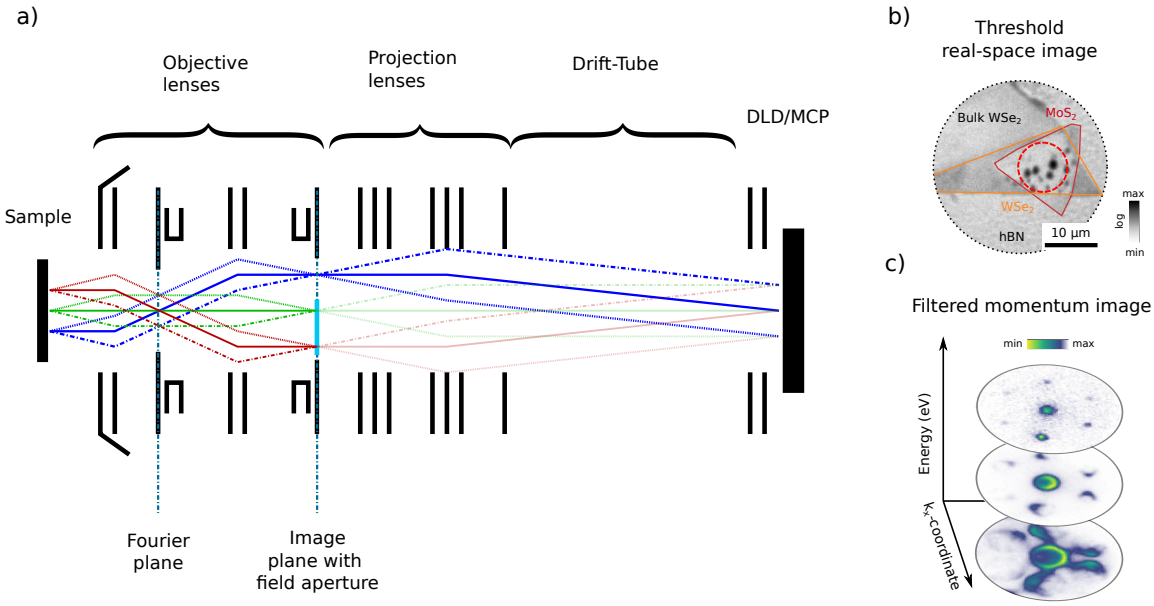

Fig. A.4.1.: a) Schematic photoelectron paths of the momentum microscope in the momentum-resolved mode. The different colors indicate electrons photoemitted from different regions of the sample. Additionally, the different lens section are indicated and the Fourier and image plane are identified with blue dashed lines. The field aperture in the image plane only allows the transmission of electron emitted from certain spatial positions. b) Threshold PEEM image of an exemplary TMD sample and selected region-of-interest for real-space filtering (red circle). c) Real-space filtered momentum-resolved image of the region selected in b). Image a) adapted from [108] and [184] and b) adapted from [28].

In this mode, the Fourier plane is projected to the detector as shown in Fig. A.4.1. The momentum microscope allows inserting an aperture in the image-plane (real-space image) in order to select only a certain region-of-interest from the sample. The size of the aperture in real-space is determined by the size of the aperture that can be selected in different sizes from 40 µm to 2000 µm diameter, and the applied extractor voltage, which determines the magnification of the image plane. The used extractor setting of 16 kV (magnification of 10.1) leads to respective magnified sizes of the aperture of 3.5 µm to 190 µm. In the experiments presented in this thesis, usually a magnified aperture size of 10 µm has been selected. In that

way, depending on the size of the aperture the photoemission signal from very small regions, e.g. µm-sized flakes can be measured, which allows the access to new sample systems such as the exfoliated TMD samples. Beside the discussed experimental requirements (optimized beam diameters and high-repetition-rates), this new technique requires a careful optimization procedure of the microscope itself.

Threshold real-space image: In the following, the microscope alignment procedure in the case of the momentum-resolved measurements of µm-sized sample is described. The first step is to perform a threshold real-space image of the sample (A.4.1 b)). During this step, initial optimizations, such as applying focal series and aligning the sample, are performed in order to calibrate the objective lens system. Here, especially for momentum microscopy of µm-sized samples, the first optimization is performed in the lowest magnification of the projective/transfer lens system and subsequently the magnification is changed to higher values and further adjustments have to be performed.

Optimization of the projective lens system: In order to adjust the projective/transfer lens system and the subsequent optics, a grid (aperture with an equally spaced array of stripes) can be inserted in the image-plane. By tweaking various lens parameters of the respective lens system, the grid sharpness on the detector and hence the lens system can be optimized.

Selection of a region-of-interest in the image plane: After that, the selected real-space aperture can be inserted into the image plane to select the desired region of interest (A.4.1 b), red circle). Notably, after setting this aperture, any change of the objective lens system (including also the sample) can alter the position and the size of the aperture with respect to the image. Especially when performing measurements of µm-sized flakes, the objective lens is very sensitive to small changes. At this point, the light source is changed to the 26.4 eV HHG light source. With the help of a motorized multilayer mirror, the position of the HHG spot is optimized to the center of the aperture and therefore to the highest photoelectron yield.

Calibration/Optimization of the momentum-resolved image: After that, the momentum microscope's transfer lens is set to momentum-resolved mode. Note that the switching to other imaging modes does not manipulate the respective images of the objective lens. However, the electron beam usually experiences a constant shift (or tilt) when switching to other imaging modes. To compensate that shift, either (i) the position of the aperture and the beam can be changed, which requires an alignment of the sample's region of interest to the adjusted aperture position or (ii) shifting and tilting of the image by applying magnetic deflectors. Step (i) has the advantage that the lens system operates in the optimized geometry, but additional adjustments of the objective lens system, including iteration-wise switching between real-space mode and momentum-mode, are necessary. The alignment procedure of (ii) is much faster and allows a direct alignment of the photoemission horizon to the detector. In the case of larger applied shifts, e.g., larger deflector voltages, the image can suffer from distortions and less sharp signatures. In order to avoid such distortions, most of the measurements acquired in this work and the respective publications were therefore performed using procedure (i).

Calibration of the energy range: The next step involves the shifting of the desired energy range into the sharp energy region of the momentum microscope. The reason for this is that only a certain energy interval is mapped inside the focused region. In typical experiments, this range covers about 6 eV depending on the kinetic energy inside the drift tube and the inserted aperture, which gives additional depth of field [181]. Initially, this range is in the energy range of the secondary electrons (low kinetic energies) for the given experimental settings (without sample voltage). Now, by changing the drift energy inside the drift tube (potential difference between sample and last element before entering the drift tube) the photoemission horizon can be shifted energetically and thereby the desired energy range can be mapped to the focused region. After applying this shift, further adjustments of the orientation of the photoemission horizon, such as compensating for astigmatism or residual tilts and shifts with the help of magnetic deflectors, are performed.

Data saving: As the last step, the right energy and momentum range has to be determined software-wise. Since the size of one data set can extend multiple Gigabytes, a certain amount of pixels is grouped into a larger pixel (so-called binning) for efficient and space-saving data accumulation. The momentum-space resolution of the acquired images strongly depends on the performed optimization steps explained here. Under best conditions, the maximal achievable momentum-resolution was recorded by Tusche *et al.* to 0.01 1/Å[135]. The momentum-resolution of the given microscope settings used in this work is about 0.04 ± 0.01 1/Å[28] as demonstrated in Fig. A.4.2.

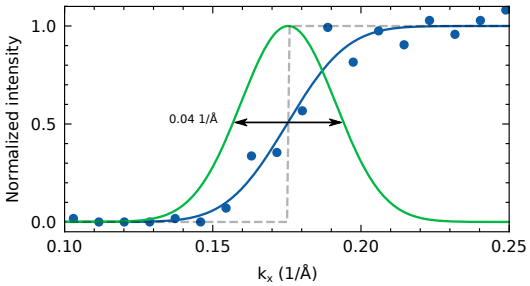

Fig. A.4.2.: The momentum resolution of the experiment is extracted from the edge of the photoemission horizon. Fitting a convolution of a heavyside function (gray dashed) and a Gaussian (green line) yields a momentum resolution of about 0.04 1/Å.

A.5. Real-space and dark-field momentum microscopy

The real-space mode of the momentum microscope allows the simultaneous detection of the two real-space coordinates and the energy coordinate of the photoelectrons. In that way, this mode provides access to the 3D real-space distribution of the photoelectrons with the possibility to also map certain momentum-selected regions-of-interest onto real-space coordinates. The schematic beam path of photoelectrons in the real-space resolved mode and an exemplary resulting dark-field data set are shown in Fig. A.5.1.

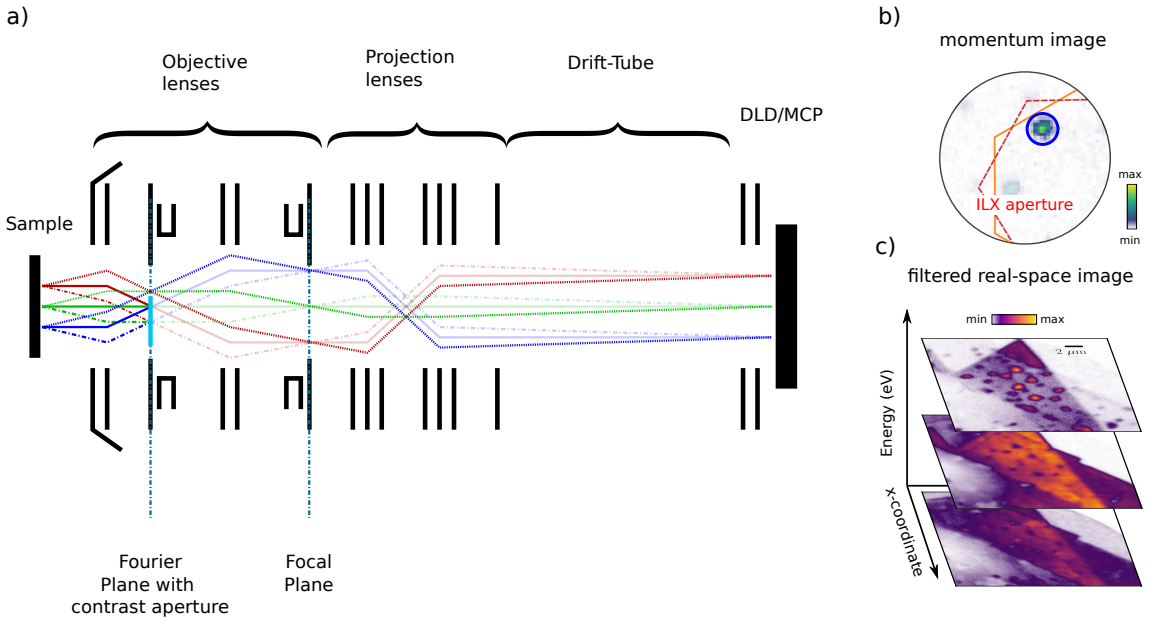

Fig. A.5.1.: a) Schematic photoelectron paths of the momentum microscope in the real-space mode. The different colors indicate electrons photoemitted from different regions of the sample. Additionally, the different lens sections are schematically indicated and the Fourier and image plane are marked with blue dashed lines. The contrast aperture in the Fourier plane allows the transmission of photoelectrons with certain emission angles. b) Momentum-resolved image of an exemplary TMD sample and selected region-of-interest for momentum-space filtering. c) Momentum-filtered real-space resolved image of the region selected in b). Image a) adapted from [108] and [184] and image b) adapted from [30].

In the real-space mode of the momentum microscope, the image plane is projected to the detector as demonstrated in Fig. A.5.1. For real-space resolved measurements, the general alignment procedure is similar to the momentum-resolved measurements but includes, especially for the dark-field microscopy, further steps and some modifications of the described procedure. Most importantly, the shifting and tilting of the sample is only optimized in the

real-space resolved mode and the alignment of the momentum-resolved image is performed only with the help of deflectors, in order to keep the real-space resolution as good as possible.

Selection of a region-of-interest in the Fourier plane: After adjusting the momentum-resolved image, a contrast aperture is introduced into the Fourier plane. Here, a certain region of interest (or signature) in momentum-space can now be selected. The exact size of the aperture in momentum-space is given by the size of the aperture, where different sizes can be selected of 75 µm, 100 µm and 200 µm diameter and the applied extractor voltage, which defines the magnification of the Fourier-plane. The used extractor setting of 16 kV leads to respective momentum-resolved sizes of the aperture of 0.4 1/Å, 0.2 1/Åand 0.15 1/Å. After inserting the aperture, the momentum microscope is set again to the real-space imaging mode and the before mentioned real-space aperture is removed.

Data saving: As the last step, the right energy and real-space range (+ pixel binning) has to be determined software-wise for efficient and space-saving data accumulation. The real-space resolution of the acquired images strongly depend on the performed optimization steps explained before, but also on the position of the inserted aperture. In the off-axis case, lens distortions, such as spherical aberration, could affect the image quality. Further, a strong lateral energy-dependent shift of the image can be observed. The maximal resolution extracted in the dark-field geometry is about 500 nm (c.f. chapter 4), whereas under optimal conditions (centered aperture, switched-off turbo pumps) an ultimate resolution of about 118 nm can be achieved [55], as demonstrated on a chessy-sample in Fig. A.5.2.

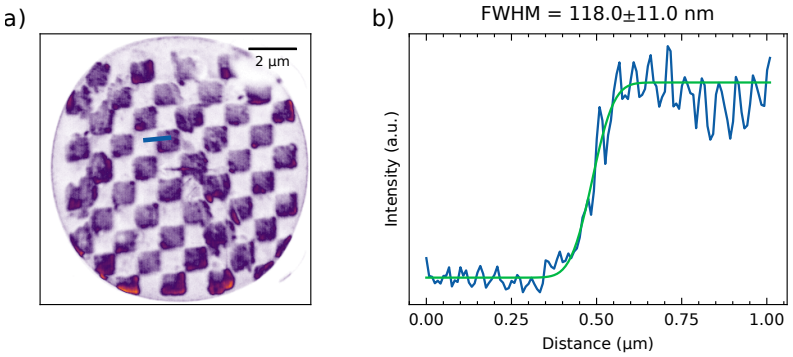

Fig. A.5.2.: a) Threshold PEEM image of a chessy sample. The chessy-sample consists of an alternating periodic pattern between gold and SiO_2. Because of the different work functions of the respective materials, the pattern can be visualized in the PEEM mode. For this specific image a monchromatic Hg lamp was used, and to avoid any vibrational influnces, also turbo pumps were switched off. b) The extracted line profile at one of the SiO_2-Au edges yields a real-space resolution of 118 $\pm$ 11 nm (FWHM), determined by fitting an errorfunction. Image reproduced from [55]. The additional oscillation of the intensity in b) reflects the electrode array of the delay line detector.

A.6. Energy-resolution of the trMM setup

The kinetic energies of the photoelectrons are measured via time-of-flight. Since the photoelectron detector has a maximal temporal resolution of 180 ps, the energy resolution can be strongly improved by increasing the dispersion and hence, the travel time of the electrons inside the drift tube. The energy resolution as a function of the kinetic energy of the electrons was simulated by Martin Ellguth (Surface Concept GmbH) and is shown in Fig. A.6.1 a).

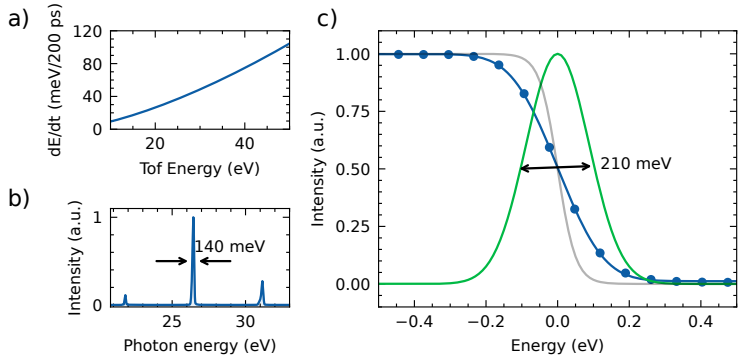

Fig. A.6.1.: a) Energy-resolution as a function of the photoelectron kinetic energy inside the time-of-flight drift tube. The Simulation was provided by Martin Ellguth. b) High harmonic spectra generated in an argon gas jet. The 11th harmonic at 26.5 eV has a bandwidth of 140 meV, measured with a home-built spectrometer and an EUV-CCD camera. c) Photoelectron spectra at the Fermi-edge of an Au(111) single crystal. The overall energy resolution can be determined by convolving a room temperature (300 K) Fermi-Dirac distribution (gray line) with a gaussian distribution, accounting for instrumental and bandwidth broadening. The fit yields a FWHM of 210 meV for the Gaussian broadening in accordance with reference [29]. Image inspired from [55].

The kinetic energy of the photoemitted electrons in the drift tube depend mainly on the probe photon energy, the work function of the material, and the potential difference between the sample potential and the potential of the drift tube. In the given experimental setup for the used settings with a 26.5 eV probe photon energy, a work function of 4-5 eV (For WSe_2 W=4.3 eV [185]), a sample voltage of 20 V and drift voltage of 40 V, the kinetic energy of the photoemitted electrons at the Fermi-energy (binding energy=0) inside the drift tube can be calculated to 41.7 eV. According to the simulation, this value corresponds to an instrumental energy-resolution of about 80 meV. Note that the simulation is performed with a slightly lower DLD temporal resolution of 200 ps, which affects the calculated energy resolution.

In addition, the bandwidth of the given light source has to be considered. In Fig. A.6.1 b) the high-harmonic spectrum was measured using a home-built spectrometer with an EUV-CCD camera. From this measurement, the bandwidth of the used 11th harmonic can be determined

to 140 meV. Assuming these factors as the main reason for the energy-resolution of the experiment, the overall energy resolution yields a value of about 160 meV. In the experiment, the overall energy-resolution can be extracted by fitting the Fermi-edge of the photoelectron spectra with a room temperature Fermi-Dirac distribution convoluted with a gaussian distribution for additional broadening A.6.1 c). The fit yields a FWHM of 210 ± 10 meV for the gaussian broadening [29], concluding that the overall broadening is governed by the bandwidth of the HHG.

A.7. Time-resolved momentum microscopy

All time-resolved momentum microscopy experiments in this work are performed using the 26.5 eV (p-polarized) HHG beam line and the tunable OPA (mostly s-polarized) pump beam line. The temporal delay between both pulses can be controlled via a delay-stage located in the OPA pump beam line. For the most experiments in this work, the OPA photon energy was tuned to 1.7 eV (740 nm) in order to resonantly excite the A-exciton of WSe_2. The polarization state can be controlled using a $\frac{\lambda}{2}$-plate and the fluence can be adjusted by a ND-filter wheel. One of the requirement for performing trARPES measurements is the spatial and temporal alignment of the pump-probe overlap.

A.7.1. Calibration of the setup for time-resolved measurements

The general calibration scheme was already described in the Phd-thesis of Marius Keunecke [55], where the author discussed the temporal-alignment using a large-scale (mm-sized) Graphene sample. For µm-sized TMD-flakes, investigated in this work, some considerations have to be taken into account. Therefore, a brief overview of the adjustment steps will be given.

For the calibration, the spatial and the temporal overlap of the respective beams have to be optimized. Here, another great advantage of the microscope comes into play. Because of the real-space capabilities of the microscope, the beams can be directly imaged and hence, the spatial overlap can be optimized straightforwardly. For this and the following calibration step, most of the time, the HHG driving light (frequency doubled laser output at 515 nm, p-polarized) is used. After having overlapped the beams spatially, the temporal overlap can be determined by monitoring the photoemission yield as a function of delay-stage position. Because the work function of most materials is about 3-5 eV, two or more photons of the pump (1.7 eV) and probe (HHG-driver at 2.4 eV)-photons are necessary to overcome the material's work function. This nonlinear multiphoton-photo-absorption process is strongly dependent on the applied peak-intensity, and therefore is strongly enhanced when both beams overlap. Performing these two calibration steps, the spatial- and temporal overlap can be found within a few minutes.

For the µARPES measurements discussed in section A.3, the calibration procedure has to be repeated inside the aperture's selected region of interest. Because the inserted aperture sizes are much smaller than the beam diameter (c.f. Fig. A.2.1), the spatial positions are calibrated by monitoring the photoemission yield inside the aperture as function of the beam position. After performing the calibration steps, the momentum microscope is set to the desired imaging mode and the HHG is used as the probe light source.

As a last calibration step, the time-resolved photoemission signal above the Fermi-energy is tracked as a function of pump-probe-delay. Note that this photoemission yield includes a combination of (1) coherent two photon processes [51], (2) electron excitation/dynamics

and further relaxation channels [56]. The latter one (2) could lead to high occupations above the Fermi-Energy even after the pump-probe overlap, e.g. for impact ionization processes, and hence, the highest yield does not necessarily correspond to the optimal overlap between both pulses. On the other hand, the coherent two photon process (1) leads to replica of the band structure, displaced energetically by the pump photon energy, existing only during the pump-probe overlap, and hence, provide a cross-correlation between the applied pulses which defines the time-zero "t=0 fs" (time-zero) of this experiment throughout this work [29]. Since both processes (1) and (2) lead to distinct photoemission signatures in momentum- and energy-space, process (1) can be measured by monitoring the photoemission yield of selected regions of interest. As a rough guide for the optimal spatial and temporal overlap, the photoemission yield above the Fermi-energy, in this work, was about 30–60 counts per second (pump: 50 mW, p-polarized; probe: 1-3 $\times 10^5$ cps within a 10 µm aperture, p-polarized).

A.8. Time-resolution of the trMM setup

The overall temporal-resolution of the experiment defines significantly the results obtained in this work, such as the access to exciton formation times, which occur on the hundred femtosecond timescale. The overall temporal-resolution is a convolution of the pump and probe pulse-lengths. The pulse length of the pump-beam (1.7 eV) can be measured by performing an autocorrelation (APE pulseCheck). The measured autocorrelation yields a FWHM of 40 fs (c.f. A.8.1 dashed greem line, sech^2). Assuming Fourier-limited HHG pulses, the HHG pulse length can be calculated with the respective bandwidth of the 11th harmonic (A.6.1 b)) and yield a value of 13.5 fs. Hence, an overall temporal-resolution of 52 fs can be estimated. An experimentally accurate value of the overall temporal resolution provides the coherent two photon process (LAPE), discussed in the section before. The temporal evolution of the extracted photoemission yield provides the cross-correlation between the applied pulses. Fitting a Gaussian distribution to the signal yields a total time-resolution of 54 $\pm$ 2 fs. From this measurement, the actual HHG pulse length can be determined to 25 $\pm$ 2 fs, calculated by deconvolving the pump pulse-length (40 fs, sech^2) from the measured signal.

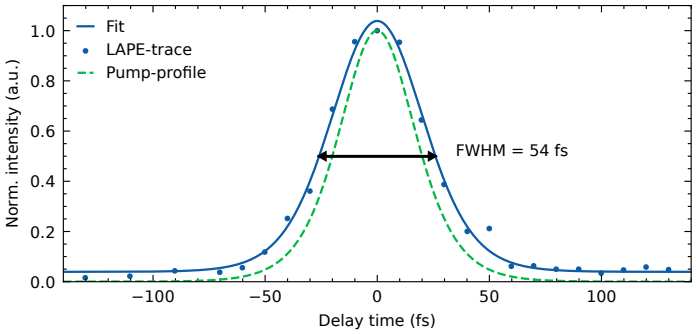

Fig. A.8.1.: Photoemission yield of LAPE (blue points). The FWHM of 54 $\pm$ 2 fs is extracted by applying a Gaussian fit to the data (green line). The autocorrelation of the pump-pulse (1.7 eV) yields a pulse length of 40 fs (orange line). Image adapted from [70].

A.9. Limitations of the trMM setup

The two articles of this manuscript-based thesis showcase the unique capabilities of the given trMM setup. However, there are also limitations of the current setup in terms of image quality, integration times and stability, which need to be considered carefully. In the following, a list of the main limitations is given:

1. Space-charge effects, leading to distortions in momentum and energy
2. Aging (decreasing efficiency) of the micro channel plate for large count rates
3. Sample design for photoemission experiments
4. Sample charging and space charge effects inside the sample
5. Sample heating due to high pump average powers
6. Lateral shifts of the sample
7. Stability of the laser system in terms of beam pointing
8. Limited options of aperture sizes and forms

Space-charge effects: For momentum microscopy of µm-sized samples and dark-field experiments, these effects have to be crucially considered, in order to perform efficient experiments. As described in section A.3 due to the small aperture sizes (10 µm) only a small fraction of the HHG beam is used for photoelectron imaging as demonstrated in Fig. A.9.1.

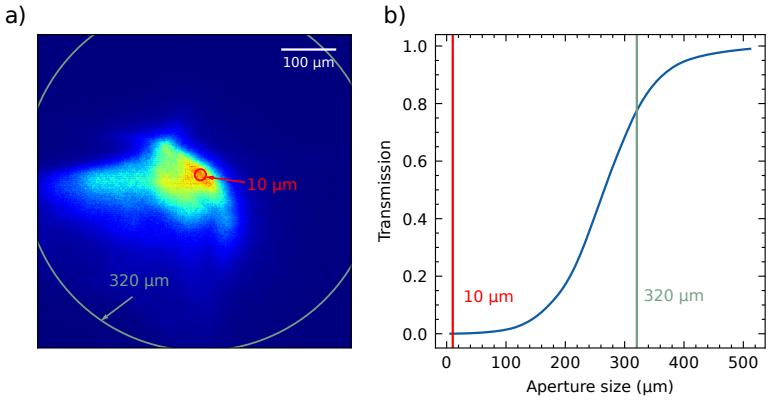

Fig. A.9.1.: a) HHG spot in the real-space mode of the momentum microscope. Two apertures with sizes of 10 µm (red circle) and 320 µm (green circle) are indicated. b) A transmission curve is extracted by evaluating the photoelectron counts for an increasing aperture radius and by normalizing through the total photoelectron yield without the aperture. The two exemplary apertures from a) are indicated as vertical lines. Image inspired by [181].

In order to extract photoemission data with feasible integration times, the total detector count rate has to be in the order of $1 - 3 \times 10^5$ cps (counts per second). Following the transmission

curve of Fig. A.9.1 the estimated count rate before entering the 10 µm sized aperture is on the order of $1-3\times10^8$. Since this count rate is significantly above the space charge limit (1 e^-/pulse), these large e^-/pulse could cause space-charge induced broadening of the bands and an additional overall shifting of the photoelectron spectra [181]. However, in the experiment, no significant broadening or shifting effects were observed for the used electron yields. Only at larger detector counts in the range of $>4-6\times10^5$ cps, a significant energetic shift of the spectra was observed.

Aging of the MCP: The high electron fluences applied inside the apertures also accelerate the degeneration of the MCP due to the very high electron counts per area. These high densities occur especially in the secondary yield of the photoelectron spectra, which are always present, because the detector measures all photoemitted energies. To remove this secondary yield from the photoelectron detector and simultaneously increase the electron yield at lower binding energies, there are different strategies. As successfully performed in [55, 56, 29], only a small fraction of the momentum space can be imaged, such that the secondary yield is not detected. The disadvantage is that, especially for the data obtained in this work, signatures appearing over the whole Brillouin zone can not be imaged simultaneously. Other strategies involve a potential barrier for the secondary yield, as performed by Kunin *et al.* [69]. While leading to slightly smaller transmissions, such an additional secondary filter, would be a useful add-on for future measurements.

Sample design for photoemission experiments: The quality of the ARPES experiment is strongly affected by the design of the sample system. During the photoemission process, non-conductive parts of the sample can be charged, which leads to extremely blurred photoemission signals. Besides that, it was shown that the quality of the photoemission data is additionally strongly affected by the surface potential of the given substrate [99]. Fig. A.9.2 shows a direct comparison of the photoemission data quality between ML WSe_2/SiO_2 and ML WSe_2/hBN/Si/SiO_2, where the ML WSe_2 is connected to bulk WSe_2, which is then directly coupled to the Si/SiO_2-interface. It is directly evident that the ML WSe_2/hBN/Si/SiO_2 shows much sharper bands, which directly affect the line width of the spin-split valence band from 0.58 eV to 0.3 eV (or 0.23 eV as reported in [30]), respectively. The reason is that the hBN provides here a very high surface quality [20], and the connection to the bulk and coupling to the substrate facilitates the distribution of excessive charge carriers to the substrate, whereas in the ML WSe_2/SiO_2, the substrate suffers from charging and charge impurities [99]. In addition, in the current experimental conditions the desired flake has to provide a minimal spatial size of about 10 µm, for feasible integration times without space-charge induced broadening. These requirements to the design and size of the sample for the photoemission experiment strongly affect the fabrication time.

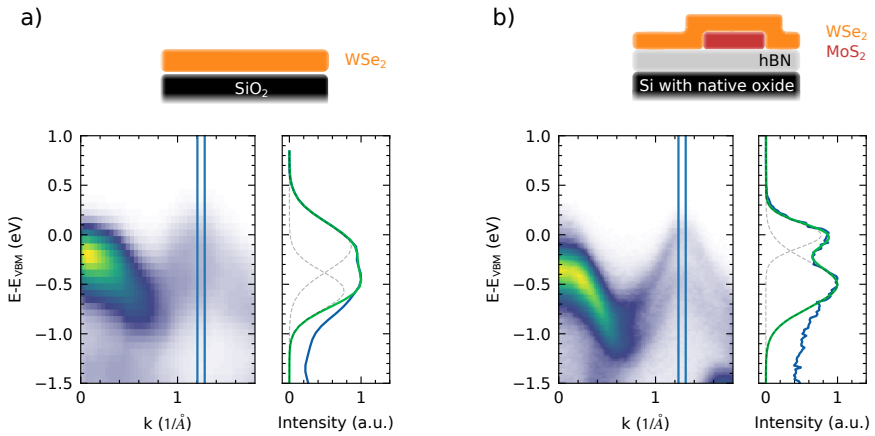

Fig. A.9.2.: a) Energy-momentum map of ML WSe_2/SiO_2 along the Γ-K-direction and extracted EDC around the K-valley b) Energy-momentum map of ML WSe_2/hBN/Si/SiO_2 along the Γ-K-direction and extracted EDC around the K-valley. The data is reproduced from [8] and [70].

Beside the charging of the sample due to photoemission of electrons and space-charge effects inside the sample (3) and in the microscope (1), the photoemission signal of the sample can also be affected by the applied pump pulse. The pump pulse excites also electrons in the respective substrates (mainly in silicon here), which alter the effective surface potential. This effect, known as the surface photovoltage effect (SPV)[186], leads to time-dependent energetic shifts in the order of < 100 meV of the whole spectrum and was observed in this work and other photoemission experiments [187, 70, 24]. Since this effect leads to a time-dependent distortion of the energy-axis, the rigid energy shift is post-corrected for all time-dependent measurements of this work (c.f. method-part in chapter 3).

Sample heating due to high pump average powers: In contrast to the applied pump pulse fluences in ref. [55] (5-17 mJ/cm^2), the fluences in this work are much smaller (280 µJ/cm^2). Therefore, the heating of the sample does not influence the actual measurement. But since the experiments are performed on scales of a few µm-regions of interest, the measurement is very sensitive to any appearing shifts of the sample, which could occur due to mechanical slackness of the sample-mount or residual heating effects of the sample. Especially, for the dark-field measurements with integration times up to 50 h, these effects need to be considered and corrected in post-processing (c.f. chapter 4).

Stability of the laser systems: During comparable µARPES and dark-field experiments, slight drifts of the optical pump and probe beams were observed, especially for larger integration times (>5h). In that case, the respective beams have to be aligned, which can alter the delay-position of the maximal temporal overlap (time-zero). These delay offsets affect the temporal resolution and could lead to artifacts, such as undesired double-peak structures, in the time-resolved photoemission signals. In order to remove such effects, only signals

showing the same temporal evolution are used for further post-processing. Further details are described in chapter 4 and the appendix B.

Limited option of apertures: As mentioned before, only a very small fraction of the HHG beam spot is used for the µARPES/dark-field experiments, which leads to very high integration times up to 50 h for one time series. A workaround to lower integration times would be either the fabrication of larger samples, which were not at hand during the experiments performed here, or precisely adjustable apertures to the exact size of the desired region-of-interest. For the performed µARPES experiments, the inserted aperture is only slightly smaller than the sample region. Inserting a larger aperture would give unwanted photoemission signal from other sample regions. Adjusting the aperture to the exact spatial region-of-interest, the experiment would benefit of slightly higher photoelectron yields. Much more significant is the situation for the dark-field experiment. Here, with the apertures at hand, only one specific signature can be selected in momentum-space. But, for signatures at the K-valleys for instance, the experiment contains actually six times more photoemission yield from the desired signature (considering even the 2. Brillouin zone, the factor is even higher). Therefore, in the dark-field experiment a large amount of photoemission yield is simply not used for imaging. A workaround could be provided by an aperture with the exact arrangement of the desired signal in momentum space, how it was successfully integrated and performed in a recent TEM dark-field experiment by Danz *et al.* [157].

Fortunately, most of these limitations could be in principle eliminated by future optimization and designing steps, which would end up in a much more efficient and stable data acquisition (c.f. section outlook).

APPENDIX B

Additional information on data handling

B.1. Data handling scheme

This section provides additional information to the manuscript "Ultrafast nano-imaging of dark excitons"[30], which are not included in the presented version of the manuscript. Because of the novelty of the measured data, a general data handling scheme concerning this type of data is not established yet. Therefore, this section and the method part of the manuscript should give suggestions on how to handle the data. This section concerns mainly quantitative details of the data pre-processing prior to the main evaluation described in the method section of the manuscript. As a starting point, the general data handling scheme is shown in Fig. B.1.1.

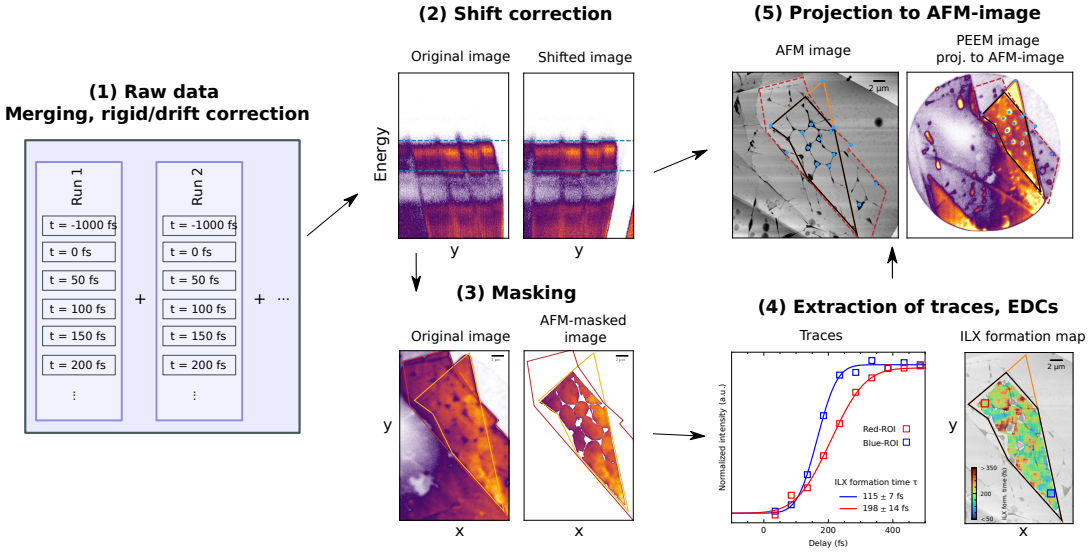

Fig. B.1.1.: Schematics of the data handling scheme.

Because of the low photoelectron statistics of the excitonic photoemission signatures, the integration times of the time-resolved dark-field experiment can be up to 51 h. The overall integration time includes 23 measurement cycles, where each data set is integrated for 10 min. In order to sum up the data sets of each measurement cycle, the data sets have to be corrected for energy-, lateral- and temporal shifts. In the following, the respective shifts are quantitatively analyzed, and the correction is presented.

B.1.1. Energy shift correction

In the method sections of the two presented articles, the presence of a rigid energy shift is observed due to space charge and surface photovoltage effects (SPV). The latter leads to a time-dependent energetic shift of the spectra and is thus visible in every measurement cycle. In Fig. B.1.2, the rigid energy shift is extracted by tracking the energetic position of a peak in the occupied region of the occupied band structure as a function of integration time (c.f. B.1.2 b) inset). At the start of every measurement cycle (gray dashed vertical lines) the peak is observed at lower energies and shifts upwards with increasing delay times in every cycle. Additionally, in the first 7 hours (in this particular measurement) also gradually decrease of the peak position is observed. After having quantified the energetic shift, all peak positions are mapped to a fixed reference position. The resulting corrected peak positions are displayed in Fig. B.1.2 b).

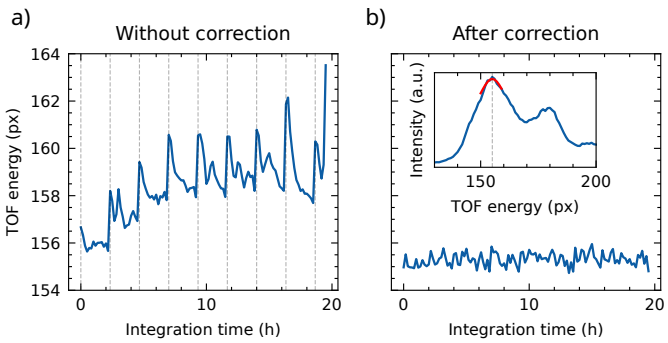

Fig. B.1.2.: Observed rigid energy band shift as a function of integration time before a) and b) after the correction is applied. For the correction, all spectra are aligned to the same peak maximum, indicated in the inset of b). The gray vertical lines indicate the start of a new measurement cycle.

B.1.2. Lateral shift correction

During the high integration time, lateral rigid shift of the sample can occur between measurement cycles due to residual heating effect of the pump in the beginning of the measurements (and) or mechanical slackness of the sample mount. In order to quantitatively analyze this occurring shift, a cross-correlation between all data sets and an arbitrary reference image is performed. An exemplary extracted x, y-shift as function of integration time is shown in Fig. B.1.3.

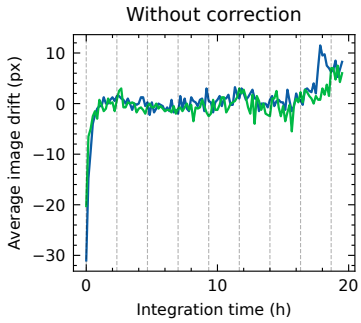

Fig. B.1.3.: Observed lateral shift in pixel (px) as a function of integration time. The gray vertical lines indicate the start of a new measurement cycle.

In the beginning, a strong shift in x and y-direction is observed. After that initial shift, the position of the sample remains comparably stable within the level of noise. At the end a slight increase of the drift is observed, which is mainly an effect of a drifting probe beam position, leading to unequal illumination of the sample and thus, worsens the accuracy of the cross-correlation significantly. Therefore, these data sets are not taken into account for the final data merging. In this regard, it should be mentioned that in order to minimize effects of uneven illumination, the data were normalized, and the average intensity was subtracted prior to the cross-correlation. However, although there may be some residual beam pointing or probe beam drift, the effect should be small because the size of the probe beam is much larger than the region-of-interest and the averaging over multiple measurements should cancel out additional pointing effects.

Much more critical are the influences of beam drifts for the temporal overlap. The spatial displacement of the pump and probe beams could lead to a change of the temporal overlap between pump and probe. While the probe beam intensity can be normalized by normalizing to a specific spectral signature, e.g. the peak in Fig. B.1.2, the drift and corresponding intensity loss and the potential change in the temporal overlap inside the region-of-interest of the pump can not be directly determined by the spectral information. Here, for every measurement the probe-normalized temporal evolution of the excited signal above the Fermi-energy is extracted, and the respective traces are inspected for temporal shifts and intensity changes. Traces which are showing significant differences are excluded for the final merging of the

data.

After performing of the prior correction and removing steps, the data sets of each measurement cycle with the same temporal information are summed up.

B.1.3. Energy-dependent shift correction

Beside the rigid lateral shift described before, an additional energy-dependent lateral shift is observed (c.f. Fig: B.1.4 a)). Since this shift is constant for all measured data sets, the observed shift does not affect the merging procedure. However, in order to extract spectral information at a certain place over a large energy range, the occurring shift has to be corrected. For that, the shift has to be quantitatively analyzed, which is done by performing again a cross-correlation between an image at a certain reference energy and images at other energies. The extracted shift is shown in Fig: (c.f. Fig: B.1.4 b)) and a linear shift as function of energy in the considered energy range is observed. In this case, the shift occurs only in y-direction, whereas the shift in the x-direction can be neglected. By a linear interpolation of the energy-dependent lateral rigid band shift, the data sets can be corrected for all energies, by shifting the data sets with the respective shift Fig (c.f. Fig: B.1.4 c)).

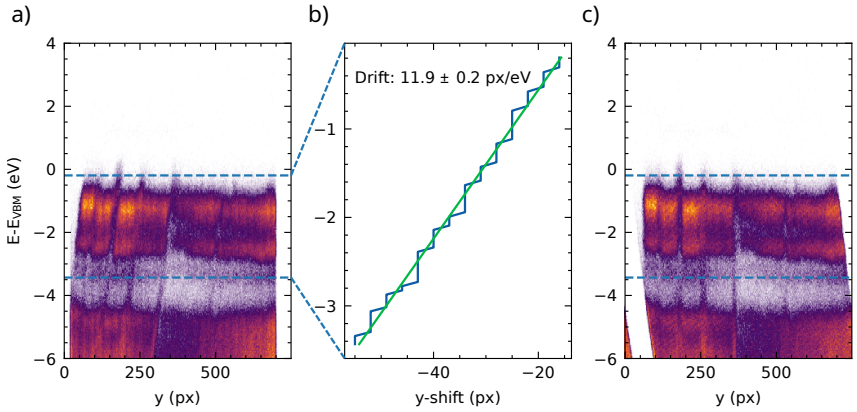

Fig. B.1.4.: a) Energy-real-space map before the correction is applied. A lateral shift of the data with decreasing energy is observed. b) The shift as a function of energy is extracted via a cross-correlation. A linear fit is used to describe the shift and yield a slope of 11.9 $\pm$ 0.2 px/eV. c) Corrected data with the linear interpolation from b).

Note, that the shift is only corrected with pixel precision. Since the spatial evaluation of the exciton landscape and formation dynamics (c.f. chapter 4) are performed with much larger pixel areas of 10 to 20 pixels, the error should be neglectable small.

B.1.4. Blister removal

In the main and method part of the manuscript, it is pointed out that 'blisters' are intentionally removed from the evaluation. The reason is that some effects at the blister regions can be strongly enhanced, such as strain, dielectric environment, decoupling of the layers and charging effects (c.f. section 2.3). Additionally, the question rises where emitted photoelectrons of blister regions occur in momentum space. The topography in the vicinity of blisters could lead to varying photoemission angles and thus, the photoelectrons are not arriving in the selected region-of-interest in momentum space.

Because of the presence of these multiple effects and their unknown influence on the photoemission signal, the blister regions are excluded from further evaluation by performing a threshold with the help of the AFM image. As shown in Fig. 4.0.7 of the method part, the blister regions are clearly visible and show height differences of up to 80 nm. By thresholding height differences > 20 nm a mask of the AFM image can be created and applied to the respective data sets (c.f. Fig. B.1.5)

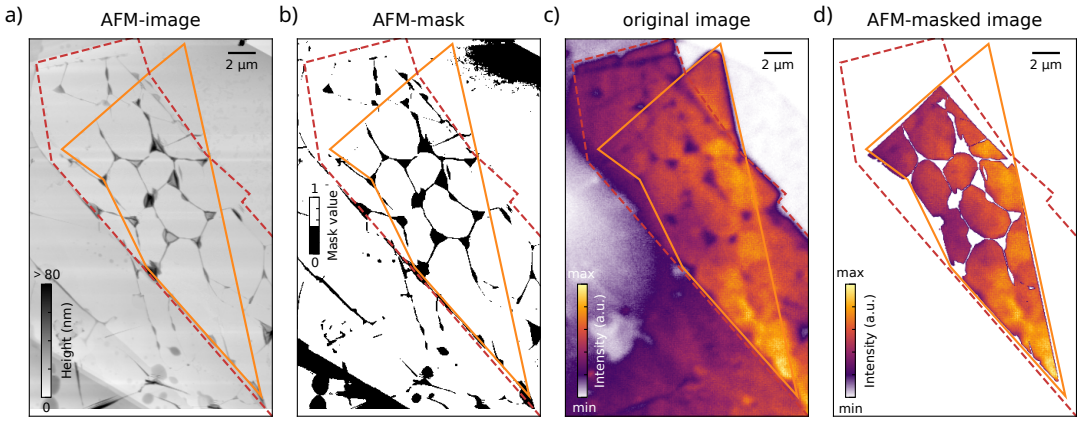

Fig. B.1.5.: a) AFM image of the heterobilayer and adjacent monolayer, bulk and hBN regions. b) Threshold of the AFM image with heights of 20 > nm. c) Exemplary dark-field image. d) AFM-mask of b) applied to the image in c). Note, that image d) is additionally cropped to the heterobilayer region of the sample before the mask is applied. In all images, the WSe_2 and MoS_2 monolayer flakes are labelled with orange and dark red borders, respectively.

After having performed the described steps, the respective quantities such as time-traces or EDCs are extracted from the corrected data sets. Finally, the projection to the AFM image is performed as described in detail in the method part after the evaluation steps are performed. The reason for the projection as a last step is that a strong deformation of the image could lead to a variation of the intensity per pixel (considering constant pixel sizes) and thus, this effect could lead to a manipulation of the extracted quantities. However, since the distortion field in Fig. (c.f. Fig. 4.0.8) is relatively uniform, the influence of this effect is considered to be small.

Danksagung

Mit dieser Danksagung möchte ich mich bei den vielen Menschen bedanken, die mich in den insgesamt fünf Jahren meiner Dissertation sowohl wissenschaftlich als auch freundschaftlich begleitet und damit wesentlich zum Gelingen dieser Arbeit beigetragen haben.

Als Erstes möchte ich meinem Doktorvater Stefan Mathias danken. Danke, dass du es mir ermöglicht hast, an diesem großartigen Projekt meine Doktorarbeit zu schreiben. Einer der wichtigsten Punkte für mich persönlich war es, dass du mir den Freiraum gegeben hast, selbständig an diesem Projekt zu arbeiten und dass du stets ein gewisses Grundvertrauen und eine positive Einstellung bezüglich meiner Arbeit hattest, auch wenn es mal nicht so gut lief. Neben den zahlreichen Diskussionen zu dem Experiment (besonders am Anfang) möchte ich mich noch für zahlreiche wissenschaftliche Diskussionen und Anmerkungen bezüglich der Paper und dieser Arbeit bedanken. **Vielen Dank Stefan** für die tolle Zeit.

Ein ganz großer Dank gilt Marcel Reutzel. Vielen Dank für die zahlreichen Diskussionen bezüglich des Experimentes und der Manuskripte, für neue Ideen (die uns manchmal nicht schlafen ließen), für zahlreiche "Text" und "Figure" Reviews, für zahlreiche Jokes, die manchmal vielleicht auch eher nicht für die Vorlesung geeignet waren, für die Motivationsschübe, mit den du alle mitreißt, für ..., für ..., für .... Ich würde diese ganzen "fürs" einfach mal als "Quality Time" mit Marcel betiteln. Also **vielen Dank Marcel** für die "Quality Time".

Danke an Thomas Weitz für die Übernahme des Zweitgutachtens und auch für einige Anregungen bezüglich der Paper. Danke auch für die Bereitstellung einiger Graphene-Proben, die es uns ermöglicht haben, erste erfolgreiche Impulsmikroskopie Messungen von mikrometergroßen Proben durchzuführen. Hier auch vielen Dank an einige Mitglieder der AG Weitz: Monica Kolek Martinez de Azagra und Anna Seiler für die Herstellung der Proben und auch an Jonas Pöhls für die Durchführung der AFM-Messungen zu dem Nano-Imaging paper.

Ein weiterer großer Dank richtet sich an das (ex-)MoMi-Team bestehend aus Marius Keunecke, Christina Möller, Jan Philipp Bange, Wiebke Bennecke, Marco Merboldt ohne deren Einsatz dieses Projekt nicht möglich gewesen. **Danke Marius** für die grandiose Aufbauarbeit des MoMis und für die zahlreichen Mess-Sessions inklusive Nachtschichten. **Danke an Christina** für den Aufbau der HHG-Kammer und die ersten Messungen am MoMi.

Hervorheben möchte ich hier insbesondere das aktuelle MoMi Team, ohne das diese Arbeit und die resultierenden Messungen/Ergebnisse in den letzten Jahren nicht möglich gewesen wären. **Danke Jan Philipp, Wiebke und Marco**, dass ihr mit stets guter Laune und komischerweise auch mit einer Mischung aus Optimismus und Ironie die zahlreichen Mess-

Sessions ("mit der zweitkleinsten Blende der Welt") oder das Instandhalten vom Experiment ("Aber stabil, oder? ... oder?") sehr angenehm gemacht haben. Und dann natürlich nochmal einen extra Dank an Jan-Philipp, Wiebke und **Matthijs** für die Zusammenarbeit an den beiden Papern.

Dieses große Projekt am Impulsmikroskop wurde auch durch die Mithilfe von vielen Doktoranden, Masteranden und Bacheloranden nach vorne gebracht, bei denen ich mich an dieser Stelle bedanken möchte. **Vielen Dank an Paul, Hendrik, Michael und Marie**.

Dieses Projekt hätte auch nicht funktioniert, ohne die Unterstützung von den Technikern. **Danke an Carsten, Uta und Kai**.

Special thanks to AbdulAziz Almutairi for the "ultrafast" fabrication of the TMD heterostructures, for being enthusiastic about new sample systems and for the great discussion. Thanks to his supervisor, Stephan Hofmann, for this very fruitful collabaration and great discussion. **Thanks to The HOFMANN group**.

Special thanks to Giuseppe Meneghini, Samuel Brem and Ermin Malic, for the theoritcal "input" for both manuscripts , for numerous comments on the paper drafts and the removal of ambiguities. **Thanks to the Ultrafast Quantum Dynamics Group**.

Meiner Meinung nach ist ein wichtiger Teil einer Doktorarbeit nicht nur die wissenschaftliche Seite, sondern auch eine gut funktionierende, sich helfende Arbeitsgruppe. Dafür möchte ich eigentlich fast allen Leuten aus der AG-Mathias danken, die auf jeden Fall diese Doktorandenzeit nochmal wesentlich verschönert haben. **Danke an Henrike, Marten, Tim, Daniel, ...** und natürlich nochmal alle Mitglieder, die bereits vorher genannt wurden.

Einen großen Beitrag zu der guten Arbeitsmosphäre haben natürlich auch die Mitglieder des I. physikalischen Institutes, denen ich an dieser Stelle danken möchte. **Danke an die Mitglieder des I. physikalischen Institutes**.

Ich möchte an dieser Stelle auch meiner Familie danken, die mich zu Bachelor- und Masterzeiten finanziell unterstützt haben und somit dieses Studium überhaupt ermöglicht haben und für das Interesse an dieser Arbeit. Schließlich möchte ich mich bei meiner Freundin bedanken. Dafür, dass du mir immer einen Rückhalt gibst und ich mich in jeder Situation auf dich verlassen kann.